

Provash Chandra Sadhukhan
Sanjay Premi *Editors*

Biotechnological Applications in Human Health

 Springer

Biotechnological Applications in Human Health

Provash Chandra Sadhukhan •
Sanjay Premi
Editors

Biotechnological Applications in Human Health

 Springer

Editors

Provash Chandra Sadhukhan
Division of Virus Laboratory
ICMR-National Institute of Cholera and
Enteric Diseases
Kolkata, West Bengal, India

Sanjay Premi
Tumor Biology
Moffitt Cancer Center
Tampa, FL, USA

ISBN 978-981-15-3452-2 ISBN 978-981-15-3453-9 (eBook)
<https://doi.org/10.1007/978-981-15-3453-9>

© Springer Nature Singapore Pte Ltd. 2020

This work is subject to copyright. All rights are reserved by the Publisher, whether the whole or part of the material is concerned, specifically the rights of translation, reprinting, reuse of illustrations, recitation, broadcasting, reproduction on microfilms or in any other physical way, and transmission or information storage and retrieval, electronic adaptation, computer software, or by similar or dissimilar methodology now known or hereafter developed.

The use of general descriptive names, registered names, trademarks, service marks, etc. in this publication does not imply, even in the absence of a specific statement, that such names are exempt from the relevant protective laws and regulations and therefore free for general use.

The publisher, the authors, and the editors are safe to assume that the advice and information in this book are believed to be true and accurate at the date of publication. Neither the publisher nor the authors or the editors give a warranty, expressed or implied, with respect to the material contained herein or for any errors or omissions that may have been made. The publisher remains neutral with regard to jurisdictional claims in published maps and institutional affiliations.

This Springer imprint is published by the registered company Springer Nature Singapore Pte Ltd.
The registered company address is: 152 Beach Road, #21-01/04 Gateway East, Singapore 189721, Singapore

Foreword

Biotechnology has offered an immense opportunity from prevention to diagnosis to prognosis and treatment toward the protection of human health. Human well-being can be ensured by utilizing powerful biotechnological tools, which might include developing vaccines to stimulate the immune system, thus protecting the body to drug development for the treatment and many more. The findings of the human genome project and further advancement of recombinant DNA technology made a lot of things possible which once was beyond imagination. In vitro generation of different hormones and their use in treating diseases (the most common one is insulin) are possible only by utilizing biotechnological techniques.

Different biotechnological techniques like a polymeric chain reaction or site-directed mutagenesis to microarray techniques are helping in specifically identifying different genetic diseases as well as giving guidance for treatment. Understanding gene sequence has made it possible to diagnose the disease more accurately and in some cases to develop personalized medication. Newly developed proteomic technology is also a promising technique for an understanding of pathogenicity and virulence factors that will open up new possibilities of disease diagnosis and appropriate protection measures. It is also possible to predict the vulnerability of a genetic disease for an individual so that an appropriate preventive measure can be taken.

This book contains 12 chapters on different applications of biotechnology for human well-being. One chapter includes NIRS, the non-obtrusive, simple appropriate instrument to quantify the tissue oxygenation, and alongside the vascular impediment, it shows promising outcomes in breaking down the ailing states. Regardless of the accessibility of different NIRS frameworks, there is no one-of-a-kind instrument for screening and surveying the tissue oxygenation parameters at foot bottom regions in case of diabetic foot patients. The book also includes a chapter on the ionizing radiation-induced MMP-2 expression, cytotoxicity, and DNA damage. There is also another chapter on the study of the altered profile of regulatory T cells and NKT cells which are characteristics of Chikungunya-related polyarthralgia. Another work in the book is on molecular docking and drug designing for treatment. A very important chapter on the study of molecular protein interaction for inhibiting growth of human leukemic cells toward drug development is also included. There is a work on the method of universal primer design for the detection of diverged multi-drug-resistant genes in superbugs. There is also a very important study on cytotoxicity and apoptosis of human colon carcinoma cells.

The chapters in this book include some of the research work going on pan India and abroad on preventive and curative aspects of human health presented at the International Conference on Biotechnology and Biological Sciences, BIOSPECTRUM. In conclusion, it can be said that the role of biotechnology in human health and well-being is so multifarious that it is impossible to brief all the aspects in a single write-up.

Department of Biotechnology
University of Engineering & Management,
Kolkata, West Bengal, India

Susmita Mukherjee

Contents

1 Design of Multi-wavelength Near Infrared Probe to Detect Risk Areas in Diabetic Foot	1
N. P. Guhan Seshadri and R. Periyasamy	
2 Cellular and Molecular Response for Sensitising Cancer Cells and Protecting the Normal Cells from Radiation-Induced Damages	11
Shailender Gugalavath and Rama Rao Malla	
3 A Novel Approach for Production and Study of Medical Ultrasound from Low-Cost Electromagnetic Transducers	23
Srijeet Chatterjee, Priyam Biswas, and Pratik Das	
4 Altered Profile of Regulatory T Cells and NKT Cells As Characteristic of Chikungunya-Associated Polyarthralgia	33
Nilotpal Banerjee, Bibhuti Saha, and Sumi Mukhopadhyay	
5 Cytotoxicity and Apoptosis of Human Colon Carcinoma Cell Line (HT29 Cells), Treated with Methanolic Extract of <i>Chlorococcum humicola</i>	39
Uma Ramaswamy, Sivasubramanian Velusamy, and Niranjali S Devaraj	
6 Universal Primer Design for the Detection of Diverged CTX-M Extended-Spectrum β-Lactamases (ESBL) That Give Penicillin and Cephalosporin Resistance During Superbug Infections	45
Asit Kumar Chakraborty, Kousik Poria, and Sourav Kumar Nandi	
7 Lipopeptides as Therapeutics: Molecular Docking and Drug Design	61
Satya Eswari Jujjavarapu and Swasti Dhagat	

8	Design and Simulation of Geometrical Shape and Size Variations of Micro-electrode for Cochlear Implant	69
	Abhishek Nigam, Faiz Ahmed, and S. J. Pawar	
9	Molecular and Protein Interaction Studies for Inhibiting Growth of Human Leukemic Cells: An In Silico Structural Approach to Instigate Drug Discovery	77
	Arundhati Banerjee, Rakhi Dasgupta, and Sujay Ray	
10	Laccase-Mediated Synthesis of Bio-material Using Agro-residues	87
	Komal Agrawal and Pradeep Verma	
11	Extraction of Fungal Xylanase Using ATPS-PEG/Sulphate and Its Application in Hydrolysis of Agricultural Residues	95
	Nisha Bhardwaj and Pradeep Verma	
12	Thyme (<i>Thymus vulgaris</i>) Essential Oil-Based Antimicrobial Nanoemulsion Formulation for Fruit Juice Preservation	107
	Aakash Patel and Vijayalakshmi Ghosh	

About the Editors

Provash Chandra Sadhukhan, Ph.D Scientist–E, ICMR-National Institute of Cholera and Enteric Diseases, Kolkata, did his MSc and PhD from the Department of Biochemistry, University of Calcutta, and did his postdoctoral work in the Department of Cancer Biology, Cleveland Clinic Foundation, USA, for more than 6 years. In his postdoctoral study, his major area of research was on interferon and NF- κ B signaling in bladder and kidney cancer. He also did gene therapy work for bladder cancer treatment. He joined ICMR Virus Unit, Kolkata, in the year 2005 working in different aspects of hepatitis C and dengue virus. His present research interests are low-cost viral detection, molecular epidemiology, host-virus interaction, viral pathogenesis, nanomedicine for viral replication inhibition, and cell signaling. Currently, his research team is working in the field of infectious diseases with special emphasis on RNA viruses, dengue, and hepatitis C virus. The group mainly focuses on the propensity of envelope gene antigenic dynamicity and its implication regarding neutralizing antibodies and its associated host cell receptor-mediated entry of HCV and dengue virus and HCV infections within high-risk group population and their immune response against this virus. The functional role of HCV RNA and its structural protein (core protein) associated with signaling pathway leading to pathophysiological changes in liver hepatocytes is also being explored. His research platform is based on HCV and dengue from eastern and northeastern region of India and an exhaustive interface between clinical sciences, experimental biology, and bioinformatics which leads to translation research. He has more than 45 publications in national and international journals.

Sanjay Premi is an Assistant Professor at Moffitt Cancer Center with an affiliated assistant professorship at the University of South Florida, Tampa, Florida, USA. He completed his master's and PhD degrees from Jawaharlal Nehru University, New Delhi, India, in 2008 and moved to the USA for his postdoctoral training. After spending about 7 years at Yale University as a Postdoc and Associate Research Scientist, he was hired as a faculty by Moffitt Cancer Center. Dr. Premi is a renowned scientist in the fields of photobiology, skin carcinogenesis, and skin pigmentation. During his PhD, he established a unique signature of radiation exposure in human genome which seems to buffer out the carcinogenic and genotoxic effects of high background radiation. During his postdoc at Yale, he discovered a carcinogenic role

of the skin pigment melanin which is otherwise considered as a potent sun-shield. Till date, Dr. Premi has published around 20 peer-reviewed articles in high-impact journals which includes *Science*, *Proceedings of the National Academy of Sciences of the United States of America (PNAS)*, and *The Journal of Infectious Diseases (JID)*. In 2018, he was awarded the prestigious Wellcome-DBT India Alliance Fellowship worth ~500 k US dollars. He is frequently invited guest speaker at various national and international institutions and meetings.



Design of Multi-wavelength Near Infrared Probe to Detect Risk Areas in Diabetic Foot

1

N. P. Guhan Seshadri and R. Periyasamy

Abstract

Diabetic foot diseases are the most common problem among people with diabetes mellitus (DM) that lead to lower body amputation. Loss of sensation (neuropathy) at the foot areas, peripheral arterial disease, and poor microcirculation at foot are the major risk factors which suppress the oxygen availability to the tissues, leading to ulcerations. Different methods are applied for noninvasive measurement of tissue oxygenation. Though there was an immense interest and rigorous research in this area for the last two decades, presently there is no suitable device to assess the tissue oxygenation noninvasively at foot sole. Near infrared (NIR) spectroscopy aids in examining the tissue oxygenation levels in noninvasive manner and also helps in evaluating the values of tissue oxygenation levels at specific region in the foot sole. In this chapter, a noninvasive multi-wavelength (740/850, 740/940) NIR probe was developed using light-emitting diodes (LED) to assess the tissue-oxygenation parameters by using the reflective characteristics of skin tissue in the plantar surface of patient foot, along with the tissue hardness, and temperature at the foot sole areas were obtained. From this study, diminished tissue oxygenation is observed at the area where the tissue hardness and foot sole temperature is high. In conclusion, a proposed optical-based multi-NIR wavelength method can be used to avoid the damages in lower extremity peripheral nerves and to identify the risk areas in the foot at an early stage before it leads to ulceration.

Keywords

Diabetic foot · Near infrared spectroscopy · Tissue oxygenation · LED · Ulceration

N. P. Guhan Seshadri · R. Periyasamy (✉)
Department of Biomedical Engineering, National Institute of Technology Raipur,
Raipur, India
e-mail: rperiya.bm@nitrr.ac.in

1.1 Introduction

Diabetic foot diseases are the most common problem among people with Diabetes mellitus (DM) that lead to lower body amputation. Loss of sensation (neuropathy) at the foot areas, peripheral arterial disease, and poor microcirculation at foot are the major risk factors which suppress the oxygen availability to the tissues, leading to ulcerations. This suppresses the transportation of oxygen into the living body tissues, leads to diminished oxygen supply and blood circulation to the cells, and causes cell necrosis due to ischemia at the end. So, it is important to evaluate and monitor the tissue oxygenation and perfusion at the local tissue level concerning the identification of risk areas before ulceration. Over a last decade, optical techniques are highly established because it offers a noninvasive, real-time technique for measurement of oxygen saturation in medical diagnostics [1–7]. It was first evolved in 1935 when German physicist Karl Matthes developed a first ear oxygen saturation meter using two wavelengths of light (red and green) [8]. Transmission of light into biological tissues causes the light to reflect, absorb, and scatter based on the tissue optical properties and wavelength of the transmitting light. In particular, the wavelength range from 600 to 1200 nm (so-called “therapeutic window”), the penetration of light into the body tissues are deep in this bandwidth, because of more scattering of light into the tissues than the absorption [9]. Initially in 1972, Takuo Aoyagi developed a pulse oximeter with the absorption ratios of red and infrared light, and it was marketed by Biox technologies in 1981 mainly focusing on respiratory care and monitoring patients in operation theaters, and later it spread worldwide to monitor the oxygen saturation and cerebral oxygenation [8]. Pulse oximetry is limited as it only measures oxygen saturation at the pre-capillary arteriole. In contrast, near infrared spectroscopy (NIRS) measures oxygenation levels at both capillary bed and post-capillary venule (StO_2) [10]. Recently, many researchers are focused in developing a multi-wavelength near infrared system to calculate the tissue oxygenation. Jun Li developed a low-cost imaging system using CCD camera with two laser diodes of wavelengths 660 and 880 nm for mapping skin venous oxygen saturation [11]. Khallil designed a diffuse optical tomography using two laser diodes of wavelength 680 and 880 nm for the detection of vascular dynamics at foot [12]. Zhang Y studied spatial variation of tissue oxygenation using multiple source detector to estimate the hemodynamics changes in biological tissues with the wavelengths 735, 760, 810, and 850nm [9], but the scattering factor in the calculation of tissue oxygenation makes the spatial variation method less reliable for multilayered structure [13]. Though there was an immense interest and rigorous research in this area since two decades [1–7], there is no convenient device at the market that can measure the tissue oxygenation in the foot sole noninvasively. Therefore, the present study aimed at designing a NIR probe using LEDs of wavelength 740, 850, and 940 nm with fixed source detector distance to assess the tissue-oxygenation parameters by using the reflective characteristics of skin tissue in the plantar surface of patient foot, along with the tissue hardness and temperature at the foot sole areas in order to identify the risk areas which are prone to ulceration

1.2 Instrumentation and Experiments

The system uses three LEDs of wavelength 740, 850, and 940 nm in the near infrared region of electromagnetic spectrum as a light source as shown in Fig. 1.1a. These wavelengths were selected because it covers the absorption bands of oxygenated hemoglobin (HbO₂) and deoxygenated hemoglobin (HHb) and it is closely associated with venous oxygen saturation, minimally affected by skin blood flow, mainly derived from HHb and not myoglobin [14]. The LEDs are switched on manually so that the detected signals at each wavelength could be analyzed separately.

The detector part consists of PIN photodiode (QSD2030F) having high sensitivity, daylight filter, and peak sensitivity at 880 nm. The distance between the LED source and photodiode is fixed at 1.5 cm (shown in Fig. 1.1b). The source and detector are arranged side by side in order to carry the measurements in a reflectance mode. The photodiode is integrated with trans-impedance amplifier in order to

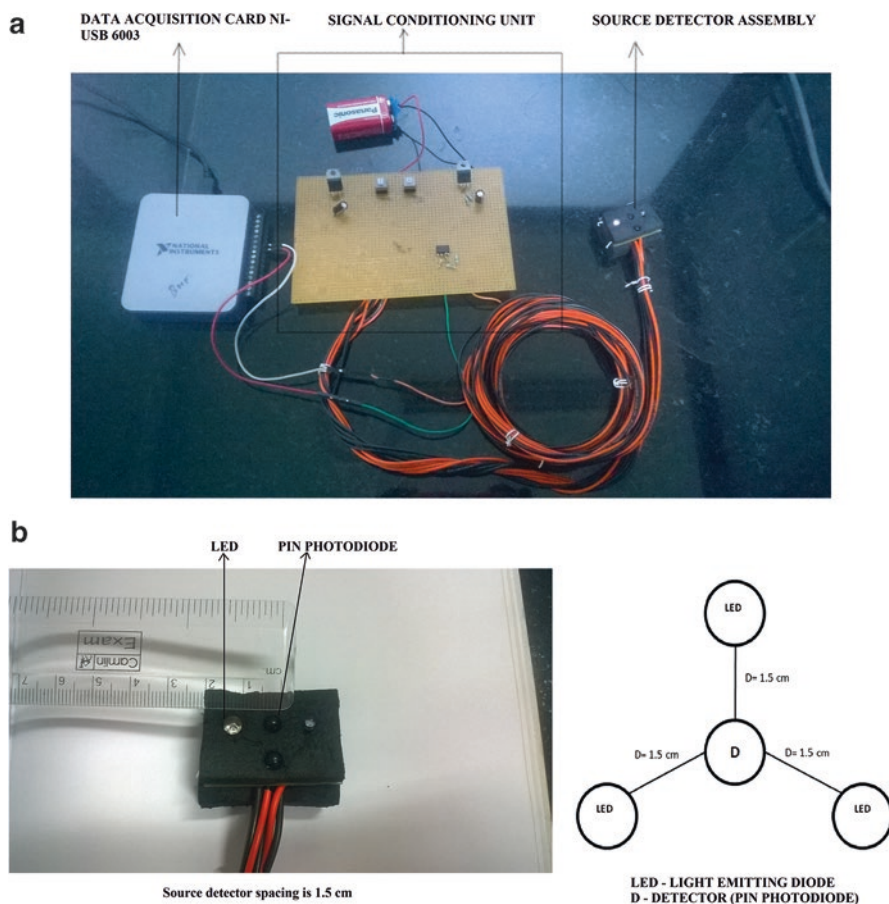


Fig. 1.1 (a) NIRS system. (b) Source detector assembly with a separation distance of 1.5 cm

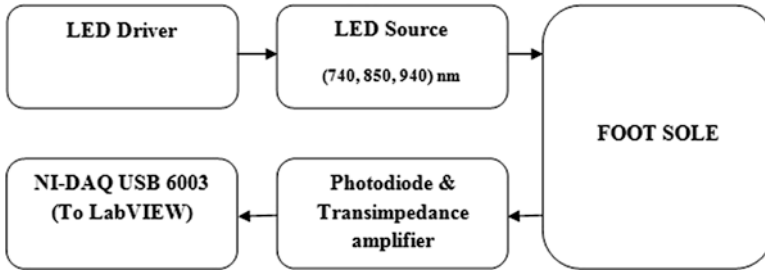


Fig. 1.2 Block diagram of the NIRS system

convert the photodiode current output in voltage, and the voltage signal is taken to LabVIEW for further analysis using data acquisition card (NI-USB 6003). From the acquired reflectance signal, modified Beer–Lambert’s law was used to find out the absorbance and changes in the concentration of oxyhemoglobin (HbO_2), deoxyhemoglobin (HHb), and total hemoglobin (THb) [9]. A block diagram of the entire setup is shown in Fig. 1.2.

1.2.1 Evaluation of Probe

Real-time testing of the system is done by monitoring the blood flow in the forearm. The human forearm occlusion is commonly used as reference for the interpretation and evaluation of *in vivo* NIRS [15], since it is safe and convenient; to evaluate the probe, we have restricted the blood flow in order to assess the temporal response of the blood flow in the forearm. The NIRS probe was placed on lower forearm of a healthy volunteer and the pressure cuff was wrapped around the upper arm. The signal of blood flow in the lower arm was recorded during 0–5 s of baseline recording and 5–20s inflating pressure above 180 mmHg (arterial occlusion) and 20–50s for pressure release and recovery time for each wavelength. The changes in optical density due to the halt of blood flow after occlusion was detected by the NIRS system, and Fig. 1.3 shows the optical density of the blood flowing through the human forearm measured during its occlusion at 180 mmHg.

1.2.2 Experiment Protocol

The NIRS system along with vascular occlusion technique was used in order to examine the response for the standard ischemic stimulus. The foot is anatomically marked into 10 significant areas based on the method by Cavanagh [16] shown in Fig. 1.4. We aimed at measuring the tissue oxygenation at the three standard regions (areas 2, 5 and 8) in the foot sole of healthy volunteers shown in Table 1.1. Before acquiring the data, subjects were asked to wash their feet so that there is no dirt

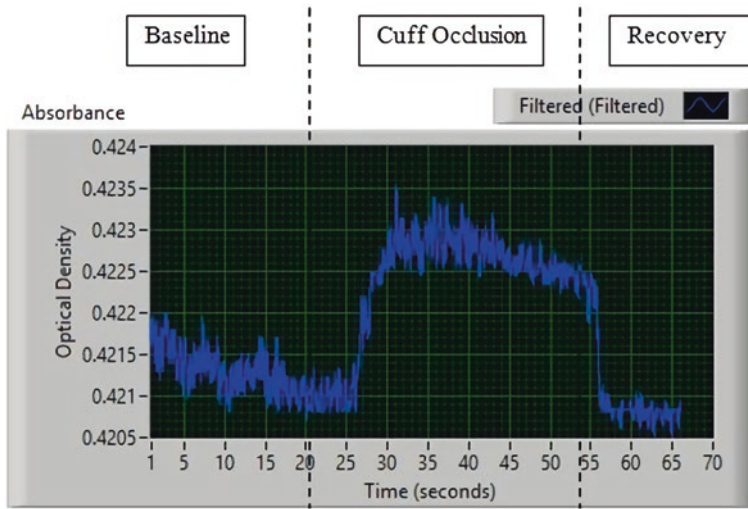


Fig. 1.3 Forearm occlusion response

Fig. 1.4 Anatomical separation of foot areas

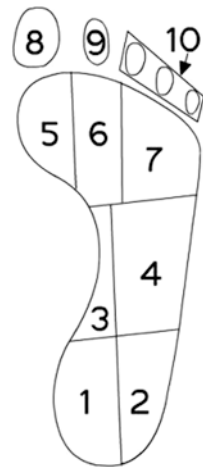


Table 1.1 Foot sole areas assessed in this study

Foot area	Anatomical name
2	Calcaneum
5	Ball of great joint
8	Great toe

which may affect the incident light. Two healthy volunteers were selected for the measurements, and their mean age was $26.5 (\pm 2)$. The volunteers are asked to relax for 15 min in supine position before the start of experiment. The foot sole hardness and temperature are also measured using a shoremeter and an infrared thermometer, respectively. The experiment protocol followed was 3 min baseline recording, 3 min cuff inflation to halt arterial blood flow (180 mmHg), and 3 min recovery time [17]. Three minutes occlusion period was followed because it allows calculation of all indices of interest (HbO_2 , HHb, THb) without augmenting patient discomfort [17].

1.3 Results and Discussion

The experiments were done in the foot sole of healthy volunteers and an inflatable blood-pressure cuff was wrapped around the calf muscles. During arterial occlusion, the probe (source and detector assembly) is placed over the plantar surface of the foot sole. Pressure was applied on the calf muscle (180 mmHg) for 3 min to achieve arterial occlusion, and then the pressure was deflated. The changes in concentration of HbO_2 , HHb, and THb for different wavelengths were calculated and observed.

It was observed that the absorbance for the wavelength 740, 850, and 940 was increased progressively during the period of occlusion and it comes back to the baseline after the release of pressure as shown in Fig. 1.5. The concentration of HbO_2 was decreased during the time of arterial occlusion because of the halt of blood flow completely and it returns to the baseline after the release of pressure. In contrast, the concentration of HHb was increased during the period of arterial occlusion which shows the lack of oxygen perfusion to the tissue and it remains high

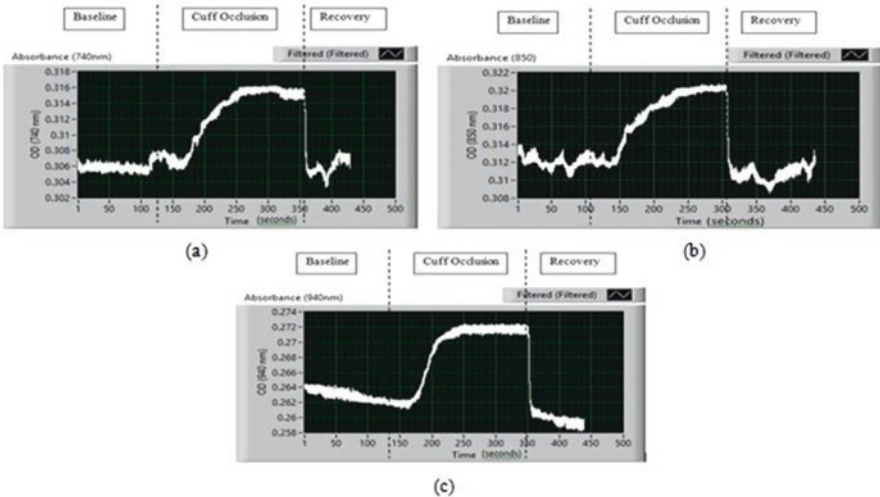


Fig. 1.5 (a) Absorbance at 740 nm (b) Absorbance at 850 nm (c) Absorbance at 940 nm

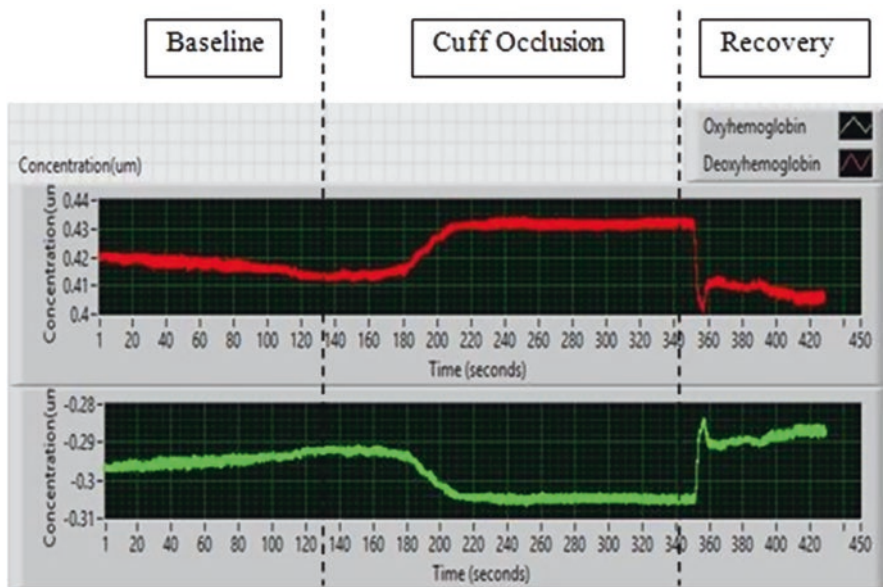


Fig. 1.6 Concentration of HbO_2 and HHb

during entire period of occlusion and returns to its baseline after the release of pressure shown in Fig. 1.6.

The total hemoglobin (THb) was calculated by adding the concentration of HbO_2 and HHb, and the hardness at the point of foot sole areas was measured. The plot of THb in the foot sole is shown in Fig. 1.7. From the Fig. 1.7 it is noted that the THb

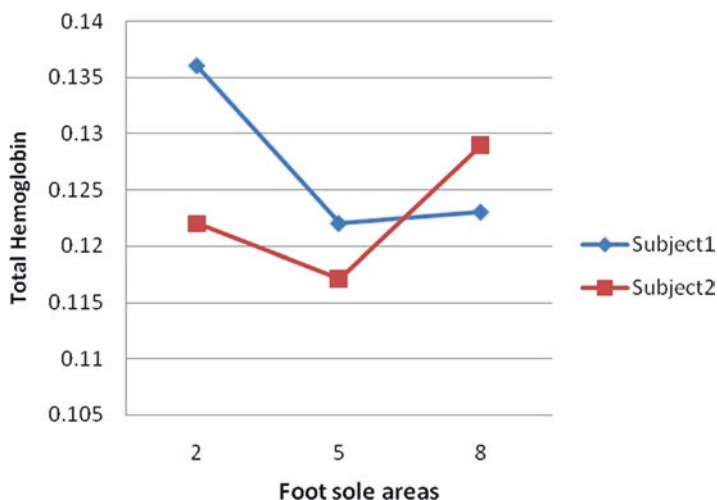


Fig. 1.7 Total hemoglobin in different foot sole areas

Table 1.2 Total hemoglobin, tissue hardness, and temperatures at measuring sites

Samples	Foot sole area	THb	Hardness	Temperature (°C)
Subject 1	2	0.136	16	30
	5	0.122	18.5	30
	8	0.123	17.5	29
Subject 2	2	0.122	12.5	31
	5	0.117	16.5	30
	8	0.129	15.5	30

level was minimum in the foot area 5 (Ball of Great joint). Comparing the tissue hardness with the THb value (shown in Table 1.2), the foot area 5 with minimum THb holds higher hardness degree than other two areas, foot area 2(Calcaneum), and foot area 8(Great toe).

NIRS with vascular occlusion is a promising technique to examine the response for a standard ischemic stimulus [17]. Therefore in the present study, vascular occlusion technique was used to find out the tissue oxygenation (oxygen demand and oxygen supply) in the plantar surface of the foot in order to identify risk areas. It was observed that area 5 (ball of great joint) in the plantar surface of foot has lower THb value as compared to other two areas (area 2 and area 8). It shows the poor oxygen permeability to the tissues at area 5 as compared to other two areas. Lin [18] stated that the poor supply of oxygen to the tissues leads to thickening of basal layer of blood wall and ends in cell necrosis forms in the underlying tissues being excessively hard. Accordingly, the present study also analyzed the foot sole tissue hardness and temperature. It was observed that the tissue hardness at the area 5 was high as compared to other two areas where as the THb value at the area 5 was low indicating the relationship between the hardness of the tissue to THb level. However, there was no significant difference in the temperature data (shown in Table 1.2) among the measured foot sole areas in normal subjects.

1.4 Conclusion

NIRS is a noninvasive, easy applicable tool to measure the tissue oxygenation, and along with the vascular occlusion, it shows promising results in analyzing the diseased state. Despite the availability of various NIRS systems, there is no unique tool to monitor and assess the tissue-oxygenation parameters at foot sole areas to identify the risky regions before it get affected. So, in the present study, we designed a NIRS probe which solely measures the tissue oxygenation at foot sole areas which can be used at diabetic foot care centers to monitor and identify risk areas at foot sole. The NIRS probe was tested on only few subjects; in order to enhance the study in future, we will include more diabetic patients and normal subjects to conclude that the our designed NIRS probe can be used to assess tissue oxygenation and to identify risk areas on foot sole significantly. Further the probe can be validated with the available clinical gold standard techniques.

Acknowledgment Authors are grateful to Science and Engineering Research Board (SERB), Ministry of Science and Technology, Govt. of India, New Delhi for providing financial support (ECR/2015/000161).

References

1. Leenders KL, Perani D, Lammertsma AA et al (1990) Cerebral blood flow, blood volume and oxygen utilization: normal values and effect of age. *Brain* 113(1):27–47
2. Cope M (1991) The development of a near infrared spectroscopy system and its application for non-invasive monitoring of cerebral blood and tissue oxygenation in the newborn infants. Doctoral dissertation, University of London
3. Alfano RR, Demos SG, Gayen SK (1997) Advances in optical imaging of biomedical media. *Ann N Y Acad Sci* 820(1):248–271
4. Delpy DT, Cope M (1997) Quantification in tissue near-infrared spectroscopy. *Philos Trans R Soc Lond Ser B Biol Sci* 352(1354):649–659
5. Chance B (1998) Near-infrared images using continuous, phase-modulated, and pulsed light with quantitation of blood and blood oxygenation. *Ann N Y Acad Sci* 838(1):29–45
6. Hoshi Y (2003) Functional near-infrared optical imaging: utility and limitations in human brain mapping. *Psychophysiology* 40(4):511–520
7. Torricelli A, Contini D, Dalla Mora A et al (2014) Neurophotonics: non-invasive optical techniques for monitoring brain functions. *Funct Neurol* 29(4):223
8. Pole Y (2002) Evolution of the pulse oximeter. *Int Congr Ser (Elsevier)* 1242:137–144
9. Zhang Y, Guo C, Zhao J, Yang C, Wang K, Sun J (2013) Non-invasive measurement of haemodynamic changes with a multi-wavelength NIRS system. *J Comp Info Syst* 9(13):5265–5272
10. Gay AN, Lazar DA, Stoll B et al (2011) Near-infrared spectroscopy measurement of abdominal tissue oxygenation is a useful indicator of intestinal blood flow and necrotizing enterocolitis in premature piglets. *J Pediatr Surg* 46(6):1034–1040
11. Li J, Zhang X (2014) A low-cost CCD-based imager for mapping venous oxygenation. Session 2A0, p 624
12. Khalil MA, Hoi J, Kim HK, Hielscher AH (2013) Dynamic contact-free continuous-wave diffuse optical tomography system for the detection of vascular dynamics within the foot. In SPIE BiOS International Society for Optics and Photonics 85781H-85781H
13. Bakker A, Smith B, Ainslie P, Smith K (2012) Near-infrared spectroscopy. In: Ainslie P (ed) *Applied aspects of ultrasonography in humans*. InTech, pp 65–76
14. Mancini DM, Bolinger L, Li H, Kendrick K, Chance B, Wilson JR (1994) Validation of near-infrared spectroscopy in humans. *J Appl Physiol* 77(6):2740–2747
15. Hampson NB, Piantadosi CA (1988) Near infrared monitoring of human skeletal muscle oxygenation during forearm ischemia. *J Appl Physiol* 64(6):2449–2457
16. Cavanagh PR, Rodgers MM, Liboshi A (1987) Pressure distribution under symptom-free feet during barefoot standing. *Foot Ankle* 7(5):262–278
17. Gerovasili V, Dimopoulos S, Tzanis G, Anastasiou-Nana M, Nanas S (2010) Utilizing the vascular occlusion technique with NIRS technology. *Int J Ind Ergon* 40(2):218–222
18. Lin OH, Lai JY, Tsai HY (2013) Preventing diabetes extremity vascular disease with blood oxygen saturation images. *Int J Instrum Sci* 2(A):1–7



Cellular and Molecular Response for Sensitising Cancer Cells and Protecting the Normal Cells from Radiation-Induced Damages

2

Shailender Gugalavath and Rama Rao Malla

Abstract

Research on cellular and molecular response of radiation in normal and cancer cells has been the focus with high priority during the past two decades. However, the simultaneous sensitisation of tumour cells and protection of normal cells is impeded due to high dose resistance to cancer cells and damage of normal cells during radiotherapy. This review discusses the recent advances on radiation-induced DNA damage and repair, cell cycle arrest as well as apoptosis, cellular sensitivity, bystander effect and genomic instability with cellular and molecular responses for sensitising cancer cells and protecting the normal cells against radiation-induced damages.

Keywords

DNA damage · Cell cycle arrest · Apoptosis · Genomic instability · Bystander effect

Abbreviations

APAF1	Apoptotic protease activating factor 1
CAFs	Cancer-associated fibroblasts
DD	Death domain
DISC	Death-inducing signalling complex
DSB	double-strand breaks
ECM	Extracellular matrix
FADD	Fas-associated death domain

S. Gugalavath · R. R. Malla (✉)
Cancer Biology Research Laboratory, Department of Biochemistry and Bioinformatics,
GITAM Institute of Science (Deemed to be University), Visakhapatnam, India
e-mail: ramarao.malla@gitam.edu

HR	Homologous recombination
MOMP	Mitochondrial outer membrane potential
NHEJ	Non-homologous end-joining
ROS	Reactive oxygen species
SSB	Single-strand breaks

2.1 Introduction

Radiation therapy is the most common mode of cancer treatment, which uses high energy beams to destroy cancer cells. However, exposure of adjacent normal cells to radiation during cancer radiation therapy causes adverse effects [1]. Therefore, it is essential to understand the cellular and molecular response to protect normal cells with a lesser complication from radiation and to sensitise the tumour cells by fractionated radiation. Radiotherapy has been greatly influenced by tumour microenvironment in which cancer cells have physical contact with extracellular matrix (ECM), fibroblasts and vascular vessels that influence the tumour cell behaviour. The studies on radiation-induced damage in normal fibroblasts are useful for identifying the cellular and molecular pathways involved in sensitising metastatic tumour cells and protecting the normal cells [2]. The knowledge of cellular and molecular pathways to radiation-induced damage helps to identify the new molecular targets. Understanding the response of normal fibroblasts and cancer-associated fibroblasts (CAFs) to radiation-induced cellular sensitivity, genomic instability, and bystander effect of radiation dramatically helps in the development of cancer therapeutics.

2.2 p⁵³ is Determinative of DNA Repair or Cell Death

Radiation induces various biological effects mainly by targeting nucleic acids, proteins and lipids in the cells which appear to be critical for cell survival. The DNA damage is initiated with ionization of the water molecule, followed by ROS generation. Hydroxyl radicals cause DSB as well as SSB by damaging the sugar-phosphates backbone [3].

Radiation exposed cells riposte DNA damage by employing ATM and ATR [4]. Inactive forms of ATM dimer dissociate as active monomers at DSB, which triggers autophosphorylation or transphosphorylation at Serine^{1,981} [5]. ATR is active at SSBs or stalled replication forks [6]. In rapid response to radiation, cell cycle transducers downstream to ATM degrade phosphorylated CDC25 by CHK1 and CHK2, which are activated by CDK2-CyclinE and CDK1-CyclinB complexes by inducing G1 as well as G2 phase arrests, respectively (Fig. 2.1) [7]. In delayed response, unstable MDM2-p⁵³ complex translocates from the cytosol to nucleus. The active p⁵³ transcribes p21 gene, which inhibits CDK4 and CDK6, as well as CDK1-cyclin B complex inducing G1 and G2 cell cycle arrest (Fig. 2.2) [8]. Furthermore,

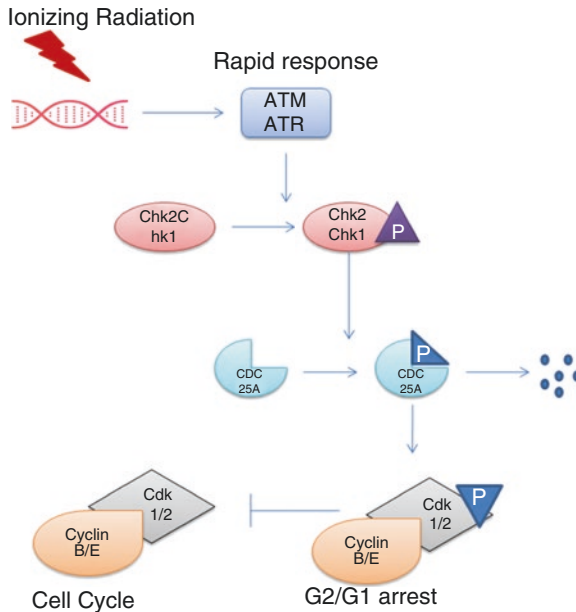


Fig. 2.1 Ionizing radiation induces directly double strands breaks or indirectly through radicals. Subsequently, the ATM/ATR kinase is activated through phosphorylation, and it activates the CHK1 and CHK2 causing phosphorylation of CDC25 isoforms, resulting in its degradation. As a consequence, CDC25 no longer activates CDK2 or CDK1, and thus the cell cycle is stopped in the G1 and G2 phases, respectively

the fate of cell survival and cell death is monitored by p⁵³ phosphorylation at Serine¹⁵, which causes cell cycle arrest, and additional phosphorylation at Serine⁴⁶ induces cell death [9]. These signify the role of p⁵³ as ‘guardian of the genome’ [10].

2.3 DNA Repair

The paused cell cycle enables the damaged DNA to undergo repair through NHEJ and HR [11]. NHEJ randomly repairs DSBs independent of homology during the G1 phase [12]. In NHEJ, the heterodimer Ku70-Ku80 recognizes the DSB and recruits the catalytic subunit of DNA PK holoenzyme and γ H2AX stabilizes the broken ends of DNA. In the ATM pathway, Ku also protects DSB ends by activating 53BP1. DNA-PK holoenzyme and ATM additionally recruit the processing enzymes of DSB repair machinery, and XRCC4/Ligase IV mediates the ligation of the DSB [13, 14].

HR is a standard error-free mechanism of DNA repair but requires extensive homology. In this mechanism, the DNA is repaired frequently through gene conservative rarely by non-conservative annealing mechanisms at late S and G2 phases [11]. In HR pathway protein kinases, ATM and ATR mediate DNA damage response, phosphorylate downstream BRCA1, BRCA2 and assist the formation of RAD51–BRCA1/BRCA2 complex. This complex helps RAD 51 to bind to ssDNA. RAD51

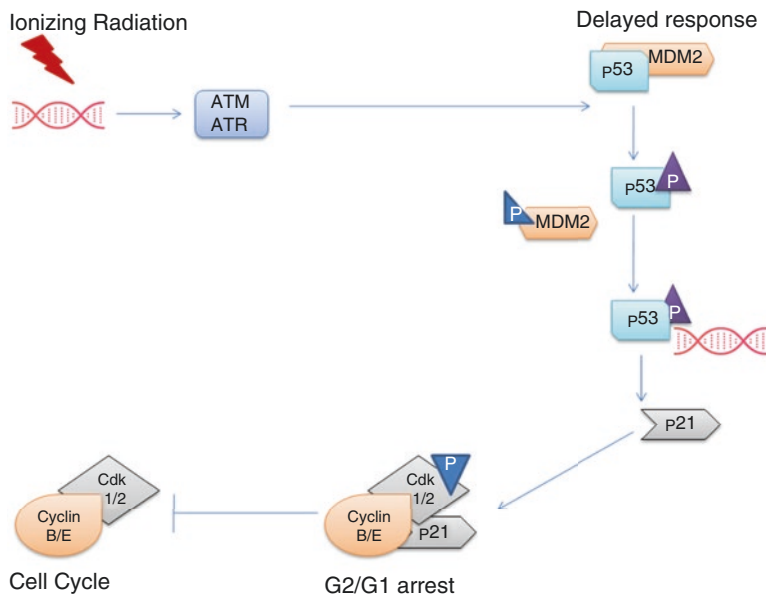


Fig. 2.2 Ionizing radiation induces directly double strands breaks or indirectly through radicals. Subsequently, the ATM/ATR kinase is activated through phosphorylation and this activates p⁵³ causing phosphorylation of p⁵³ and serves as a transcription factor to p⁵³ which inactivates CDK1/CDH2 + CyclinB/E complex by phosphorylation, thus causing cell cycle arrest at G1 and G2 phases, respectively

plays a regulatory function, which forms the nucleoprotein filament on DNA for strand exchange.

Furthermore, DNA end-joining process is mediated by MRN complex in combination with CTIP. The CTIP restricts the HR by phosphorylating at S as well as G2 phases. Therefore, RAD 51 and its upstream mediators have a significant role in repair mechanism [15]. After repair of the SSB and DSB, pausing at point stops and cell cycle continues.

2.4 Apoptosis

The failure of DNA repair mechanism leads to induction of apoptosis. The mitochondria-mediated apoptosis pathway involves interactions of pro- as well as antiapoptotic Bcl-2 proteins, whereas the extrinsic mechanisms are mediated by FADD, a death receptor of the TNF-R family as well as caspase-8 [16].

Intrinsic apoptosis pathway disrupts the function of mitochondrial membrane and is further regulated by the Bcl-2 family and nuclear p⁵³ [17]. Nuclear p⁵³ regulates the expression of proapoptotic proteins Noxa, Bax and Puma [18]. After translocation to cytoplasm, p⁵³ forms complex with Bcl-2 [19]. Puma disrupts the p⁵³-Bcl-2 complex and liberates the p⁵³-induced apoptosis by promoting the formation of Bax-Bak pores by subsequent releases of cytochrome C through the

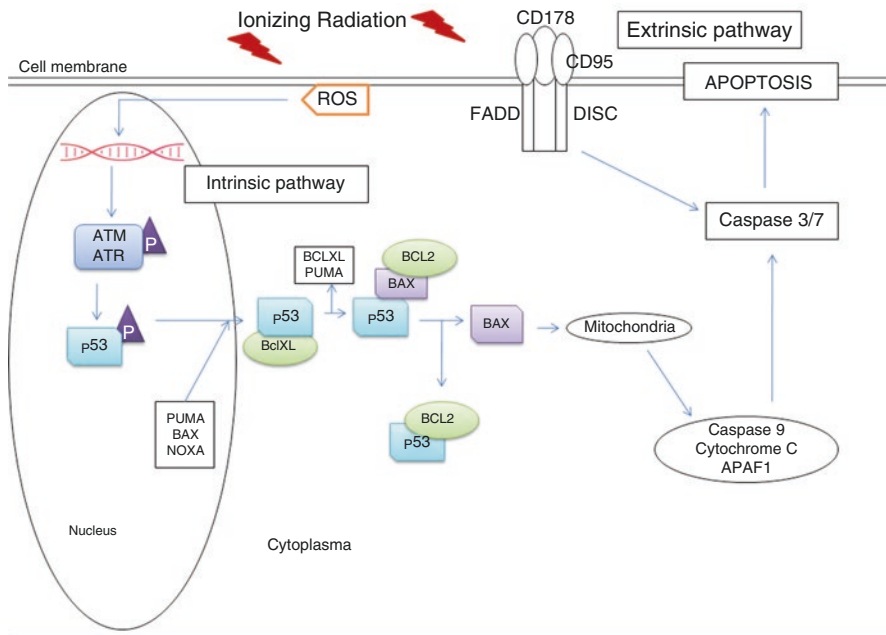


Fig. 2.3 Radiation induces the radical activity that causes the DNA DSB which leads to ATM activation by phosphorylating p^{53} along with BAX, PUMA and NOXA and further triggers the mitochondrial changes leading to caspase dependent apoptosis, which is controlled by p^{53} directing to intrinsic pathway. The extrinsic pathway is independent on of p^{53} , radiation activates the CD95/CD178 which causes the triggering of caspase activation leading to apoptosis

mitochondrial outer membrane. The released cytochrome c activates APAF1 as well as apoptosome with caspase-9 in the cytosol [20].

The radiation-induced extrinsic apoptotic pathway involves ligand-dependent membrane-bound TNF receptor family members [21, 22]. In these pathways, p^{53} causes upregulation and transactivation of the CD95 receptors [23]. CD178 binding causes CD95 ligand trimerization from DD and recruits the FADD [24]. FADD activates caspases-8 by the mitochondria-independent mechanism by forming the DISC. It can also precede mitochondria-dependent apoptotic mechanisms by the activated caspases-3/7 leading via activated the caspases-8/9 [25]. Therefore, signalling molecules mediating apoptosis as well as cell cycle are promising targets of radio-sensitization approach (Fig. 2.3).

2.5 Radiation-Induced Cellular Sensitivity

Several strategies with different approaches by fractionated dose, sensitivity, genomic instability, bystander effect by fibroblasts are reported below. The sensitivity of fibroblasts to radiation varies with dose, time of exposure and origin of cells.

Table 2.1 Sensitivity to radiation compared to the normal fibroblast

S.No	Fibroblast type	Dose	Response	References
1	Fibroblasts from fanconi anaemia patients	1–2 Gy (HDR), 0.1 Gy (LDR)	Cellular sensitivity showing no recovery of the DNA damage defect at HDR and better chance recovery at LDR	[26]
2	Human skin fibroblasts from retinoblastoma patients	0.13 Gy	Cellular sensitivity and radiation-induced G1 arrest	[27]
3	Normal human fore skin fibroblasts	0.04–0.14 Gy	Dose-dependent protein expression	[28]
4	Fibroblast cells from nevoid basal cell carcinoma syndrome	2.58 Gy	High cellular sensitivity due to failure of the DNA replication	[29]
5	Cultured human fibroblasts	UV-A (334 nm, 365 nm) and near-visible (405 nm)	Singlet oxygen-mediated lethal action	[30]
6	Fibroblasts from retinoblastoma patients	1.8 Gy	High sensitivity due to defect in DNA repair	[31]
7	Xeroderma pigmentosum fibroblasts	5–1 Gy	Decreased sensitivity	[32]
8	Human fibroblast	1.07 Gy (HDR), 0.0109 Gy(LDR)	Cellular sensitivity correlated with DNA residual levels	[33]
9	Cultured fibroblasts from non-Hodgkin's lymphoma patients	4.6 Gy	Cellular and chromosomal sensitivity	[34]

The fibroblast isolated from various cancer patients showed more sensitivity to radiation compared to the normal fibroblasts (Table 2.1).

2.6 Radiation-Induced Genomic Instability

In multicellular organisms, instability in the genome is central to carcinogenesis. The enhanced alterations in the genome lead to genomic instability [35]. Studies from various laboratories demonstrated radiation-induced DNA lesions including SSB, DSB and base modifications directly through absorption of energy or indirectly through ROS generation [36]. Radiation-induced DNA damage could be transmitted to multiple generations from the survived cells [37]. Recently, NASA reported that a low dose of γ rays caused DNA damage in human fibroblasts [38]. Transformed neoplastic mouse fibroblasts showed genome liability at 8Gy X-ray radiation [39]. Exposure of cultured human skin fibroblasts to laser radiation at

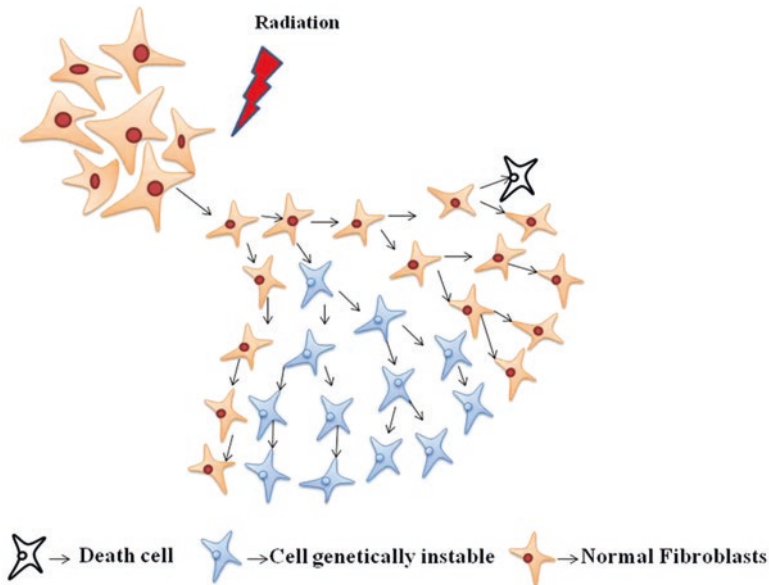


Fig. 2.4 Schematic presentation of radiation-induced genomic instability in fibroblasts. Among the progeny of surviving cells, various types of delayed phenotypes are expressed, but not uniformly, over several generations after radiation. Delayed manifestations of induced genomic instability include delayed cell death and chromosomal instability

sub-lethal doses of either 193- or 248-nm resulted in genotoxicity [40]. Magnander et al. investigated the damage and repair of clustered DNA and reported the influences of structural difference on the organization of chromatin [41]. They said that the induction of DSBs and clustered damage occurs in human fibroblasts at 13.5 Gy X-radiation. Al-Khodairy et al. demonstrated that primary skin fibroblasts are sensitive to UV (254 nm) radiation at an average of 4.6 Jm² and showed a defect in DNA repair mechanism [42]. Hannan et al. showed a deficiency in DNA repair, potentially lethal damage repair that leads to genomic instability in cultured skin fibroblasts at low dose γ -radiation(0.007 Gy/min) [43]. Normal human fibroblasts showed about 50% chromosome aberrations when X-ray irradiated at 6 Gy [44]. Human lung fibroblasts showed DNA damage and reversible cell cycle arrest at 4 Gy radiation but cellular senescence at 50 Gy radiation [45]. Desphande et al. reported that the chromosomal instability (Sister Chromatin exchange) in α particles exposed normal human diploid fibroblasts [46]. Mahrhofer et al. reported that X-radiation induces various levels of γ -H2AX formation in primary skin fibroblasts of healthy individuals as well as breast cancer patients [47]. Radiation-mediated genomic instability of fibroblasts showed delayed cell death and it carried genomic instability to further generation (Fig. 2.4).

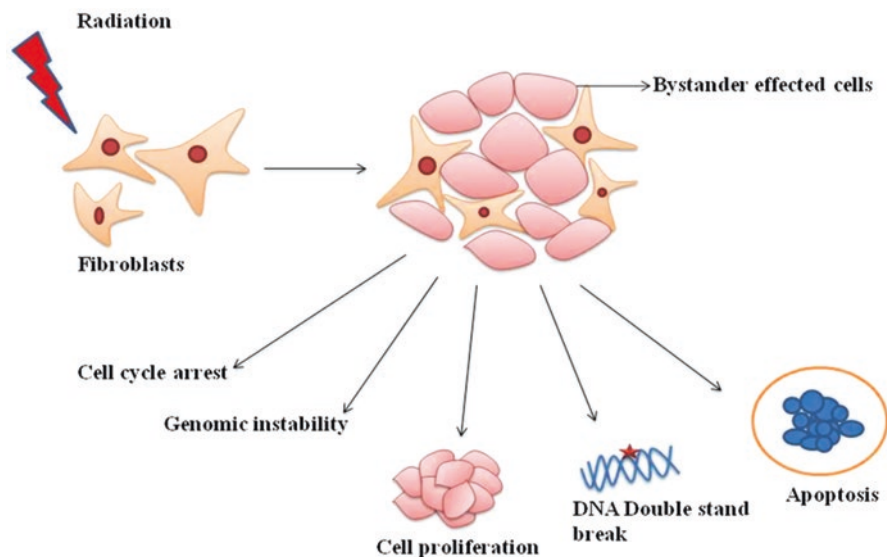


Fig. 2.5 Illustration of radiation induced bystander effect in fibroblasts resulting in the operation of molecular signals secreted by irradiated cells and non-irradiated cells causing the cycle arrest, genomic instability, cell proliferation, and DNA double-strand break and apoptosis

2.7 Radiation-Induced Bystander Effect

The healthy cells close to irradiated cells exhibit a radiation-related bystander effect (Fig. 2.5). In such a scenario, extranuclear as well as extracellular events contribute to radiation-induced biological consequences of radiation [48]. The bystander effect is extensively reported in cultured cells, however, and quite a few studies reported in *in vivo* system [49]. The X-radiation mediated bystander effect induces expression of extracellular signalling proteins and alters the expression of interleukins associated with apoptosis in normal rat fibroblasts [50]. Pereira et al. reported that at the chronic low dose of ^{137}Cs γ -rays (0.01–0.1 Gy) showed the DNA DSB in embryonic zebrafish fibroblasts [51]. Widel et al. reported that X-radiation (2–4 Gy) induced apoptosis in normal human dermal fibroblasts co-cultured with Me45 malignant melanoma cell [52]. Neonatal human dermal fibroblasts showed the reduced survival, enhanced the frequency of apoptosis release of ROS, and IL-6 by UV-induced bystander effect [53]. Fibroblasts exposed how X-irradiation induced the expression of mitotic genes and proliferation of primary human mammary co-cultured breast carcinoma cells [54]. Fibroblasts induced by bystander effects showed expression of growth marker Ki-67 in squamous cell carcinoma; invasive markers c-Met, Ras, MAPKinases, MMP-1 and MMP-9 and p^{53} -binding protein 1 (53BP1) [55]. Irradiation of normal human lung fibroblasts with α -particle-induced bystander effect on the expression of p^{53} and NFkB-regulated genes [56]. Ohuchida et al. reported that irradiated stromal fibroblasts interacted with tumour cells and enhanced the invasion of pancreatic carcinoma [57]. Belyakov et al. showed the

direct evidence of ionising radiation-mediated bystander effect in human primary fibroblasts [58]. Iyer and Lehnert showed increased survival, decreased TP⁵³, as well as CDKN1A levels in human normal lung fibroblasts cultured with supernatant from alpha-irradiated fibroblasts [59]. The chromosomal radiosensitivity of the cultured fibroblasts from non-Hodgkin's lymphoma patients increased with the dose of 4.6 Gy when compared to normal fibroblasts [34].

2.8 Conclusion

From the last two decades, knowledge on radiation-induced response has been increased. However detailed mechanism on complete interaction and regulatory mechanisms that help cells to survive and towards the apoptosis is not well understood. In spite of that, current knowledge for the development of the radio-sensitizing therapeutic approaches has to be highly promising to target cancer-associated fibroblasts and vice versa for the protection of normal fibroblast cells. This can be achieved by scavenging of reactive species, increasing the cell survival, adhesion of fibroblast to cancer cells, cell cycle arrest, or reduction of apoptosis. This combination approach creates more opportunities for widening the therapeutic application of radiotherapy as the most successful method for the treatment of cancer with simultaneous protection of healthy cells from radiation.

Acknowledgements This review was supported by GITAM (Deemed to be University) and Defence Research & Development Organization – Life Sciences Research Board (File No: CC R&D (TM)/81/48222/LSRB-282/SH&DD2014 Dated 08-12-2014), India.

Conflict of Interest The authors declare that they have no conflict of interest.

References

1. Barnett GC, West CM, Dunning AM, Elliott RM, Coles CE, Pharoah PD et al (2009) Normal tissue reactions to radiotherapy: towards tailoring treatment dose by genotype. *Nat Rev Cancer* 9(2):134–142
2. Maier P, Wenz F, Herskind C (2014) Radioprotection of normal tissue cells. *Strahlentherapie und Onkologie: Organ der Deutschen Röntgengesellschaft [et al]* 190(8):745–752
3. Herskind C, Westergaard O (1988) Variable protection by OH scavengers against radiation-induced inactivation of isolated transcriptionally active chromatin: the influence of secondary radicals. *Radiat Res* 114(1):28–41
4. Marechal A, Zou L (2013) DNA damage sensing by the ATM and ATR kinases. *Cold Spring Harb Perspect Biol* 5(9):a012716
5. Bakkenist CJ, Kastan MB (2003) DNA damage activates ATM through intermolecular autophosphorylation and dimer dissociation. *Nature* 421(6922):499–506
6. Stokes MP, Rush J, Macneill J, Ren JM, Sprott K, Nardone J et al (2007) Profiling of UV-induced ATM/ATR signaling pathways. *Proc Natl Acad Sci U S A* 104(50):19855–19860
7. Donzelli M, Draetta GF (2003 Jul) Regulating mammalian checkpoints through Cdc25 inactivation. *EMBO Rep* 4(7):671–677

8. Abbas T, Dutta A (2009) p21 in cancer: intricate networks and multiple activities. *Nat Rev Cancer* 9(6):400–414
9. Zhang XP, Liu F, Wang W (2011) Two-phase dynamics of p⁵³ in the DNA damage response. *Proc Natl Acad Sci U S A* 108(22):8990–8995
10. Lane DP (1992) Cancer. p⁵³, guardian of the genome. *Nature* 358(6381):15–16
11. Chapman JR, Taylor MR, Boulton SJ (2012) Playing the end game: DNA double-strand break repair pathway choice. *Mol Cell* 47(4):497–510
12. Lieber MR (2010) The mechanism of double-strand DNA break repair by the nonhomologous DNA end-joining pathway. *Annu Rev Biochem* 79:181–211
13. Davis AJ, Chen DJ (2013) DNA double strand break repair via non-homologous end-joining. *Transl Cancer Res* 2(3):130–143
14. Ma Y, Pannicke U, Schwarz K, Lieber MR (2002) Hairpin opening and overhang processing by an Artemis/DNA-dependent protein kinase complex in nonhomologous end joining and V(D)J recombination. *Cell* 108(6):781–794
15. Gudmundsdottir K, Ashworth A (2006) The roles of BRCA1 and BRCA2 and associated proteins in the maintenance of genomic stability. *Oncogene* 25(43):5864–5874
16. Takasawa R, Nakamura H, Mori T, Tanuma S (2005) Differential apoptotic pathways in human keratinocyte HaCaT cells exposed to UVB and UVC. *Apoptosis* 10(5):1121–1130
17. Tait SW, Green DR (2010) Mitochondria and cell death: outer membrane permeabilization and beyond. *Nat Rev Mol Cell Biol* 11(9):621–632
18. Dogu Y, Diaz J (2009) Mathematical model of a network of interaction between p⁵³ and Bcl-2 during genotoxic-induced apoptosis. *Biophys Chem* 143(1–2):44–54
19. Lomonosova E, Chinnadurai G (2008) BH3-only proteins in apoptosis and beyond: an overview. *Oncogene* 27(Suppl 1):S2–S19
20. Wolff S, Erster S, Palacios G, Moll UM (2008) p⁵³'s mitochondrial translocation and MOMP action is independent of Puma and Bax and severely disrupts mitochondrial membrane integrity. *Cell Res* 18(7):733–744
21. Harms K, Nozell S, Chen X (2004) The common and distinct target genes of the p⁵³ family transcription factors. *Cell Mol Life Sci* 61(7–8):822–842
22. Muller M, Strand S, Hug H, Heinemann EM, Walczak H, Hofmann WJ et al (1997) Drug-induced apoptosis in hepatoma cells is mediated by the CD95 (APO-1/Fas) receptor/ligand system and involves activation of wild-type p⁵³. *J Clin Invest* 99(3):403–413
23. Muller M, Wilder S, Bannasch D, Israeli D, Lehlbach K, Li-Weber M et al (1998) p⁵³ activates the CD95 (APO-1/Fas) gene in response to DNA damage by anticancer drugs. *J Exp Med* 188(11):2033–2045
24. Scaffidi C, Fulda S, Srinivasan A, Friesen C, Li F, Tomaselli KJ et al (1998) Two CD95 (APO-1/Fas) signaling pathways. *EMBO J* 17(6):1675–1687
25. Yang F, Stenoien DL, Strittmatter EF, Wang J, Ding L, Lipton MS et al (2006) Phosphoproteome profiling of human skin fibroblast cells in response to low- and high-dose irradiation. *J Proteome Res* 5(5):1252–1260
26. Burnet NG, Wurm R, Tait DM, Peacock JH (1994) Cellular sensitivity and low dose-rate recovery in Fanconi anaemia fibroblasts. *Br J Radiol* 67(798):579–583
27. Fitzek MM, Dahlberg WK, Nagasawa H, Mukai S, Munzenrider JE, Little JB (2002) Unexpected sensitivity to radiation of fibroblasts from unaffected parents of children with hereditary retinoblastoma. *Int J Cancer* 99(5):764–768
28. Hauptmann M, Haghdoost S, Gomolka M, Sarioglu H, Ueffing M, Dietz A et al (2016) Differential response and priming dose effect on the proteome of human fibroblast and stem cells induced by exposure to low doses of ionizing radiation. *Radiat Res* 185(3):299–312
29. Chan GL, Little JB (1983) Cultured diploid fibroblasts from patients with the nevoid basal cell carcinoma syndrome are hypersensitive to killing by ionizing radiation. *Am J Pathol* 111(1):50–55
30. Tyrrell RM, Pidoux M (1989) Singlet oxygen involvement in the inactivation of cultured human fibroblasts by UVA (334 nm, 365 nm) and near-visible (405 nm) radiations. *Photochem Photobiol* 49(4):407–412

31. Weichselbaum R, Albert D, Cassady J, Little J (1983) An in vitro investigation of x-ray sensitivity in fibroblasts from patients with retinoblastoma. *Invest Ophthalmol Vis Sci* 24(7):958–961
32. Arlett CF, Green MH, Rogers PB, Lehmann AR, Plowman PN (2008) Minimal ionizing radiation sensitivity in a large cohort of xeroderma pigmentosum fibroblasts. *Br J Radiol* 81(961):51–58
33. Zhou PK, Sproston AR, Marples B, West CM, Margison GP, Hendry JH (1998) The radio-sensitivity of human fibroblast cell lines correlates with residual levels of DNA double-strand breaks. *Radiother Oncol* 47(3):271–276
34. Waghray M, Sigut D, Einspinner M, Kunhi M, al-Sedairy ST, Hannan MA (1992) Chronic gamma-irradiation results in increased cell killing and chromosomal aberration with specific breakpoints in fibroblast cell strains derived from non-Hodgkin's lymphoma patients. *Mutat Res* 284(2):223–231
35. Morgan WF, Day JP, Kaplan MI, McGhee EM, Limoli CL (1996) Genomic instability induced by ionizing radiation. *Radiat Res* 146(3):247–258
36. Ward JF (1988) DNA damage produced by ionizing radiation in mammalian cells: identities, mechanisms of formation, and reparability. *Prog Nucleic Acid Res Mol Biol* 35:95–125
37. Tomita M, Maeda M (2015) Mechanisms and biological importance of photon-induced bystander responses: do they have an impact on low-dose radiation responses. *J Radiat Res* 56(2):205–219
38. Lu T, Zhang Y, Wong M, Feiveson A, Gaza R, Stoffle N et al (2017) Detection of DNA damage by space radiation in human fibroblasts flown on the International Space Station. *Life Sci Space Res* 12:24–31
39. Crompton NE, Sigg M, Jaussi R (1994) Genome lability in radiation-induced transformants of C3H 10T1/2 mouse fibroblasts. *Radiat Res* 138(1 Suppl):S105–S108
40. Rimoldi D, Miller AC, Freeman SE (1991) Samid D. DNA damage in cultured human skin fibroblasts exposed to excimer laser radiation. *J Invest Dermatol* 96(6):898–902
41. Magnander K, Hultborn R, Claesson K, Elmroth K (2010) Clustered DNA damage in irradiated human diploid fibroblasts: influence of chromatin organization. *Radiat Res* 173(3):272–282
42. Al-Khodayry FM, Kunhi M, Siddiqui YM, Arif JM, Al-Ahdal MN, Hannan MA (2004) Defective repair of UV-induced DNA damage in cultured primary skin fibroblasts from Saudi thyroid cancer patients. *Asian Pac J Cancer Prev APJCP* 5(2):139–143
43. Hannan MA, Siddiqui Y, Rostom A, Al-Ahdal MN, Chaudhary MA, Kunhi M (2001) Evidence of DNA repair/processing defects in cultured skin fibroblasts from breast cancer patients. *Cancer Res* 61(9):3627–3631
44. Borgmann K, Dede M, Wrona A, Brammer I, Overgaard J, Dikomey E (2004) For X-irradiated normal human fibroblasts, only half of cell inactivation results from chromosomal damage. *Int J Radiat Oncol Biol Phys* 58(2):445–452
45. Papadopoulou A, Kletsas D (2011) Human lung fibroblasts prematurely senescent after exposure to ionizing radiation enhance the growth of malignant lung epithelial cells in vitro and in vivo. *Int J Oncol* 39(4):989–999
46. Deshpande A, Goodwin EH, Bailey SM, Marrone BL, Lehnert BE (1996) Alpha-particle-induced sister chromatid exchange in normal human lung fibroblasts: evidence for an extra-nuclear target. *Radiat Res* 145(3):260–267
47. Mahrhofer H, Burger S, Oppitz U, Flentje M, Djuzenova CS (2006) Radiation induced DNA damage and damage repair in human tumor and fibroblast cell lines assessed by histone H2AX phosphorylation. *Int J Radiat Oncol Biol Phys* 64(2):573–580
48. Hei TK, Zhou H, Ivanov VN, Hong M, Lieberman HB, Brenner DJ et al (2008) Mechanism of radiation-induced bystander effects: a unifying model. *J Pharm Pharmacol* 60(8):943–950
49. Mancuso M, Pasquali E, Leonardi S, Tanori M, Rebessi S, Di Majo V et al (2008) Oncogenic bystander radiation effects in Patched heterozygous mouse cerebellum. *Proc Natl Acad Sci U S A* 105(34):12445–12450
50. Babini G, Bellinzona VE, Morini J, Baiocco G, Mariotti L, Unger K et al (2015) Mechanisms of the induction of apoptosis mediated by radiation-induced cytokine release. *Radiat Prot Dosim* 166(1–4):165–169

51. Pereira S, Malard V, Ravanat JL, Davin AH, Armengaud J, Foray N et al (2014) Low doses of gamma-irradiation induce an early bystander effect in zebrafish cells which is sufficient to radioprotect cells. *PLoS One* 9(3):e92974
52. Widel M, Krzywon A, Gajda K, Skonieczna M, Rzeszowska-Wolny J (2014) Induction of bystander effects by UVA, UVB, and UVC radiation in human fibroblasts and the implication of reactive oxygen species. *Free Radic Biol Med* 68:278–287
53. Widel M, Przybyszewski WM, Cieslar-Pobuda A, Saenko YV, Rzeszowska-Wolny J (2012) Bystander normal human fibroblasts reduce damage response in radiation targeted cancer cells through intercellular ROS level modulation. *Mutat Res* 731(1–2):117–124
54. Tsai KK, Stuart J, Chuang YY, Little JB, Yuan ZM (2009) Low-dose radiation-induced senescent stromal fibroblasts render nearby breast cancer cells radioresistant. *Radiat Res* 172(3):306–313
55. Kamoichi N, Nakashima M, Aoki S, Uchihashi K, Sugihara H, Toda S et al (2008) Irradiated fibroblast-induced bystander effects on invasive growth of squamous cell carcinoma under cancer-stromal cell interaction. *Cancer Sci* 99(12):2417–2427
56. Ghandhi SA, Yaghoubian B, Amundson SA (2008) Global gene expression analyses of bystander and alpha particle irradiated normal human lung fibroblasts: synchronous and differential responses. *BMC Med Genet* 1:63
57. Ohuchida K, Mizumoto K, Murakami M, Qian LW, Sato N, Nagai E et al (2004) Radiation to stromal fibroblasts increases invasiveness of pancreatic cancer cells through tumor-stromal interactions. *Cancer Res* 64(9):3215–3222
58. Belyakov OV, Malcolmson AM, Folkard M, Prise KM, Michael BD (2001) Direct evidence for a bystander effect of ionizing radiation in primary human fibroblasts. *Br J Cancer* 84(5):674–679
59. Iyer R, Lehnert BE, Svensson R (2000) Factors underlying the cell growth-related bystander responses to alpha particles. *Cancer Res* 60(5):1290–1298



A Novel Approach for Production and Study of Medical Ultrasound from Low-Cost Electromagnetic Transducers

Srijeet Chatterjee, Priyam Biswas, and Pratik Das

Abstract

Medical ultrasound is generally produced via piezoelectric crystals, and the probes are quite costly, due to which overall cost of diagnosis and therapy increases immensely. Our aim was to develop a low-cost ultrasound probe. We thereafter successfully produced ultrasound from low-cost electromagnetic loud speakers available locally in the market. The presence of ultrasound was tested at a range of 40 kHz via resonating crystals at the receiver end, which was observed in a CRO. Using advanced Matlab programming the interpolation was for the output ultrasound which was received with respect to the input voltage from the frequency generator. The voltage level was calibrated with the output waveform amplitude, and a plot was obtained which can give exact values for desired ultrasound peak values. Significance of the 40 KHz frequency includes ultrasound-assisted photo catalysis of chemicals, such as methylene blue, and particle image velocimetry.

Keywords

Ultrasound · Affordable · Electromagnetic · Lagrange

3.1 Introduction

Ultrasound is a kind of sound which has a frequency directly beyond the audible range, and the frequency range is from 20 Hz to 20 kHz. Sound is kind of mechanical energy and it needs a medium to travel. Thus, in divergence to electromagnetic

S. Chatterjee · P. Biswas

Netaji Subhash Engineering College, TIG, MAKAUT, Kolkata, India

P. Das (✉)

School of Bioscience and Engineering, Jadavpur University, Kolkata, India

waves, it cannot travel in void. The frequencies typically applied in medical imaging lie between 1 MHz and 20 MHz [1]. This type of sound is produced by a transducer that primarily actions as a loudspeaker transferring out an acoustic pulse along a thin beam in a specified track. The transducer consequently works as a microphone in the demand to record the acoustic echoes produced by the tissue along the pathway of the released pulse. These echoes thus bring statistics about the acoustic properties of the tissue along the pathway [2]. The discharge of acoustic energy and the recording of the echoes generally take place at the same transducer, in dissimilarity to CT imaging, where the emitter (the X-ray tube) and recorder (the detectors) are positioned on the differing side of the patient.

Ultrasound (including sound) prerequisites a medium, where it can propagate by means of local distortion of the medium. The medium can be thought of being made of small spheres (e.g., molecules or atom) that are linked with coils. While mechanical energy is transferred through such a medium, the small spheres connected through coils will oscillate about their latent position. Thus, the transmission of sound is owing to an uninterrupted exchange between kinetic energy and potential energy, associated to the density and elastic properties of the medium, respectively. The two waves that exist in solids are longitudinal waves where the particle movements occur in the same way of the propagation (or energy flow) and transversal (or shear waves) in which the movements occur in a plane perpendicular to the way of propagation. In water and soft tissue, the waves present are mainly longitudinal. The frequency, f , of the particle oscillation, is correlated to the wavelength, λ , and the propagation velocity c [3]:

$$\lambda f = c$$

The speed of sound in soft tissue at around 37°C is 1540 m/s; thus, at a frequency of 7.5 MHz, the wavelength is expected to be 0.2 mm. In order to mimic ultrasonic frequencies, people have yoked the electrical assets of materials. When an exclusively cut piezoelectric quartz crystal is compressed, the crystal turns out to be electrically charged, and an electric current is produced: the electric current is directly proportional to the pressure applied [4]. If the crystal is abruptly stretched, the direction of the current will reverse itself. Consecutively compressing and stretching the crystal have the consequence of producing an alternating current.

When an alternating current is applied to the crystal that matches the natural frequency of the crystal, the crystal is able to be made to expand and contract with the help of the applied alternating current. When a crystal is subjected to such current, ultrasonic waves are formed [5]. Most of the time, ultrasonic waves are produced by a transducer that comprises a piezoelectric crystal that converts electrical energy (electric current) to mechanical energy (sound waves). The sound waves are reflected and return to the transducer as echoes and are transformed back to electrical signals by the similar transducer or by a different one. Other than this, ultrasonic waves can be created by means of magnetostriction (from magneto, meaning magnetic, and strictio, meaning drawing together). In such case, an iron or nickel element is magnetized to modify its dimensions, thereby generating ultrasonic waves. Ultrasound may also be generated by a whistle or siren-type originator. In this technique, gas or

liquid streams are delivered through a resonant cavity or reflector with the effect that ultrasonic vibrations characteristic of the specific gas or liquid are created.

This work aims to produce ultrasound from a low-cost electromagnetic loud speaker available locally in the market and hence generating ultrasound very economically.

3.2 Methodology

In our experiment, we have used a commercially available frequency generator to generate a frequency of 40 KHz, which is an appropriate range for ultrasound. The output from the frequency synthesizer can be varied in between 0 and 5 V. The test was mainly conducted using sine wave (Figs. 3.1, 3.2 and 3.3).

Fig. 3.1 40 KHz sine wave (0–5 V)

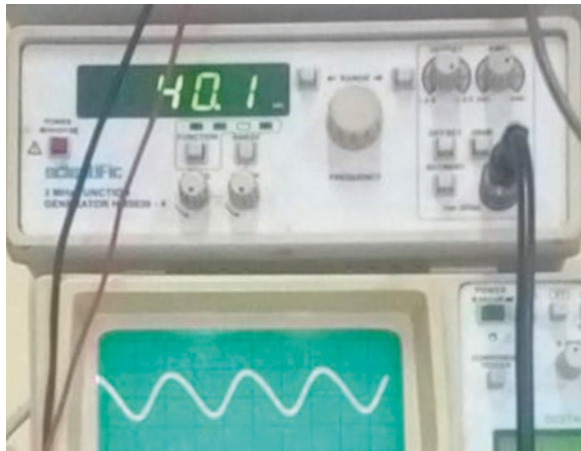


Fig. 3.2 Low-cost speaker

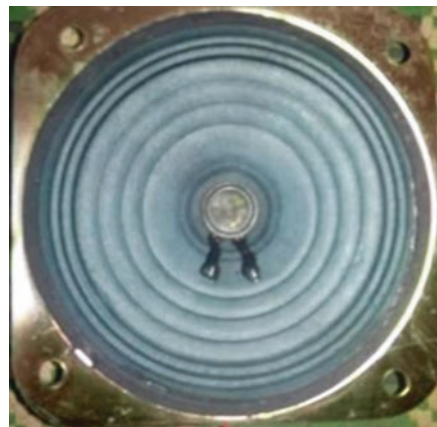


Fig. 3.3 Piezoelectric receiver unit



A low-cost electromagnetic loud speaker available locally in the market with 4 ohm resistance and 5 watt power consumption rating, price approximately 35/- INR was used for the experiment. {Se-yuen, 2003 #452}. A resonating crystal of 40 KHz was selected as the receiving transducer to verify whether electromagnetic speakers can truly emit ultrasound frequencies. The receiver unit consists of three major blocks.

- First there is the piezoelectric receiver input, which is resonating at a frequency of 40 KHz.
- Next is the preamplifier unit, which compensates the losses and ensures that the transduced frequency is fed to the output of this unit; here we have taken an approximation for practical purpose. The output of the electromagnetic transmitter unit is relatively less compared to the input of the frequency generator. Considerations have been made regarding the preamplifier section that it only compensates the losses that occur due to receiver end, and hence no effect on the output of the electromagnetic transducer is observed (Nelkon 1978 #453). This has been verified using the original setup where the receiver unit is a part of complete transmitter and receiver set.
- Last is the output to the CRO.

Now from the frequency generator in 0.5 V steps, a frequency of 40 KHz was fed to the electromagnetic transducer. Keeping negligible distance between the transducer and receiver unit, the reading was observed from the CRO. Hereby we ensured that a simple electromagnetic sound speaker was converted to a very low-cost ultrasound transducer which can be utilized for a vast range of activities, but our prime focus was on biomedical applications since power rating and voltage rating were quite low.

Next we took all our data and tried to derive an equation establishing relationship between the input voltage from the frequency generator and the output voltage from the receiver unit, which replicates the transducer output (Fig. 3.4).

3.3 Observation

In our experiment, we took two data sets, with 0.5 V steps, one while increasing the voltage of frequency generator from 0V to 5V and another we took while decreasing the frequencies from 5V to 0V; both were observed at 40 KHz frequency and,



Fig. 3.4 Negligible distance between transducer and receiver ensures no loss while propagation



Fig. 3.5 The complete setup

having found nearly the same values, an average of the two was considered and plotted against the output voltage obtained from the receiver end. All the frequencies were sinusoidal waves (Fig. 3.5 and Table 3.1).

3.4 Results

We did a computation in MATLAB using Lagrange numerical methods and obtained an equation and a curve stating the relationship of input and output voltages. The equation, plot, and algorithm are stated below (Figs. 3.6, 3.7 and 3.8):

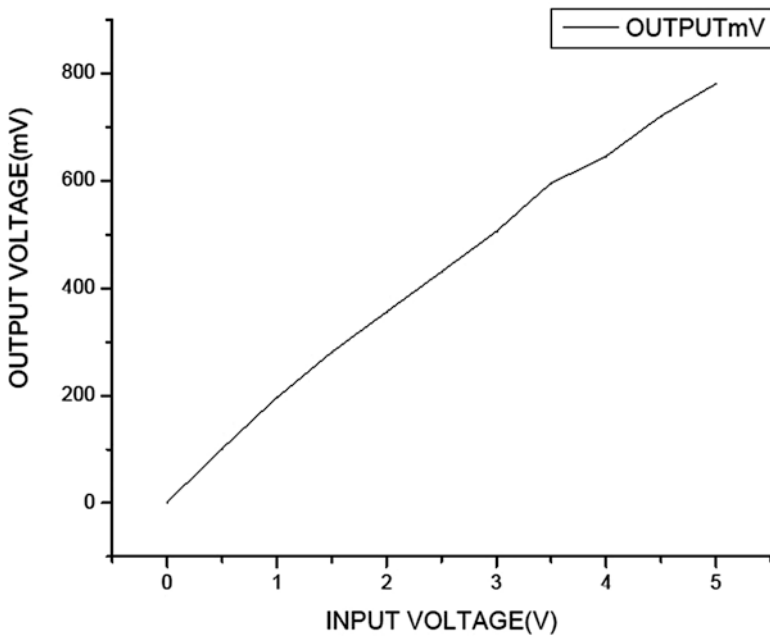
1. Equation obtained:

$$f(x) = -0.671605x^{10} + 16.1905x^9 - 166.931x^8 + 962.444x^7 - 3403.79x^6 + 7612.69x^5 - 10681.9x^4 + 8969.42x^3 - 4044.17x^2 + 931.75x$$

Table 3.1 Input vs output voltage

Input voltage (Volts)	Output voltage (mV) ↑	Output voltage (mV) ↓	Output voltage Avg. (mV)
0.0	0	0	0
0.5	95	105	100
1.0	200	190	195
1.5	280	280	280
2.0	355	355	355
2.5	435	425	430
3.0	500	510	505
3.5	595	595	595
4.0	650	640	645
4.5	730	710	720
5.0	780	780	780

2. Graphical representation:

**Fig. 3.6** Output voltage vs input voltage

3. Algorithm of Lagrange numerical method to find the equation and plot

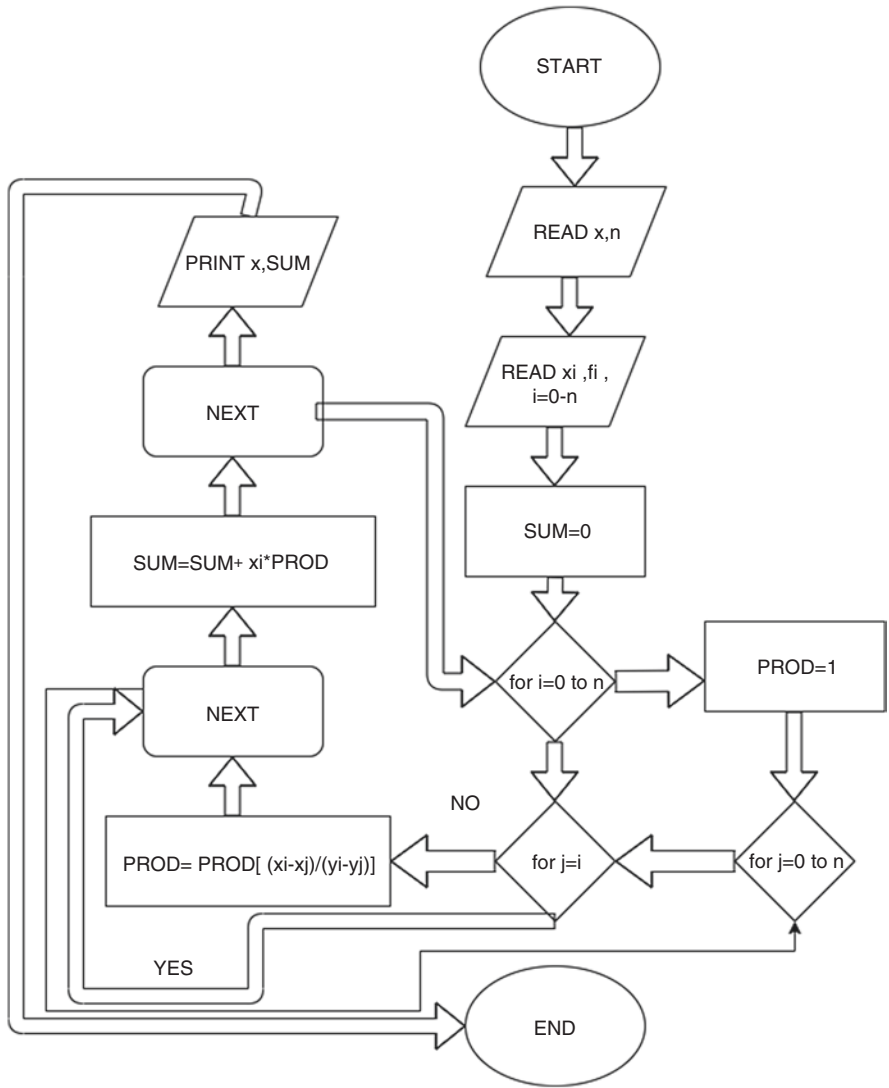
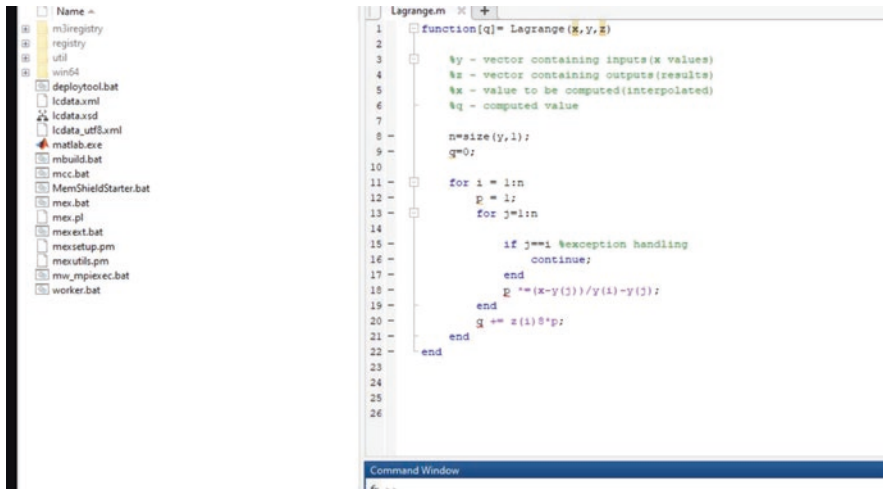


Fig. 3.7 Flowchart of Lagrange numerical



```

1  function[q]= Lagrange(x,y,z)
2
3  %y - vector containing inputs(x values)
4  %z - vector containing outputs(results)
5  %x - value to be computed(interpolated)
6  %q - computed value
7
8  n=size(y,1);
9  g=0;
10
11  for i = 1:n
12      p = 1;
13      for j=1:n
14
15          if j==i %exception handling
16              continue;
17          end
18          p **=(x-y(j))/(y(i)-y(j));
19      end
20      g += z(i)*p;
21  end
22  end
23
24
25
26

```

Fig. 3.8 Code for Lagrange

3.5 Conclusion

Ultrasound is one of the most significant factors in the field of biomedical engineering. Various upcoming technologies developing in this interdisciplinary field encompass the application of ultrasound. One of the major reasons why till date it has not gained much popularity in developing countries like India is only because of its high cost. Bringing down the cost to an affordable rate, in such every diagnostic center can provide ultrasound facilities even to people living in rural and suburban areas, was the prime motto. Electromagnetic loud speakers showed that the ability to transmit ultrasound frequencies is a novel approach for production of medical ultrasound.

3.6 Future Scope

We are constantly trying to build a closed loop unit, which does accurate ultrasound physiotherapy after processing the EMG signals in frequency domain. It gives out ultrasound waves for physiotherapy accordingly, accurately, and automatically. The whole technology is programmed and is much affordable and accurate than conventional systems due to decrease in overall circuit cost.

Acknowledgments We would like to acknowledge the Head of the Department of Biomedical Engineering, Netaji Subhash Engineering College, (Prof.) Dr. Sukumar Roy, and Dr. Piyali Basak, School of Bioscience and Engineering, Jadavpur University, for their constant encouragement and support, making this project a successful one.

References

1. Wells PN (2006) Ultrasound imaging. *Phys Med Biol* 51:R83
2. Greenslade TR Jr (1994) Experiments with ultrasonic transducers. *Phys Teach* 32:392–398
3. Kossoff G (2000) Basic physics and imaging characteristics of ultrasound. *World J Surg* 24:134–142
4. Kremkau FW (1994) Diagnostic ultrasound: principles and instruments. *Ultrasound Q* 12:65
5. Xiong SF, Yin ZL, Yuan ZF, Yan WB, Yang WY, Liu JJ, Zhang F (2012) Dual-frequency (20/40 kHz) ultrasonic assisted photocatalysis for degradation of methylene blue effluent: synergistic effect and kinetic study. *Ultrason Sonochem* 19:756–761



Altered Profile of Regulatory T Cells and NKT Cells As Characteristic of Chikungunya-Associated Polyarthralgia

Nilotpal Banerjee, Bibhuti Saha, and Sumi Mukhopadhyay

Abstract

Chikungunya is an arboviral infection having huge disease burden throughout the tropics, including India. The chief manifestation of the febrile illness is the development of debilitating joint pain, which often leads to arthritis. Till date, very little is known about the disease pathophysiology, which is very important toward better patient management and development of therapeutics. This study aims to characterize different subpopulations of T cell in the peripheral blood of chikungunya patients which may give some idea about the immune homeostasis during acute infection. At a Medical research institute devoted to tropical diseases, 25 informed consented chikungunya IgM⁺ patients of different age groups were enrolled during April 2015 to March 2017. After clinical examination, lymphocyte count of peripheral blood was noted followed by three-color flow cytometry. Interestingly, there is no significant ($P = 0.0583$) change in CD3⁺ T cell population, but there is statistically significant increase in CD3⁺ CD56⁺ ($P = 0.0003$) population among chikungunya patients with/without polyarthralgia and healthy controls. CD3⁺ CD4⁺ CD25⁺ (T_{regs}) are decreased significantly ($P < 0.0001$) in chikungunya patients with polyarthralgia. CD4:CD8 is also altered significantly in chikungunya patients. From this study, it is concluded that an imbalance in T_{reg} and NKT cell population is a characteristic of Chikungunya-associated polyarthralgia having possible immunopathological roles.

Keywords

Chikungunya · Polyarthralgia · Regulatory T cell · NKT cell

N. Banerjee · S. Mukhopadhyay (✉)
Department of Laboratory Medicine, School of Tropical Medicine,
Kolkata, West Bengal, India

B. Saha
Department of Tropical Medicine, School of Tropical Medicine, Kolkata, West Bengal, India

4.1 Introduction

Chikungunya (CHIK) is a single-stranded RNA virus of genus *Alphavirus* of family *Togaviridae*. This is an arbovirus transmitted by *Aedes* mosquito [2]. CHIK infection in humans is mostly characterized by short-duration fever and rash along with varied levels of joint pain. Most of the clinical symptoms of CHIK viral infection last for maximum 7–10 days on an average, but the joint pain can persist for 1 year causing extreme distress to the patient along with effective man-hour loss toward the economy [4]. Currently, CHIK viral infection is not only the issue of tropical countries only. In recent years, CHIK has a huge global burden affecting millions of people [11, 12]. The interplay between virus and host is believed to be possible cause of joint inflammation due to chikungunya. Recent studies in mouse model have indicated the involvement of CHIK virus-specific CD4⁺ but not CD8⁺ T cells as essentials for the development of joint swelling. Further, the role of Tregs has also been demonstrated in CHIK virus pathogenesis in mice model [8]. Taken together, T cell immunology plays a significant role in CHIK-associated arthritis.

T lymphocytes are innate immune cells having pivotal role in cell-mediated immunity in viral infections. CD3 is the signature marker of T lymphocytes, and estimation of CD3⁺ population in peripheral blood is a routine method in viral infections like HIV [1]. CD3⁺ cells are usually further characterized by immunophenotyping with anti-human CD4 and CD8 monoclonal antibodies. NKT cells are CD3⁺ CD56⁺ cell population which functionally differs from other CD3⁺ cells having both the properties of T lymphocytes and natural killer cells. CD3⁺ CD4⁺ CD25⁺ cells are popularly known as regulatory T cells which play crucial role in inflammatory and autoimmune diseases. Regulatory T cells are also known as suppressor T cells and are known to maintain the self-nonsel balance of the immune system by cascading signaling pathways to suppress other immune cells. T_{reg} balance is necessary for the homeostasis of the overall immune system, and any alteration in their frequency leads to destruction of normal healthy cells. The CD4:CD8 ratio in peripheral blood represents the tendency of the immune system toward development of inflammation [9]. These parameters are very important to determine the status of the disease manifestation at any given point of time. NKT cells are known to regulate immune response along with secretion of inflammatory cytokines upon activation by Ig-like lectins expressed by macrophages. So, the status of both NKT cells and T_{regs} is important to know the pathophysiology of joint inflammation and pain due to chikungunya infection. To the best of our knowledge, there is no such report regarding the status of those cells in chikungunya infection involving human subjects. In this background, this study aims to identify NKT cells and regulatory T cells in peripheral blood of chikungunya patients suffering from varied levels of joint pain along with healthy individuals by immunophenotyping which might give an explanation for Chikungunya-associated polyarthralgia.

4.2 Materials, Methods, and Subjects

Ethical permission for this study was given by the institutional ethical committee. This study has been done from April 2015 to March 2017, and 25 informed, written-consented patients along with 25 age- and sex-matched healthy donors were enrolled. After clinical evaluation of the patients, initial screening for the presence of IgM antibodies for arboviral infection was done by using WHO-recommended MAC ELISA kits provided by NIV, Pune, ICMR, Government of India. Dengue and chikungunya equivocal cases were repeated to confirm their status. After confirming disease status, peripheral blood was taken, and lymphocyte count was done by Sysmex KX-21 N™ Automated Hematology Analyzer. Furthermore, 100 μ L of whole peripheral blood was taken in a BD Falcon™ 5 ml round-bottom tube (obtained from BD Biosciences, India Pvt. Ltd.), and surface was stained with 5 μ L of PE/Cy5-conjugated anti-human CD3 mAb (Clone HIT3a) and FITC-conjugated anti-human CD56 mAb (HCD56) obtained from Biolegend®, San Diego, USA. For the immunophenotyping of T_{regs}, whole peripheral blood was mixed with PE/Cy5-conjugated anti-human CD3 mAb, FITC-conjugated anti-human CD4 (clone OKT4) or CD8 (clone SK1), and PE-conjugated anti-human CD25 (clone BC96) mAbs. After 30 min incubation with mAbs, the samples were treated with 2 mL of 1X BD Pharm Lyse™ buffer. The samples were processed as directed in the technical data sheet and undergone flow cytometric analysis through a BD FACSCalibur™ machine. The data generated through flow cytometer were further analyzed by BD CellQuest™ Pro Analysis software. Data was generated in duplicate, and further statistical analysis was done by using Graph Pad Prism 5 software.

4.3 Results

After initial clinical study, CHIK patients were divided into two groups, namely, chikungunya patients with and without polyarthralgia. According to a previous study by Gerardin P et al. (2009), subjects having joint pain involving more than six locations were treated as CHIK patients with polyarthralgia [7]. A total of 80% of CHIK patients were found to have polyarthralgia. Rest of the patients have joint pain in less than six locations. Total lymphocyte count in peripheral blood was found to be overall statistically significant but not significant among groups. This pathological parameter is patient specific but not disease specific. CD4 and CD8 ratio has been found to be increased significantly. NKT cells were found to have increased 2.53-fold in CHIK patients with polyarthralgia than healthy controls. Regulatory T cells are 8.73-fold decreased in CHIK patients suffering with polyarthralgia and 1.29-fold decreased in CHIK patients without polyarthralgia (Table 4.1, Fig. 4.1). This is found to be significant after statistical analysis.

Table 4.1 Different study parameters of the subjects

	Healthy controls ^a (N = 25)	CHIK patients without polyarthralgia ^a (N = 05)	CHIK patients with polyarthralgia ^a (N = 20)	P value* (one-way ANOVA)
Lymphocyte count	30 ± 10.58	32 ± 7.58	34.21 ± 4.68	0.0024
% of CD3 ⁺ cells (among lymphocytes)	58.55 ± 1.23	62.15 ± 1.06	62.32 ± 1.13	0.0583
CD 4: CD8	1.51 ± 0.15	1.8 ± 0.10	2.1 ± 0.23	0.0206
% of CD3 ⁺ CD56 ⁺ cells (among lymphocytes)	4.37 ± 1.05	6.9 ± 3.62	11.07 ± 2.60	0.0003
% of CD3 ⁺ CD4 ⁺ CD 25 ⁺ cells (among lymphocytes)	23.75 ± 2.86	18.31 ± 4.61	2.72 ± 5.31	<0.0001

^aMean ± S.E.M

*P < 0.05 is significant

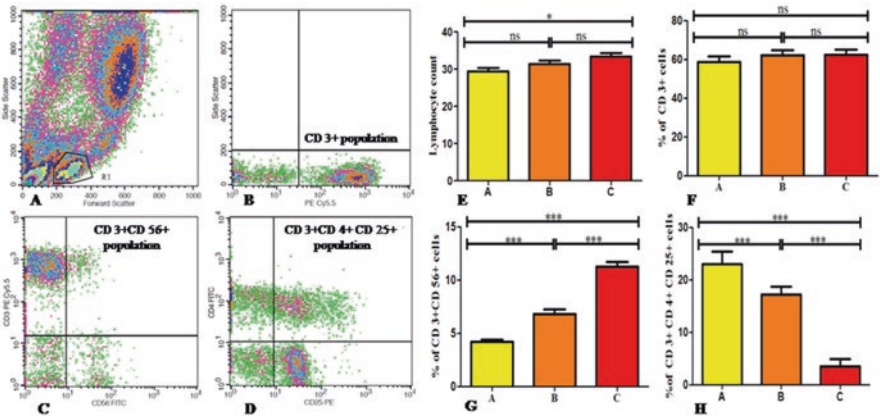


Fig. 4.1 (a–d) are representative intensity plots. (a) is the Forward vs. Side Scatter of white blood cells. (b) describes CD3 positive population. (c) shows CD3⁺ CD56⁺ cells. (d) represents CD3⁺ CD4⁺ CD25⁺ regulatory T cells. (e–h) are graphical representation of study parameters among three groups. (a) is healthy control, (b) is chikungunya patients without polyarthralgia, (c) is chikungunya patients with polyarthralgia within the graphs. One-way ANOVA was done among three groups. Between two groups, *t-test* was done for determination of significance. *P* < 0.05 is statistically significant. Nonsignificance is represented as “ns.” (e) is the total lymphocyte count among all the study groups. (f, g, h) are percentage of CD3⁺ cells, NKT cells, and regulatory T cells among all the study groups, respectively

4.4 Discussion

Lymphocyte count of patients in comparison with healthy individuals is not sufficient enough to comment on their immunological role in the pathophysiology of CHIK infection. Rather there is clonal expansion of different subpopulations of lymphocytes observed during CHIK infection which is not reflected by routine pathological test. Interestingly, CD3⁺ T lymphocytes were also not significantly changed in CHIK patients. Frequency of overall T cell population is not sufficient to comment on the cell-mediated immunity, which happens during viral infection like CHIK. Rather it becomes necessary to know the status of different subpopulations of T cells by immunophenotyping.

CD4 and CD25 positive regulatory T cells were found to be significantly decreased in study group, namely, chikungunya patients having arthralgia in more than six locations, whereas in CHIK patients who do not have developed polyarthralgia, they are not decreased significantly. So, it is clear that decrease of T_{regs} or suppressor T cells is observed in patients with polyarthralgia. CD4:CD8 ratio is also changed significantly. Interestingly, overall percentage of CD4 cells is increased, but that of regulatory T cells is decreased [Table 4.1]. This change indicated autoimmunity, which can destroy the host's own cells. The imbalance of Tregs which happens in some patients might lead to polyarthralgia. As from studies involving other diseases, it is clear that regulatory T cells have protective role against self-cell destruction [6]. Any deviation from the normal level of those cells possibly leads to destruction of host cells, which might be the cause of joint inflammation and pain in a significantly large subpopulation of persons suffering from CHIK infection.

On the other hand, NKT cells are found to be significantly increased in those patients having polyarthralgia. In response of the infection, NKT cells are expanded in some patients to produce inflammatory cytokines [10]. From previous studies, it is known that NKT cells involve with Ig-like lectins, which are responsible for inflammation in diseases like systemic sclerosis and systemic lupus erythematosus [3, 5]. Surge of such cells gives an idea about the inflammation process during CHIK infection. Those patients, who have an increased NKT cell frequency, suffer with more joint inflammation.

So from this study, it is clear that though there is no significant change in CD3⁺ population among CHIK patients, there is expansion of subpopulations, which is not reflected by overall percentage of T lymphocytes. Detailed study revealed altered percentage of Tregs along with NKT cells, which possibly leads to development of polyarthralgia. This information becomes very helpful for further study toward development of therapeutics and more detailed study of the CHIK disease pathophysiology.

4.5 Conclusion

NKT cells are increased in CHIK patients and might have an important role in the development of joint inflammation. Regulatory T cells are decreased in CHIK patients with polyarthralgia. Alteration of normal level of those cells is a potential cause of self-cell destruction, and possibly this is the cause behind debilitating joint pain. For the first time, this study reports about NKT cells, T_{regs}, and CD4:CD8 data, which are the characteristics of chikungunya-associated polyarthralgia.

Acknowledgments Nilotpal Banerjee is a recipient of Research Fellowship from Department of Biotechnology, Government of West Bengal (File No. 232/BT(Estt)/RD-24/2014). This scientific study is funded by Department of Biotechnology, Government of West Bengal (File No.: WDBBT Memo No. 232/BT(Estt)/RD-24/2014) India. We are thankful to Prof. (Dr.) Mitali Chatterjee, Dept. of Pharmacology, IPGME&R, Kolkata, India, for giving access to flow cytometry facility available in her laboratory.

References

1. Autran B, Carcelain G, Li TS, Blanc C, Mathez D, Tubiana R, Katlama C, Debre P, Leibowitch J (1997) Positive effects of combined antiretroviral therapy on CD4+ T cell homeostasis and function in advanced HIV disease. *Science* 277(5322):112–116
2. Banerjee N, Mukhopadhyay S (2016) Viral glycoproteins: biological role and application in diagnosis. *Virus Dis* 27(1):1–11
3. Chen J, Wu M, Wang J, Li X (2015) Immunoregulation of NKT cells in systemic lupus erythematosus. *J Immunol Res* 2015
4. Collinder Avia. Chik-V seen as costing billions in lost productivity. <http://jamaica-gleaner.com/gleaner/20141015/business/business2.html>. Accessed on 9 May 2017
5. Cossu M, van Bon L, Nierkens S, Santaniello A, Beretta L, Radstake T (2014) Nk/nkt cells from early and definite systemic sclerosis patients show different immunological responses after Il-2 stimulation. *Arthritis Rheumatol* 66:S528–S529
6. Francisconi CF, Vieira AE, Bigueti CC, Glowacki AJ, Trombone APF, Letra A, Silva RM, Sfeir CS, Little SR, Garlet GP (2016) Characterization of the protective role of regulatory T cells in experimental periapical lesion development and their chemoattraction manipulation as a therapeutic tool. *J Endod* 42(1):120–126
7. Gérardin P, Fianu A, Michault A, Mussard C, Boussaïd K, Rollot O, Grivard P, Kassab S, Bouquillard E, Borgherini G, Gaüzère BA (2013) Predictors of Chikungunya rheumatism: a prognostic survey ancillary to the TELECHIK cohort study. *Arthritis Res Ther* 15(1):R9
8. Lee WW, Teo TH, Her Z, Lum FM, Kam YW, Haase D, Rénia L, Röttschke O, Ng LF (2015) Expanding regulatory T cells alleviates chikungunya virus-induced pathology in mice. *J Virol* 89(15):7893–7904
9. Lu W, Mehraj V, Vyboh K, Cao W, Li T, Routy JP (2015) CD4: CD8 ratio as a frontier marker for clinical outcome, immune dysfunction and viral reservoir size in virologically suppressed HIV-positive patients. *J Int AIDS Soc* 18(1)
10. Vivier E, Tomasello E, Baratin M, Walzer T, Ugolini S (2008) Functions of natural killer cells. *Nat Immunol* 9(5):503–510
11. WHO. Chikungunya, Chikungunya: WHO fact sheet on Chikungunya providing key facts and information on scope of the problem, who is at risk, prevention, WHO response. <http://www.who.int/mediacentre/factsheets/fs327/en/>. Accessed on 9 May 2017
12. WHO. Surveillance and outbreak alert, Chikungunya. http://www.searo.who.int/entity/emerging_diseases/topics/Chikungunya/en/. Accessed on 9 May 2017



Cytotoxicity and Apoptosis of Human Colon Carcinoma Cell Line (HT29 Cells), Treated with Methanolic Extract of *Chlorococcum humicola*

Uma Ramaswamy, Sivasubramanian Velusamy, and Niranjali S Devaraj

Abstract

Chlorococcum humicola, green microalga, possess higher concentration of bio-active compounds, which includes quercetin, sterol, terpenes, fatty acids and carotenoid showing antimutagenic, antimicrobial, anti-tumour and chemopreventive effects. However, the precise mechanism of anticancer activity of *C. humicola* remains to be elucidated. The HT29 human colon carcinoma cell line was used to evaluate the cytotoxic effect of aqueous and methanolic extracts of *Chlorococcum humicola* by MTT assay. The MTT assay demonstrated that aqueous (AECH) and methanolic extract (MECH) of *C. humicola* inhibited the growth of HT29 cell line with IC₅₀ value of 50 and 15.62 µg/ml, respectively. Hence, to find out the mechanism of apoptosis in MECH, western blotting was carried out. Western blot analysis was done to examine the protein expression of Bcl-2 (anti-apoptotic), p53 (tumour suppressor), PARP and Bax (pro-apoptotic) in MECH-treated HT29 cells. MECH modulated Bcl2/Bax ratio and upregulated p53, and PARP caused apoptosis in HT29 cells confirmed by immune blotting results. Once activated, caspase-3 cleaves the 116 kDa, death substrate PARP into 85 kDa fragment. The western blotting results suggested that MECH inhibits the growth of HT29 colon cancer cell lines through mitochondrial (intrinsic) and receptor (extrinsic) mediated apoptosis, which may in part explain its anticancer activity.

U. Ramaswamy (✉)

PG & Research Department of Biochemistry, Dwaraka Doss Goverdhan Doss Vaishnav College, Chennai, Tamil Nadu, India

S. Velusamy

Phycospectrum environmental research centre, Anna nagar, Chennai, Tamil Nadu, India

N. S. Devaraj

Department of Biochemistry, University of Madras, Guindy, Chennai, Tamil Nadu, India

KeywordsApoptosis · HT29 cells · *Chlorococcum humicola* · MTT assay

5.1 Introduction

Cancer is one of the life-threatening diseases and characterized by the deregulated proliferation of abnormal cells. Cancer death from worldwide is projected to increase in the future. Most of the anticancer drugs used in chemotherapy are cytotoxic to normal cells and cause side effects. Therefore, research for finding new anticancer compounds from natural source with minimal side effects and cheaper cost has been focused on [1]. Microalgae were rich in biologically and pharmacologically active compounds, which includes amino acids, vitamins, minerals, fatty acids, enzymes, glycolipids and sulphated compounds. Recent findings evidenced that microalgae contained antiviral, antibacterial, antifungal [2] and anti-tumour [3] activities. *Chlorococcum humicola*, green microalgae, exhibited anticancer activity against Hep2 cell line, human lung carcinoma [4]. Apoptosis can be caused by both intrinsic and extrinsic signals which lead to the activation of cysteine-dependent aspartate-directed proteases (caspases) and nucleases resulting in destruction of the cell. The present study was carried out to find the molecular mechanism of MECH-induced cytotoxicity and apoptosis in human colon cancer cells.

5.2 Materials and Methods

5.2.1 Outdoor Cultivation of Algae

Chlorococcum humicola culture was collected from the Vivekananda Institute of Algal Technology (VIAT) in Chennai. Five hundred ml of algal cultures was added to 20 litres of water containing 0.25 g/l of NPK fertilizer with a facility to pump the culture with aeration pump. The algae was grown for 2 weeks and harvested.

5.2.2 Preparation of Algal Extracts

10 g of dried coarse powder of the green microalga of *Chlorococcum humicola* was extracted with 50 ml of methanol and water, respectively, and kept in an orbital shaker for 48 h at 28 °C for 100 rpm. The extracts were filtered through Whatman no.1 filter paper, and the filtrate was evaporated in vacuum at 45 °C and then lyophilized [5]. The extracts obtained were dissolved in dimethyl sulphoxide (DMSO) and used for the study.

5.2.3 Cell Line and Culture

Human colon cancer HT29 and vero cell lines were obtained from National Centre for Cell Science (NCCS), Pune, India. The cells were maintained in RPMI-1640; supplemented with 10% FBS, penicillin (100 U/ml) and streptomycin (100 µg/ml) and incubated at 37 °C in a humidified incubator of 50 µg/ml CO₂.

5.2.4 In Vitro Assay for Cytotoxicity Activity (MTT Assay)

The cytotoxicity of samples on HT29 cells was determined by MTT assay [6]. Cells (1×10^5 /well) were added in a 100 µl of medium/well in 96-well plates and incubated for 48 h. Various concentrations of the samples (AECH & MECH in 0.1% DMSO) were added to the cells and incubated for 48 h at 37 °C. After removal of the sample solution and washing with phosphate buffered saline (pH 7.4), 20 µl/well (5 mg/ml) of 0.5% 3-(4, 5- dimethyl-2-thiazoly)-2,5-diphenyl-tetrazolium bromide (MTT) was added to each well. After 4 h of incubation 0.04M HCl/Isopropanol was added and purple-coloured formazan was formed, and the absorbance values were read at 570 nm. All experiments were performed in triplicates. The effect of the samples on the proliferation of human colorectal cancer cells was expressed as the % cell viability, using the following formula:

$$\text{Cell viability\%} = \text{OD of treated cells/OD of control cells} \times 100.$$

5.2.5 Western Blot Analysis

1×10^5 H29 cells were seeded into 6-well plates and treated with various IC₅₀ concentrations of MECH for 48 h. Cells were collected by trypsinization and washed three times with phosphate-buffered saline (PBS) lysed in cell lysis buffer. 10 µg of extracted protein samples in a lane was added in five times the volume of sample buffer (50 mM Tris-HCl, pH 6.8, 12.5% glycerol, 1% sodium dodecyl sulphate, 0.01% bromophenol blue) and subjected to denaturation at 100 °C for 5 min and then electrophoresed on sodium dodecyl sulphate-poly acrylamide gel electrophoresis (SDS-PAGE) at 200 V for 45 min, followed by quantitative transfer and irreversible binding to nitrocellulose membrane. Then, the membrane was washed with buffer and incubated with primary antibody, overnight at 4 °C. The membrane was washed again with washing buffer and incubated with horseradish peroxidase (HRP)-conjugated secondary antibody for 2 h at room temperature. The membrane was washed, and diaminobenzidine solution was added and incubated at room temperature for colour development, which was usually completed within 5–10 min. β actin was used as internal control. Intensity of bands was digitized by gel scanner, and the densitometry analysis was done using UN-SCAN-IT gel software (Version 6.1).

5.3 Results and Discussions

5.3.1 Evaluation of In Vitro Cytotoxicity of the Algal Extracts Against HT29 Cells

As shown in Fig. 5.2, treatment of HT 29 cells with 0.976–1000 $\mu\text{g/ml}$ of MECH for 24 h reduced cell viability by 8.5–87.2% in a dose-dependent manner. The decrease in cell viability was constant, and the 50% cell viability occurred at the concentration of 15.625 $\mu\text{g/ml}$ and 50 $\mu\text{g/ml}$, respectively, for MECH and AECH against HT29 cells. The IC_{50} value for AECH and MECH against vero cell line was 92 and 125 $\mu\text{g/ml}$, respectively (Fig. 5.1). These data demonstrated that MECH inhibits the growth of HT29 cells effectively when compared to the AECH. Previous studies concluded that the marine macroalgae belonging to Phaeophyta group possess anti-tumour activity and sterols from *Sargassum carpophyllum* exhibited cytotoxicity against several cultured cell lines [7] (Fig. 5.2).

HT29 cells were treated for 48 h with indicated concentration of MECH. Lane 1: Control cells (HT 29); Lane 2, 3.95 $\mu\text{g/ml}$; Lane 3, 7.812 $\mu\text{g/ml}$; Lane 4, 15.62 $\mu\text{g/ml}$ (IC_{50}) concentration of MECH-treated HT29 cells. β - actin was used as internal control. Values are expressed as mean \pm SD

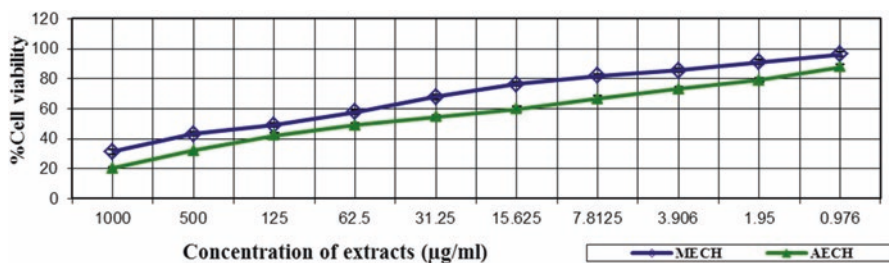


Fig. 5.1 In vitro cytotoxicity of methanol and aqueous extracts of *Chlorococcum humicola* on vero cell line

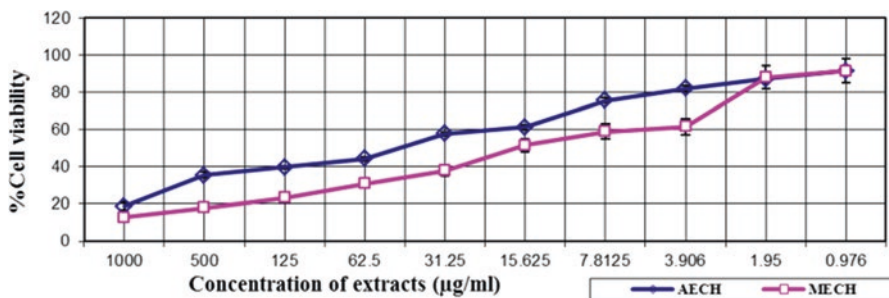


Fig. 5.2 In vitro cytotoxicity of methanol and aqueous extracts of *Chlorococcum humicola* on HT29 cells

5.3.2 Effect of Methanolic Extract of *C. humicola* on Apoptosis of HT29 Cells

The western blot results of pro-apoptotic protein Bax, tumour suppressor protein p53, anti-apoptotic protein Bcl-2 and PARP for the HT29 cells treated with 0, 3.90, 7.82 and 15.625 $\mu\text{g/ml}$ of MECH was shown in Fig. 5.3. Tumour suppressor protein (p53) level was reduced in control but after treatment with MECH, showed increased levels of p53 expression in treated cells, which in turn transcriptionally activates the Bax and Fas genes in response to apoptosis. On activation, caspase-3 cleaves the 116 kDa death substrate poly(ADP-ribose) polymerase (PARP) into 85 kDa

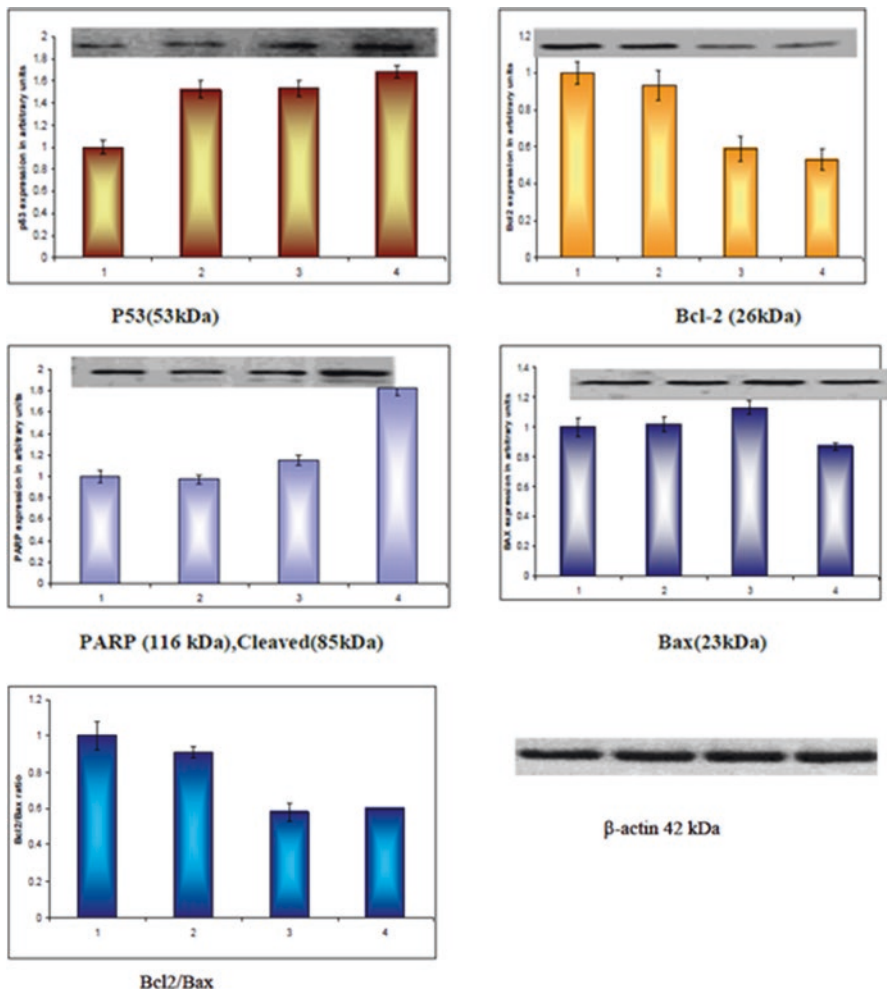


Fig. 5.3 Analysis of expression of apoptotic proteins by Western blotting (a) Effect of MECH on the expression of apoptotic proteins in HT29 cells (densitometry analysis)

fragment. Western blot analysis showed that caspase-3 activation preceded PARP signature-type cleavage. Western blot analysis demonstrated that MECH treatment with HT29 cells increased Bax and profoundly reduced Bcl-2 protein expression and the Bcl 2/Bax ratio in HT29 cells. Results suggested that MECH induced mitochondrion-dependent apoptosis in HT29 cells through the regulation of expression of Bcl-2 family protein. *Spica prunellae* inhibits the growth of HT29 colon cancer cells through mitochondrion-mediated apoptosis [8].

5.4 Conclusion

In the present study, results for the first time demonstrated, the methanolic extract of *Chlorococcum humicola* inhibits tumour growth and reduced cell viability and induces apoptosis in mitochondrion and receptor dependent pathway in the colorectal cancer-derived cell line HT29. These results suggest that *Chlorococcum humicola* may be a potential novel therapeutic agent and holds great promise to explore the isolation and characterization of lead compounds liable for anticancer activity.

References

1. Xu N, Fan X, Yan X, Tseng C (2004) Screening of marine algae from China for their antitumor activities. *J Appl Phycol* 16:451–456
2. Ozdemir G, Karabay NU, Dalay CM, Pazarbasi B (2004) Antibacterial activity of volatile component and various extracts of *Spirulina platensis*. *Phytother Res* 18:754–757
3. Hoa LTP, Quang DN, Ha NTH, Tri NH (2011) Isolating and screening mangrove microalgae for anticancer activity. *Res J Phytochem* 5:156–162
4. Uma R, Sivasubramanian V, Niranjali Devaraj S (2011) Evaluation of in vitro antioxidant activities and antiproliferative activity of green micro algae of *Desmococcus olivaceus* and *Chlorococcum humicola*. *J Algal Biomass Util* 2(3):82–93
5. Olukayo DK, Idika N, Odugbemi T (1993) Antimicrobial activity of some medicinal plants from Nigeria. *J Ethnopharmacol* 39:69–72
6. Mossman T (1983) Rapid colorimetric assay for cellular growth and survival: application to proliferation and cytotoxicity assays. *J Immunol Methods* 65(1–2):55–63
7. Tang HF, Yang-Hua Y, Yao XS, Xu QZ, Zhang XY et al (2002) Bioactive steroids from the brown alga *Sargassum carpophyllum*. *J Asian Nat Prod Res* 4:95–105
8. Zheng L, Chen Y, Lin W, Zhuang Q, Chen X, Wei X, Liu X, Peng J, Thomas J, Sferra TJ (2011) *Spica prunellae* extract promotes mitochondrion dependent apoptosis in human colon carcinoma cell line. *Afr J Pharm Pharmacol* 5(3):327–335



Universal Primer Design for the Detection of Diverged CTX-M Extended-Spectrum β -Lactamases (ESBL) That Give Penicillin and Cephalosporin Resistance During Superbug Infections

Asit Kumar Chakraborty, Kousik Poria, and Sourav Kumar Nandi

Abstract

The complexity of diverged β -lactamases in multidrug-resistant bacteria has created a panic as common antibiotics failed to cure infections. We found >40%, >25%, and 0.002% of bacteria in Kolkata water bodies (river, sea, rain) were ampicillin, tetracycline, and meropenem resistant, respectively. More than 20 unique sequence classes of β -lactamases were known to cause MDR inactivating penicillin, cephalosporin, and carbapenem drugs. Further, there are other diverged *mdr* genes such as drug efflux genes (*acrAB*, *mexAB-EF*, *tetA*), drug-modifying genes (*aacA1/CI*, *strA/B*), and drug-binding genes (*tetS/M*, *PBP*, *sulI*) that were present in a single bacterial plasmid suggesting too many PCR reactions to be performed to understand the drug resistomes. Thus, we devised a method of reduction in PCR assays using seq-2 and forced multi-align analysis of >200 bla_{CTX-M} protein sequences for universal primer design. The universal primer set recognized major type-1, type-2, and type-9 bla_{CTX-M} mutants including clinically relevant bla_{CTX-M-15}. We also made bla_{TEM}-SHV common primers. This study was supported by the WHO recommendations to adopt a uniform policy for AMR detection and antibiotic therapy worldwide. Interestingly, we have also devised a solution (MDR-Cure) for the treatment of plasmid-borne MDR infections using Indian phytoextracts.

A. K. Chakraborty (✉) · K. Poria · S. K. Nandi
Post Graduate Department of Biotechnology and Biochemistry, Genetic Engineering Laboratory, Oriental Institute of Science & Technology (OIST), Vidyasagar University, Midnapore, West Bengal, India

Keywords

AMR · Universal primers · CTX-M β -lactamases · PCR diagnosis · MDR plasmids · ESBL · Cefotaxime resistant

6.1 Introduction

β -Lactamases are enzymes that are highly expressed in multidrug-resistant bacteria and hydrolyze penicillin, cephalosporin, and carbapenem drugs [1]. Presently, ampicillin, cefotaxime, and imipenem drugs are not sufficient to cure bacterial infections as β -lactamase genes such as KPC-2, OXA-23/48/58, and NDM-1 were assembled into conjugative plasmids of bacteria providing high expression profiles and resistance to all β -lactams and β -lactamase inhibitors [2]. Different classes of enzymes hydrolyze the β -lactams with different substrate specificities. For example, TEM-1 enzyme only hydrolyzes benzyl penicillin but not oxacillin or ceftriaxone, OXA-1 enzyme hydrolyzes oxacillin easily than penicillin but could not hydrolyze cefotaxime and sulbactam, and CTX-M enzymes hydrolyze cefotaxime easily but not meropenem. On the other hand, KPC-2 could hydrolyze cefotaxime and doripenem both as do OXA-23 and OXA-48. Most recently discovered NDM-1 could hydrolyze most carbapenems, penicillins, and cephalosporins as well including most β -lactamase inhibitors but not avibactam [3]. A *Nature* journal wrote, “last resort imipenem drug got resistance,” explaining all humans are now susceptible to NDM-1MDR pathogens [4]. *Mcr-1 mdr* gene discovery foils colistin (polymyxin E) drug for therapeutic use [5]. The situation is so frustrating that 700,000 deaths (200,000 neonates) in the recent year were reported by the WHO and 20 million deaths will be happening as we approach 2050. So medical authorities have declared war against AMR by infusing huge funding to monitor MDR bacterial population worldwide. Sadly, expression of other *bla* genes (OXA, TEM, CTX-M), very diverged drug-modifying genes (*aac*, *aph*, *aad*, *arr*), and drug efflux genes (*acr*, *mex*, *emr*, *tet*, *nor*, *mac*) in these microorganisms was maintained in high-expression conjugative plasmids, making the AMR trauma more serious, where conjugative *E. coli*, *K. pneumoniae*, and *S. enterica* were serious threats as they could transfer the *mdr* genes to most waterborne bacteria by conjugation [6]. It is accepted worldwide that all patients should be analyzed for AMR status if they do not respond to common drugs including β -lactamase inhibitor combination. There are 12 well-known Bla enzymes reported [7], TEM (286aa), SHV (286aa), CTX-M (291aa), KPC (293aa), AmpC (382aa), OXA-1 (276aa), OXA-23 (273aa), IMP (246aa), VIM (266aa), OXA-48 (265aa), OXA-58 (280aa), CMY (381aa), and NDM-1 (270aa), and other less familiar enzymes such as SPM (276aa), LAT (381aa), FOX (382aa), L1 (303aa), MIR (381aa), IMI (292aa), TOHO (291aa), DHA (379aa), TMB (245aa), etc. We speculate that many β -lactamases (TEM, SHV) could be analyzed by one set of primer having sequence similarity to amp gene of plasmid pBR322 [8]. However, CTX-M isomers have a very diverged NH₂ terminal and need six sets of primers for more than three independent lineages (CTX-M-1 type, CTX-M-2

type, and CTX-M-9 type) unless universal homology could be found [9]. The easy and quick assay of the *mdr* genes is the PCR analysis of plasmid and genomic DNA of bacteria isolated from blood, stool and urine of patients. But too many PCR reactions for one patient are very expensive for poor patients in India, Malaysia, Iran, Nepal, and the Philippines and also most of the African and Latin American countries. The truth is, penicillin is the safest drug used in clinical therapy as it inhibits peptidoglycan cross-linking in the cell wall, which is absent in humans and animals.

*Bla*_{CTX-M} genes are originated from chromosomal locus of various *Kluyvera* species and have been facilitated by mobile genetic elements such as ISEcp1 or ISCR1 [10]. Multi-replicon FII plasmids carry the most widely distributed *bla*_{CTX-M-15} across continents, paving the way for *bla*_{CTX-M-15} into different genetic lineages of *Escherichia coli*, *Salmonella enterica*, *Pseudomonas aeruginosa*, *Proteus mirabilis*, and *Klebsiella pneumoniae* [11, 12]. Molecular characterization of *bla*_{CTX-M} isomers and others will be adapted in most countries soon, and thus reduction in PCR assays is important for poor nations [13]. CTX-M β-lactamases have been recently divided into five groups based on their amino acid sequence identities [14]. Group I includes CTX-M-1, CTX-M-3, CTX-M-10 to CTX-M-12, CTX-M-15, CTX-M-22, CTX-M-23, CTX-M-28, CTX-M-29, and CTX-M-30. Group II includes CTX-M-2, CTX-M-4 to CTX-M-7, and CTX-M-20 and Toho-1. Group III includes CTX-M-8. Group IV includes CTX-M-9, CTX-M-13, CTX-M-14, CTX-M-16 to CTX-M-19, CTX-M-21, and CTX-M-27 and Toho-2. Finally, group V includes CTX-M-25 and CTX-M-26. We have reasoned here such classification is incomplete as 189 variants have been discovered so far with common lineage from CTX-M-1, CTX-M-2, and CTX-M-9 and others are very minor groups. We have designed a universal primer set by forced multi-align method and have dramatically reduced the number of PCR reactions to understand the CTX-M contamination in clinical and environmental samples. CTX-M β-lactamases are very abundant in MDR plasmids. We have devised a method that such complex nature CTX-M enzymes could be selected by one set of universal primers saving time and cost. We argue that CTX-M-9 is an extremely divergent motif of type-II CTX-M variants, and similarly CTX-M-8 is a subgroup of CTX-M-1.

6.2 Materials and Methods

The CTX-M-1 and CTX-M-2 seq-2 alignment was performed using NCBI BLAST (www.ncbi.nlm.nih.gov). Such analysis was not complete and most 5'-sequences of type-1, type-2, and type-9 CTX-M genes were not aligned in this analysis having divergent. So initially from protein databases, CTX-M-1 vs CTX-M-3 and CTX-M-2 vs CTX-M-4 were aligned by seq-2 blast, and from the such data, cut and paste were done to align CTX-M-1 vs CTX-M-2 using Microsoft Word. Then, the matched identical two conserved protein sequences were found by looking contact two protein sequences and used to get a conserved universal protein sequence. The position of similar CTX-M-1 vs CTX-M-3 and CTX-M-2 vs CTX-M-4 DNA sequences was

performed to obtain the conserved sequence position by multiplying the protein homology position by three. The primers were analyzed by OligoAnalyzer 3.1 software. Each oligonucleotide was then checked by Nucleotide BLAST Search if any unwanted homology was present in the GenBank. Further, two sets of primer each specific for CTX-M-1 and CTX-M-2 lineages were done and used to recheck by BLAST analysis such as primer selected either class-1 or class-2 CTX-M enzymes. Further degeneracy on the primers was corrected by comparing the *bla*CTX-M-9 genes using plasmid as well as genome databases [3].

The PCR reaction (20 μ L) contained ~40 ng plasmid DNA, 10 pmole primers, 0.25 mM dXTPs, 1.5 mM MgCl₂, and 2 unit Taq DNA polymerase. The reaction cycle was as follows: 94 °C for 3 min for 1 cycle; 94 °C for 45 sec, 52 °C for 45 sec, and 72 °C for 2 min for 35 cycles; and followed by 72 °C for 5 min for 1 cycle and then set to 4 °C to stop. About 10 μ l of the PCR reaction was loaded onto 1% agarose gel containing 0.5 μ g/ml ethidium bromide, and the gel was run in 1xTAE buffer at 50 V for 3 h. The photograph was taken under UV illumination. Sanger color dideoxy sequencing was performed by the SciGenom Labs Pvt. Ltd., Kerala, India. DNA sequences were analyzed by BLAST and Seq-2 programs of NCBI. The primers are developed in the study as shown in Table 6.1.

Water from Ganga River was collected at 7 am on Monday from Babu Ghat and Howrah Station areas. About 100 μ l of water was spread onto 1.5% Luria Bertani Agar Plate containing different antibiotics. MDR bacteria were selected in agar plate containing ampicillin+ streptomycin+ chloramphenicol+ tetracycline or ciprofloxacin at 50, 50, 34, and 20 μ g/ml, respectively [3]. As imipenem- and meropenem-resistant bacteria were present low concentration in Ganga River water (0.2 cfu/ml water) and a modified method was followed. 2 ml of 5X LB medium was added into 10 ml Ganga River water, and imipenem was added at 2 μ g/ml and was incubated 24 h to get imipenem-resistant bacterial population. Antibiotics were purchased from HiMedia and stored at 20–50 mg/ml at –20 °C. Antibiotic papers were also purchased from HiMedia according to the CLSI standard. Antibiotic papers are as follows: AMP-30 μ g (ampicillin), Met-10 μ g (methicillin), AT-50 (aztreonam), COT-25 μ g (cotrimoxazole), CAZ-30 μ g (ceftazidime), LOM-15 μ g (lomefloxacin), VA-10 μ g (vancomycin), AK-10 μ g (amikacin), LZ-10 μ g (linezolid), TGC-15 μ g (tigecycline), and IMP-10 μ g (imipenem). The antibiotic solutions were made as follows: ampicillin 50 mg/ml in water, tetracycline 20 mg/ml in ethanol,

Table 6.1 Universal common primer sequences for *bla*_{CTX-M} and *bla*_{TEM-SHV}

Primer	Primers were developed and used in this study		
	Primer sequence	Length	Interpretation
ctxFIU-1-2	5'-AACACMGCMGATAATTCACA-3'	586 bp	M = A/C
ctxRIU-1-2	5'-CCGCATATCRTTGGTGGTG-3'		R = A/G
ctxF-1-2-9	5'-ATGTGAGYACCAGTAARGTRA-3'	654 bp	R = A/G
ctxR-1-2-9	5'-CCAACCGTTGGTGACGAT-3'		Y=C/T
Tem-shvFIU	5'-ATGATGAGCACYTTTAAAGT-3'	312 bp	Y=C/T
Tem-shvRIU	5'-TCATTGAGYTCCGKTTCCCA-3'		K = G/T

chloramphenicol 34 mg/ml in ethanol, ciprofloxacin 50 mg/ml in water, cefotaxime 25 mg/ml in water, and streptomycin 50 mg/ml in water.

The barks of *Suregada multiflora* (Ban-Naranga) and *Cassia fistula* (Bandhorlathi) were collected in July 2019 from the Midnapore district of West Bengal. Flower buds of *Syzygium aromaticum* (labanga spice) and barks of *Cinnamomum zeylanicum* (darchini) were purchased from grocery stores at Kolkata and Midnapore, respectively. Each 10 gm dried and grinded plant and spice parts (*Suregada multiflora*, *Cassia fistula*, *Syzygium aromaticum*, *Cinnamomum zeylanicum*) was suspended in 40 ml ethanol for overnight, and the extracts were concentrated 5–10 times (we called MDR-Cure, if all phytoextracts were mixed) and 50 μ l is used for Kirby-Bauer agar hole assay. Thin-layer chromatography (TLC) was performed using methanol, water, and acetic acid (50:40:10) as the mobile phase for 1 h. Organic molecules were seen and recovered by UV shadowing and were eluted in ethanol from silica gel. Mass spectrometry (MS), nuclear magnetic resonance (NMR) spectrometry, and Fourier-transform infrared spectrometry (FTIR) are in progress to characterize active chemicals (Chakraborty 2017).

6.3 Result

Bla_{CTX-M-1} (accession no. AJM91204) and bla_{CTX-M-2} (accession no. AAV28216) were much diverged (60% similarity), and two sets of primers were necessary to know the AMR status. CTX-M-1 type had a similarity to CTX-M-3, CTX-M-10 to CTX-M-12, CTX-M-15, CTX-M-22, CTX-M-23, CTX-M-28 to CTX-M-30, CTX-M-32 to CTX-M-34, CTX-M-36, CTX-M-37, CTX-M-52 to CTX-M-55, CTX-M-57, CTX-M-58, CTX-M-60 to CTX-M-62, CTX-M-64, CTX-M-66, CTX-M-68 to CTX-M-72, CTX-M-77, CTX-M-79, CTX-M-80, CTX-M CTX-M-88, CTX-M-89, CTX-M-96, CTX-M-101, CTX-M-103, CTX-M-107 to CTX-M-109, CTX-M-114, CTX-M-116, CTX-M-117, CTX-M-132, CTX-M-136, CTX-M-138, CTX-M-139, CTX-M-142, CTX-M-150, CTX-M-155 to CTX-M-158, CTX-M-161 to CTX-M-164, CTX-M-166, CTX-M-167, CTX-M-169, CTX-M-170, CTX-M-172, CTX-M-173, CTX-M-175, CTX-M-176, and CTX-M-179 to CTX-M-184, CTX-M-197, CTX-M-202, CTX-M-206 to CTX-M-212, CTX-M-220, CTX-M-222 and CTX-M-230 to CTX-M-32 isolates. CTX-M-2 had a similarity to CTX-M-4 to CTX-M-7, CTX-M-20, CTX-M-21, CTX-M-26, CTX-M-31, CTX-M-35, CTX-M-43, CTX-M-56, CTX-M-59, CTX-M-74 to CTX-M-76, CTX-M-87, CTX-M-89, CTX-M-92, CTX-M-97, CTX-M-100, CTX-M-115, CTX-M-126, CTX-M-148, CTX-M-165, CTX-M-171, and CTX-M-178, CTX-M-200, CTX-M-205, CTX-M-217 and CTX-M-229 isolates (see Table 6.1 for the assignment of all isomers). CTX-M-9 has emerged as one major group of CTX-M and has a similarity to CTX-M-13, CTX-M-14, CTX-M-16, CTX-M-19, CTX-M-24, CTX-M-27, CTX-M-38, CTX-M-42, CTX-M-51, CTX-M-65, CTX-M-67, CTX-M-73, CTX-M-81, CTX-M-86, CTX-M-90, CTX-M-93, CTX-M-99, CTX-M-102, CTX-M-104 to CTX-M-106, CTX-M-110 to CTX-M-113, CTX-M-121, CTX-M-122, CTX-M-124, CTX-M-125, CTX-M-129, CTX-M-130, CTX-M-147,

CTX-M-1	1	MVKKSLRQFTLMATATVTL	LLG	SV	FLYAQTADV	VQ	QKLAELERQ	SGGRLG	VALINTADNSQ	60
		M+ +S+R+ L	AT+ LL	S L+AQ	VQQ+L	LE+ SGGRLG	VALINTADNSQ			
CTX-M-2	1	MMTQSI	RRSMLTVMATL	PLLF	SSATLHAQANSV	QQQL	EAL	EKSSGGRLG	VALINTADNSQ	60
CTX-M-1	1	MVKKSLRQFTLMATATVTL	LLG	SV	FLYAQTADV	VQ	QKLAELERQ	SGGRLG	VALINTADNSQ	60
		MV K +++	A A +	LLGS	FLYAQT+ VQQ	KL	LE+ SGGRLG	VALI+TADN+Q		
CTX-M-9	1	MVTKR	VRQRMF	AAAACI	PLLLG	SAPLYAQT	SAVQQ	KLAALEK	SSGGRLG	VALIDTADNTQ
CTX-M-2	1	MMTQSI	RRSMLTVMATL	PLLF	SSATLHAQANSV	QQQL	EAL	EKSSGGRLG	VALINTADNSQ	60
		M+T+ ++R	M A +PLL	SA L+AQ	++VQQ+L	ALEKSSGGRLG	VALI+TADN+Q			
CTX-M-9	1	MVTKR	VRQRMF	AAAACI	PLLLG	SAPLYAQT	SAVQQ	KLAALEK	SSGGRLG	VALIDTADNTQ
CTX-M-01	1	MVKKSLRQFTLMATATVTL	LLG	SV	FLYAQTADV	VQ	QKLAELERQ	SGGRLG	VALINTADNSQ	60
		MVKKSLRQFTLMATATVTL	LLG	SV	FLYAQTADV	VQ	QKLAELERQ	SGGRLG	VALINTADNSQ	60
CTX-M-15	1	MVKKSLRQFTLMATATVTL	LLG	SV	FLYAQTADV	VQ	QKLAELERQ	SGGRLG	VALINTADNSQ	60
CTX-M-02	1	MMTQSI	RRSMLTVMATL	PLLF	SSATLHAQANSV	QQQL	EAL	EKSSGGRLG	VALINTADNSQ	60
		M+ +S+R+ L	AT+ LL	S L+AQ	VQQ+L	LE+ SGGRLG	VALINTADNSQ			
CTX-M-15	1	MVKKSLRQFTLMATATVTL	LLG	SV	FLYAQTADV	VQ	QKLAELERQ	SGGRLG	VALINTADNSQ	60
CTX-M-01	1	MVKKSLRQFTLMATATVTL	LLG	SV	FLYAQTADV	VQ	QKLAELERQ	SGGRLG	VALINTADNSQ	60
		MV K +++	A A +	LLGS	FLYAQT+ VQQ	KL	LE+ SGGRLG	VALI+TADN+Q		
CTX-M-14	1	MVTKR	VRQRMF	AAAACI	PLLLG	SAPLYAQT	SAVQQ	KLAALEK	SSGGRLG	VALIDTADNTQ
CTX-M-08	1	MMRHR	VKRMIMLTTACI	SLLG	SAPLYAQANDV	VQ	QKLALEK	SSGGRLG	VALIDTADNAQ	60
		MMR V+R	+LMTTAC+SLLL	S	FLYAQAND+QQ	KLAALEK	SSGGRLG	VALI+TADN Q		
CTX-M-78	1	MMRKS	VRRAILMTTACV	SLLS	ASVFLYAQANDI	QQ	KLAALEK	SSGGRLG	VALINTADNTQ	60

Fig. 6.1 NH₂-terminal amino acid divergence of different lineages of blaCTX-M. Sixty N-terminal amino acids were compared between CTX-M-1 and CTX-M-2, CTX-M-1 and CTX-M-9, CTX-M-2 and CTX-M-9, CTX-M-1 and CTX-M-15, etc., to show differences. Such analysis clearly indicated that common primers for all CTX-M β-lactamases are hard to find

CTX-M-159, CTX-M-168, and CTX-M-174, CTX-M-196, CTX-M-198, CTX-M-201, CTX-M-213, CTX-M-215, CTX-M-219, CTX-M-221, CTX-M-223 and CTX-M-233 isolates. The minor classes of CTX-M enzyme could be divided into at least three classes: CTX-M-8 including CTX-M-40, CTX-M-63, and CTX-M-152; CTX-M-25 including CTX-M-26, CTX-M-39, CTX-M-41, CTX-M-91, CTX-M-94, and CTX-M-160; and CTX-M-CHIM. In Fig. 6.1, we showed the differences of the 60 N-terminal amino acids among the different CTX-M β-lactamase isomers. Alignment of CTX-M with TEM, SHV, and KPC β-lactamases showed less homology. (i) TEM-1 and SHV-1 has strong AA similarities after first 20 AA and up to AA 180 and then start decreases again up to AA 286 C-terminal end. (ii) TEM-1 and SHV-1 have less sequence similarity with CTX-M (~38%) and KPC (~44%) enzymes with short stretch of similarity at 133–137 (GGP), 147–150 (TAF), 164–167 (RLDR), and 189–183 (RDTT). (iii) KPC and CTX-M have 52% similarity from 140 AA to 240 AA (AELSAAA, TFRLDR, KGGNTG) indicating related ancestral (data not shown). In Fig. 6.2, the representative amino acid homology positions were shown between diverged CTX-M-1, CTX-M-2, and CTX-M-9. Such positions multiplied by three were used to check the DNA sequence homology positions. In Fig. 6.3, we showed how CTX-M-1 vs CTX-M-3 and CTX-M-2 vs CTX-M-4 seq-2 were aligned and then assembled into MS Word Data Sheet to pick up the homology between class-1 and class-2 blaCTX-M genes. Such alignment gave the forward primer as 5'-AAC AC(C/A) GC(C/A) GAT AAT TCG CA-3'.

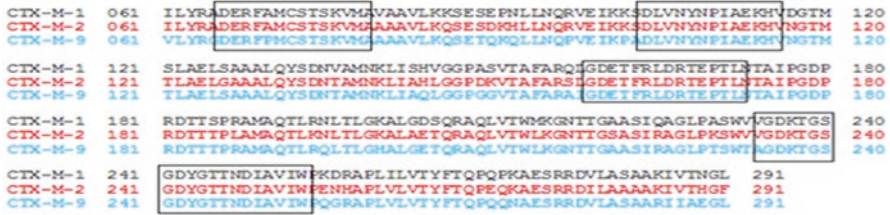


Fig. 6.2 Amino acid homology among CTX-M-1, CTX-M-2, and CTX-M-9 major classes of CTX-M beta-lactamases (36). AA positions 61–291 were used and boxed where maximum homology was found



Fig. 6.3 Discovery of homology region of class I and class II lineages of *bla_{CTX-M}* for primer design. Coding sequences were 63–938 in accession no. X92506, 6–881 in accession no. X92507, 2106–2981 in accession no. KF05540, and 1–876 in accession no. Y14156

The reverse primer obtained initially had no degeneracy (5'-CCG CGA TAT CGT TGG TGG TG-3') and aligned to CTX-M (CTX-M-1 to CTX-M-7, CTX-M-11, CTX-M-12, CTX-M-15, CTX-M-20, CTX-M-22, CTX-M-23, CTX-M-28 to CTX-M-32, CTX-M-35, CTX-M-36, CTX-M-41, CTX-M-43, CTX-M-44, CTX-M-52 to CTX-M-54, CTX-M-56, CTX-M-62, CTX-M-64, CTX-M-66, CTX-M-69, CTX-M-71, CTX-M-72, CTX-M-79, CTX-M-82, CTX-M-92, CTX-M-96, CTX-M-97, CTX-M-101, CTX-M-103, CTX-M-107 to CTX-M-109, CTX-M-114, CTX-M-116, CTX-M-131, CTX-M-132, CTX-M-155 to CTX-M-157, CTX-M-166, CTX-M-167, CTX-M-170 to CTX-M-173, CTX-M-175, CTX-M-176) but not aligned to many such as CTX-M (CTX-M-8, CTX-M-10, CTX-M-13, CTX-M-14, etc.). It was found that primer 5'-CCG GAA TAT CAT TGG TGG TG-3' aligned to CTX-M-9, CTX-M-13, CTX-M-14, CTX-M-16 to CTX-M-19, CTX-M-21, CTX-M-24, CTX-M-27, CTX-M-38, CTX-M-51, CTX-M-65, CTX-M-67, CTX-M-68, CTX-M-83 to CTX-M-86, CTX-M-90, CTX-M-93, CTX-M-99, CTX-M-102, CTX-M-104, CTX-M-105, CTX-M-106, CTX-M-110 to CTX-M-113, CTX-M-121, CTX-M-125, CTX-M-126, CTX-M-129, CTX-M-130, CTX-M-147, CTX-M-148, CTX-M-168, and CTX-M-174. Thus, the degenerative primer 5'-CCG C(G/A)A TAT C(G/A)T TGG TGG TG-3' covered most CTX-M isomers including CTX-M-74, CTX-M-169, and CTX-M-177 (having single nucleotide change (G = A)). Still CTX-M-115 has 2–20 nucleotide alignments, and CTX-M-10, CTX-M-34, CTX-M-37, CTX-M-53, and CTX-M-68 have 1–19 nucleotide alignments

A. NCBI BLAST Search of forward primer CTX-MF

Description	Max score	Query cover	E value	Ident	Accession number
CTX-M-15	34.4	100%	9.4	90%	gi 961556391 KT318935.1
plasmid	34.4	100%	9.4	90%	gi 966626646 CP013657.1
CTX-M-171	34.4	100%	9.4	90%	gi 961350022 KT277545.1
CTX-M-15	34.4	100%	9.4	90%	gi 961349988 KT265731.1
CTX-M-15	34.4	100%	9.4	90%	gi 961349986 KT265730.1
CTX-M-15	34.4	100%	9.4	90%	gi 961349984 KT265729.1
CTX-M-15	34.4	100%	9.4	90%	gi 958572088 KT001477.1
CTX-M-15	34.4	100%	9.4	90%	gi 958572068 KT001476.1
Plasmid	34.4	100%	9.4	90%	gi 959147947 CP012988.1
Plasmid	34.4	100%	9.4	90%	gi 959153704 CP012993.1

B. NCBI BLAST Search for Reverse primer CTX-MR

Description	Max score	Query cover	E value	Ident	Accession
plasmid pHeBE7	34.4	100%	9.4	90%	gi 962148759 KT002541.1
plasmid pCT-KPC	34.4	100%	9.4	90%	gi 961666360 KT185451.1
plasmid pEC012, complete	34.4	100%	9.4	90%	gi 961494526 KT282968.1
CTX-M-171 gene	34.4	100%	9.4	90%	gi 961350022 KT277545.1
CTX-M-15 gene, complete	34.4	100%	9.4	90%	gi 961349988 KT265731.1
IS26 and blaCTX-M-15 g	34.4	100%	9.4	90%	gi 958572068 KT001476.1
Klebsiella plasmid	34.4	100%	9.4	90%	gi 959153704 CP012993.1
Klebsiella plasmid pKp01a	34.4	100%	9.4	90%	gi 959147947 CP012988.1
E coli plasmid pEC3157	34.4	100%	9.4	90%	gi 873464024 KR259130.1
E cloacae CTX-M-177	34.4	100%	9.4	90%	gi 949394543 KT997889.1
Klebsiella CTX-M-176	34.4	100%	9.4	90%	gi 949394541 KT997888.1

Fig. 6.4 BLAST analysis of (a) forward primer and (b) reverse primer of *bla*_{CTX-M} (36). Both primers recognize the *Enterobacteriaceae* plasmids (accession nos. KR046918, CP012993, CP012988), integron ISEcp1 (accession nos. KT001477, KT201629), recently isolated CTX-M mutants (accession nos. KT251041, KP727572), as well as very mobilized CTX-M-15 ESBL (accession nos. KT277545, KT001477)

indicating sequencing mismatch errors of one nucleotide. However, CTX-M-8, CTX-M-25, CTX-M-26, CTX-M-40, CTX-M-89, CTX-M-91, CTX-M-94, CTX-M-152, CTX-M-159, and CTX-M-160 have a discrepancy of 10 nucleotide alignments (~6% of total 185 isomers). Such analysis gave the final reverse degenerative primer as 5'-CCG CRA TAT CRT TGG TGG TG-3' hoping possible sequencing errors in those mismatches because of large plasmids sequenced from different laboratories with multiple sequence data depositions.

In Fig. 6.4, we presented the BLAST search data for primers as both CTX-M-1 and CTX-M-2 variants were selected in plasmids and integron sequences including most abundant CTX-M-15 variant, and no unwanted DNA sequences were selected (500 individual sequences searched) to show primer specificity. We performed the primer analysis by OligoAnalyzer 3.1 software for self-dimer formation and hairpin structures and confirmed the primer's good characters. Both forward primer and reverse primer for very unstable dimer and hairpin structures. The forward primer has GC% (45–50%), T_m (59.9–64.3 °C), MW (6079 g/mole), nmole/OD₂₆₀ (4.97), extinction coefficient [201,400 L/(mole.cm)], hairpin structures (ΔG = - < -0.81; T_m < 38 °C), and weak self-dimer (-2.4 Kcal/mol). Similarly the reverse primer has GC% (55%), T_m (60.9–64.5 °C), MW (6164 g/mole), nmole/OD₂₆₀ (5.27), extinct

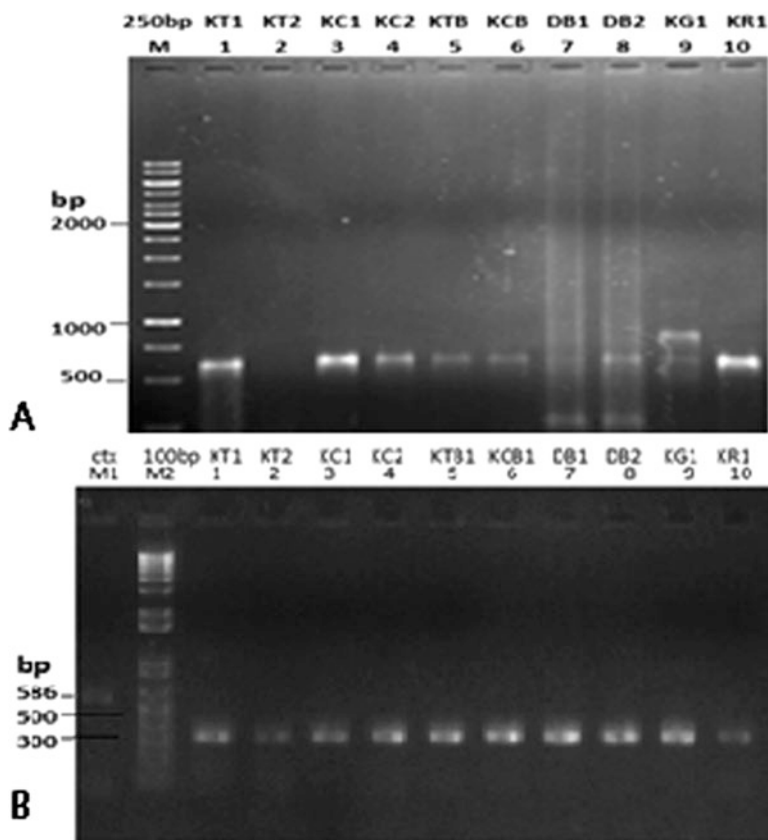


Fig. 6.5 PCR analysis of *mdr* genes in plasmids (36). Plasmids were isolated from ten ampicillin-, tetracycline-, cefotaxime-, chloramphenicol-, and streptomycin-resistant MDR bacteria of Kolkata with accession nos. KU769875-KU769883. (a) *bla*_{CTX-M} gene (type-1/type-2)-specific universal primers (586 bp). (b) *bla*_{TEM-SHV} common universal primers (312 bp). Such analysis also confirmed *acrAB*, *mcr*, and *tetA* gene abundance in those MDR bacteria [3]

coefficient [189,700 L/(mole.cm)], hairpin structures ($\Delta G = - < 0.86$ with T_m 13.2 °C), and self-dimer (-9.53 Kcal/mol). In Fig. 6.5, we showed the PCR analysis of MDR bacterial plasmid DNA. Ten MDR bacteria were easily isolated from rain water, Bay of Bengal Sea water, and Ganga River water located near Kolkata City of India by drug selection in vitro as described previously [3]. The ten clones contained *bla*_{TEM-1} and mostly *bla*_{CTX-M-1/15} isomers except KT-2 isolate. Further, all MDR isolates produced expected band for *bla*_{TEM} gene, but CTX-M primer produced few low- and high-molecular bands indicating recombination of the genes and repetitive sequences (Fig. 6.5). The color dideoxy sequencing confirmed the *bla*_{TEM-1} gene and *bla*_{CTX-M-1} gene (Fig. 6.6). Surprisingly, tem-shv universal primers gave 0.3 kb expected band that all are *bla*_{TEM-1} type, and no *bla*_{SHV} gene was detected by color dideoxy sequencing (Fig. 6.6). Nevertheless, all data confirmed the universality and

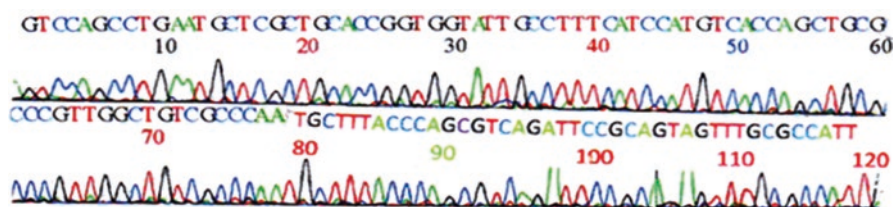


Fig. 6.6 Chromatogram of color dideoxy sequencing for *bla*_{CTX-M} gene. The PCR products as in Fig. 6.5 using reverse *bla*_{CTX-M} gene primer and confirmed the *bla*_{CTX-M-1} gene in Kolkata superbugs (see accession nos. MF278956 and MF278957 for *bla*_{TEM-1} sequence)

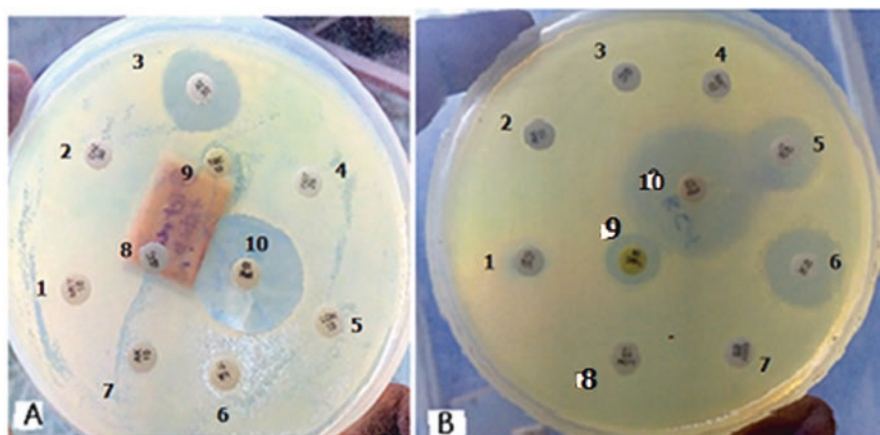


Fig. 6.7 Antibiotic paper disk assay of Kolkata superbugs (36, 37). Those are KT-1, KC-2, and KG-12 and DMT-1 strains. In (a) KG-12 isolate: 1 = MET-10, 2 = CAZ-30, 3 = AT-50, 4 = COT-25, 5 = LOM-15, 6 = VA-10, 7 = AK-10, 8 = LZ-10, 9 = TGC-10 and 10 = IMP-10. In (b) KC-1 isolate: 1 = VA-10, 2 = AK-10, 3 = LN-10, 4 = MET-10, 5 = CAZ-30, 6 = AT-50, 7 = COT-25, 8 = LOM-15, 9 = TGC-15, and 10 = IMAP-10

selectivity of the common *bla*_{CTX-M} and *bla*_{TEM-SHV} primers. We conclude that TEM-1 and CTX-M-1 genes are highly present in Kolkata superbugs as described previously in India and abroad. We also have presented few data on the Kolkata superbug isolation and its inhibition by herbal extracts (Figs. 6.7 and 6.8). Thus, we are working on detection as well as control of superbug.

6.4 Discussion

Cefotaxime is a potent third-generation cephalosporin and widely kills many *Enterobacteriaceae* and other deadly pathogens. Bla_{CTX-M} enzyme cleaves cefotaxime, and such bacteria are very resistant to many β -lactams and need a combination therapy (linezolid+colistin+amikacin) to cure. PCR amplification of CTX-M variants had been suggested in patients who did not respond to ampicillin,

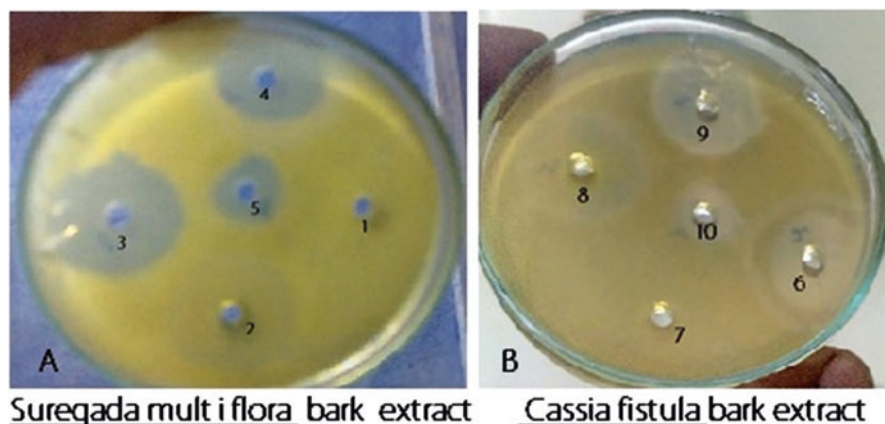


Fig. 6.8 High antibacterial activities of ethanol plant extracts (36, 38). Naringa bark extract (a) and Bandor lathi bark extract (b) on *Pseudomonas aeruginosa* DB-2_mdr (accession no. KY769876). (a) Lane 1, ampicillin 10 μ l (50 mg/ml); lane 2, tetracycline 10 μ l (20 mg/ml); lane 3, 50 μ l Naringa bark extract; lane 4, 10 μ l (2 mg/ml imipenem); and lane 5, 10 μ l (5 mg/ml faropenem). (b) Lane 6, 50 μ l Naringa extract; lane 7, ampicillin 10 μ l (50 mg/ml); lane 8, 50 μ l Bandor lathi ethanol extract; lane 9, 10 μ l (2 mg/ml imipenem); and lane 10, 10 μ l (5 mg/ml faropenem)

amoxicillin-clavulanate, and cefotaxime. We have presented data to prove that major three distinct lineages of CTX-M enzymes could be identified by common primers for PCR diagnostics of the *bla*_{CTX-M} genes. We are also first to perform complete bioinformatics analysis of >300 *bla*_{CTX-M} genes fully sequenced (data not shown). We have found high divergence in type-1, type-2, and type-9 CTX-M and CMY/VIM β -lactamase enzymes, and we have presented the analysis of CTX-M only. Recently, worldwide identification and control of multidrug-resistant bacteria were commissioned among G7 and G20 countries as recommended by the WHO and AMR Report 2018 [13]. PCR detection of *mdr* genes is an important tool other than Kirby-Bauer drug sensitivity test to detect the spread of ESBL and MBL phenotypes. Sadly in India PCR diagnostic approach has not yet been approved by the Indian Government due to poor infrastructure in villages. Indeed, hundreds of PCR reactions will be performed to know the AMR status of a single clinical isolate, which is costly and impractical in poor nations.

The different primers were designed by different workers as follows: Saladin et al. [14], Li and Li [15], Park et al. [16], Lee et al. (2005) [17], Dallenne et al. [18], Parveen et al. [19], Guo et al. [20], and more. The analysis suggested that such multiple primers had problems as no uniform strategy was followed.

Parveen RM et al. (2012) described primers that could amplify CTX-M-1, CTX-M-2, and CTX-M-9 groups as follows: CTXm-A1 = 5'-SCS ATG TGC AGY ACC AGT AA-3' and CTXm-A2 = 5'-CCG CRA TAT GRT TGG TGG TG-3' (450 bp amplicon for groups 1, 2, and 9, where S = C/G; Y = C/T; R = A/G). However, they made another primer set for CTXm-8 and CTXm-25 and indicated their effort to get a common primer for all CTX-M variants had gone in vain [19]. The primers are

as follows: CTXm-825F = 5'-CGC TTT GCC ATG TGC AGC ACC-3' and CTXm-825R = 5'-GCT CAG TAC GAT CGA GCC-3'. The analysis suggested that although they had tried to get a consensus sequence for CTX-M-1 and CTX-M-2 variants, they failed to locate the most conserved region that we described here for blaCTX-M mutants. Further, CTXm-A1 primer was found good, but CTXm-A2 has homology to acrR/tetR-type transcription factor which were present in many MDR plasmids and also hybridized to many chromosomes such as *Drosophila melanogaster* (accession no. AC004295). Guo et al. [20] used only one set of primer for CMY, CTX-M, TEM, etc., as follows: CMYF = 5'-GAC GCC TCT TTC TCC ACA-3' and CMYR = 5'-TGG AAC GAA GGC TAC GTA-3' (1146 bp); CTX-MF = 5'-TTT GCG ATG TGC AGT ACC AGT AA-3' and CTXMR = 5'-CGA TAT CGT TGG TGG TGC CAT A-3'(544 bp); and TEMF = 5'-ATA AAA TTC TTG AAG ACG A-3' and TEMR = 5'-GAC AGT TAC CAA TGC TTAA TC-3' (1080 bp), respectively. CTX-MF primer was aligned to CTX-M-2, CTX-M-5, CTX-M-31, CTX-M-35, CTX-M-43, CTX-M-44, CTX-M-56, CTX-M-97, CTX-M-141, CTX-M-165, and CTX-M-171; all were type-2 CTX-M isomers [20]. Similarly CTX-MR was aligned by BLAST to many CTX-M-15 (accession nos. LC095497-LC095574) and CTX-M-173, CTX-M-175, and CTX-M-176; again all are type-2 blaCTX-M isomers, thus reducing the chance of CTX-M detection about 50%. It appeared that all primers had different types of problems and were not designed systematically.

A recent molecular study conducted in Croatia with 68 carbapenemases (64 VIM, 9 NDM-1, and 2 OXA-48) producing strains of *E. cloacae*, *K. pneumoniae*, and *E. freundii* where 64, 30, and 18 strains showed additional TEM, CTX-M-15, and CMY co-transmissions suggesting again that superbug strains contain clinically significant CTX-M-15 cefotaximase variants [21]. A contrasting finding was reported in China with blood-borne ESBL *Escherichia coli* (B2 and ST131) where CTX-M-14/CTX-M-15/CTX-M-55 was frequent with predominant CTX-M-15 (40%), but no carbapenemase gene was detected but *tet* and *qnr* drug efflux genes [22]. We also could not find MBLs in our study, and major plasmids carry *tet*, *cmr*, *acrAB*, *blaTEM-1*, and *blaCTX-M-1/15* types of *mdr* genes [3]. A 2015 study in Brazil indicated that significant ESBL enzymes in *Escherichia coli* and *K. pneumoniae* were CTX-M-15 but also CTX-M-2 and infrequent CTX-M-8/CTX-M-9/CTX-M-59 suggesting that our primers' inability to select CTX-M-8 had minor limitations [23]. However, all studies with CRE and ESBL enzymes CTX-M-1/CTX-M-3/CTX-M-15 were clinically significant, and we could ignore other variants of CTX-M in a routine AMR assay in Indian subcontinents [7]. We found CTX-M-1 isomer rather than CTX-M-2 and CTX-M-9 although a complete sequence of the genes was necessary to define between CTX-M-1 and CTX-M-15. However, bla_{TEM} is very frequent in Kolkata superbugs with association of bla_{CTX-M}, but bla_{SHV} was infrequent [24, 25]. Gaining mutations means gaining extra power to hydrolyze new antibiotic derivatives. For example, most early ESBL CTX-M enzymes (CTX-M-1 to CTX-M-25) did not hydrolyze ceftazidime, but CTX-M-64, CTX-M-123, CTX-M-132, CTX-M-137, and CTX-M- did it well. Such discoveries are frightening for patients but more seriously produce a noise in drug industry

in granting more funds for new antibiotic discovery from fungi and actinomycetes or virtual chemical synthesis targeting MDR bacteria. We need to know the mechanism of MDR mutant selection which likely occurs in the gastrointestinal tract or blood of patients during therapy but also in environmental water with the presence of toxic chemicals, heavy metals, paints, and detergents. Why β -lactamases are involved rapidly is a gaining question! But contamination of sea and river water with penicillin and tetracycline is deadly to thing for the twenty-first-century scientific community of this Earth. Such drugs at ng concentration could induce many operons causing overexpression of MDR enzymes and AMR. Sadly, we have also overlooked the millions of research laboratories that are doing recombinant DNA research with *amp/tet/neo/cat* genes containing plasmids and would be contributing to antibiotic contamination in water and a source of *mdr* gene accumulation in conjugative plasmids of superbugs.

6.5 Conclusion

PCR detection of *mdr* genes thus appears complex. We attempted to reduce the PCR reactions in CTX-M assay, and we were analyzing the other *bla* genes such as TEM/SHV/CMY/VIM and very diverged *aac_{A1/C1}* (AG acetyltransferases) and *mex_{AB}* (proton drug efflux genes). It appeared >20 sets of primers for drug efflux genes (*acrAB*, *mexAB*, *tetA* etc.) and >20 sets for drug-modifying genes (*aad*, *aac*, *aph*) are necessary to understand the AMR status [26]. Thus, the search for common PCR primers for *bla mdr* genes is an important step of AMR management. Indeed ~100–500 kb MDR plasmids are increasing in the GenBank database and also have been located in MDR islands of chromosomes [7]. In truth, multiple *mdr genes* could be found in both cassette chromosomes and conjugative plasmids of superbugs [27]. We developed here a universal primer for *bla_{CTX-M}* genes which are ESBL with more than a hundred of combination mutations and resistant to penicillin and cephamycin. For example, *bla_{CTX-M-80}* gene had substitution Ala-27- > Val as compared to CTX-M-3, and *bla_{CTX-M-81}* gene has Lys- > Glu, Lys- > Gln, and Asn- > His changes at positions 82, 98, and 132 compared to CTX-M-14. Similarly, CTX-M-87 has substitutions Ala77- > Val and Pro167- > Leu and has potent hydrolytic activity against cefotaxime than against ceftazidime, as compared to clinically significant CTX-M-14. CTX-M-94 and CTX-M-100 belonged to the CTX-M-25-group with the substitution V77- > A, F119- > L, and D240- > G conferred increased resistant to ceftazidime and ceftriaxone. This reflects that the detection of active mutations in *mdr* genes is important for careful monitoring of the superbug spread. Many good hospitals have started screening of *mdr* genes and drug sensitivity tests before prescribing antibiotics. We have created problems using repeated doses of antibiotics for a long time killing gut microbes which supply us vitamins which are absolutely necessary but we have not been able to make drug sensitivity tests universal. WHO advises for proper antibiotic use and to take vitamin complex and probiotics during antibiotic treatment as it appears that combination therapy is a must in the recent time due to AMR.

The AMR Report on “Review on Antimicrobial Resistance” and recommendations to “Tackling Drug-Resistant Infection Globally” by international experts chaired by Jim O’Neill, England, page 73, May 2016, has extended views to reduce use of antibiotics in agricultural land and their contamination into the environment, improve global surveillance of MDR in humans and animals, and promote quick diagnostics to reduce use of drugs [26]. In Science 18th August 2016, Dr. R Laxminarayan and co-workers have pointed out the requirement of hard targets, adequate funding and one health governance structure (surveillance and therapy) worldwide to combat AMR. In truth, the Antibiotic Surveillance Committee concluded that 1/3 reduction in antibiotic prescription drugs could possibly reduce AMR-associated infections without affecting therapeutic targets and efficacy. MDR bacteria are in the air, rain, and seawater affecting this globe [3, 27]. So it is time to act seriously with a uniform policy worldwide [28, 29]. One such requirement is to register and deposit all MDR mutant strains in one site (e.g., ATCC) to make sure of the authenticity of superbugs generated and their easy availability for research. G20 Nations got together in Berlin (May 2017) to strengthen such efforts [30–32]. Superbug *mdr* genes’ (*bla*, *aac*, *aph*) heterogeneity have reached maximum, and thus our effort to make universal primers for easy superbug diagnosis is important [33–35]. Most importantly, we are engaged in herbal drug design (MDR-Cure) and have contributed significantly [35–37]. Some critic commented that we had no clinical MDR isolate, and we recently tested one MDR *E. coli* isolated at the Medical College and the superbug was equally inhibited by MDR-Cure.

Acknowledgment We thank Prof. Bidyut Bandyopadhyay for intellectual comments on the article and Late Dr. J. B. Medda of the OAER for the financial support.

References

1. Laxminarayan R, Duse A, Watal C et al (2013) Antibiotic resistance. *Lancet Infect Dis* 13:1057–1098
2. Chakraborty AK (2016) In silico analysis of hotspot mutations in the bacterial NDM-1 and KPC-1 carbapenemases. *Biochem Biotechnol Res* 4(1):17–26
3. Chakraborty AK (2015) High mode contamination of multi-drug resistant bacteria in Kolkata. *Indian J Biotechnol* 14:149–159
4. McKenna M (2013) Antibiotic resistance. *Nature (London)* 499:394–396
5. Mataseje LF, Peirano G, Church DL et al (2016) Colistin non-susceptible *Pseudomonas aeruginosa* ST654 with *bla*NDM-1 arrives in North America *Antimicrob Agents Chemother* pii: AAC02591-15
6. Li X-Z, Plésiat P, Nikaido H (2015) The challenge of efflux-mediated antibiotic resistance in Gram-negative bacteria. *Clin Microbiol Rev* 28:337–418. <https://doi.org/10.1128/CMR.00117-14>
7. Chakraborty AK (2016) Complexity, heterogeneity, 3-D structures and transcriptional activation of multi-drug resistant clinically relevant bacterial beta-lactamases. *Trends Biotechnol* open Access 2(1):1–001
8. Ambler RP (1980) The structure of β -lactamases. *Phil Trans R Soc London* 289:321–331
9. Bush K, Jacoby GA, Medeiros AA (1995) Functional scheme for β -lactamases and its correlation with molecular structure. *Antimicrob Agents Chemother* 39(6):1211–1233

10. Poirel L, Kampfer P, Nordmann P (2002) Chromosome-encoded Ambler class A beta-lactamase of *Kluyvera georgiana*, a probable progenitor of a subgroup of CTX-M extended-spectrum beta-lactamases. *Antimicrob Agents Chemother* 46(12):4038–4040
11. Wang H, Kelkar S, Wu W et al (2003) Clinical isolates of *Enterobacteriaceae* producing extended-spectrum beta-lactamases. *Antimicrob Agents Chemother* 47:790–793
12. Yamasaki Y, Komatsu M, Yamashita T (2003) Production of CTX-M-3 extended-spectrum beta-lactamases and IMP-1 metallo-beta-lactamase by five Gram-negative bacilli. *Antimicrob Agents Chemother* 51:631–638
13. Ensor VM, Shahid M, Evans JT et al (2006) Occurrence, prevalence and genetic environment of CTX-M beta-lactamases in Enterobacteriaceae from Indian hospitals. *J Antimicrob Chemother* 58:1260–1263
14. Saladin M, Cao VT, Lambert T et al (2002) Diversity of CTX-M beta-lactamases and their promoter regions from Enterobacteriaceae isolated in three Parisian hospitals. *FEMS Microbiol Lett* 20(2):161–168
15. Li H, Li JB (2005) Detection of five novel CTX-M-type extended spectrum beta-lactamases with one to three CTX-M-14 point mutations in isolates from Hefei, Anhui Province, China. *J Clin Microbiol* 43(8):4301–4302
16. Park YJ, Park SY, Oh EJ et al (2005) Occurrence of extended-spectrum beta-lactamases among chromosomal AmpC-producing *Enterobacter cloacae*, *Citrobacter freundii*, and *Serratia marcescens* in Korea and investigation of screening criteria. *Diagn Microbiol Infect Dis* 51(4):265–269
17. Lee S, Park Y-J, Kim M et al (2005) Prevalence of Ambler class A and D beta-lactamases among clinical isolates of *Pseudomonas aeruginosa* in Korea. *J Antimicrob Chemother* 56:122–127
18. Dallenne C, Da Costa A, Decré D et al (2010) Development of a set of multiplex PCR assays for the detection of genes encoding important beta-lactamases in Enterobacteriaceae. *J Antimicrob Chemother* 65(3):490–495
19. Parveen RM, Subha Manivannan S, Harish BN et al (2012) Study of CTX-M type of extended spectrum beta-lactamase among nosocomial isolates of *Escherichia coli* and *Klebsiella pneumoniae* in South India. *Indian J Microbiol* 52(1):35–40
20. Guo YF, Zhang WH, Ren SQ et al (2014) IncA/C plasmid-mediated spread of CMY-2 in multidrug-resistant *Escherichia coli* from food animals in China. *PLoS One* 9(5):e96738
21. Bedenic B, Sardelic S, Luxner J et al (2016) Molecular characterization of class B carbapenemases in advanced stage of dissemination and emergence of class D carbapenemases in *Enterobacteriaceae*. *Infect Genet Evol*. pii: S1567-1348(16)30183-6
22. Wang S, Zhao SY, Xiao SZ et al (2016) Antimicrobial resistance and molecular epidemiology of *Escherichia coli* causing bloodstream infections in three hospitals in Shanghai, China. *PLoS One* 11(1):e0147740
23. Rocha FR, Pinto VP, Barbosa FC (2016) The spread of CTX-M-type extended-spectrum beta-lactamases in Brazil: a systematic review. *Microb Drug Resist* 22(4):301–311
24. Bora A, Hazarika NK, Shukla SK et al (2014) Prevalence of blaTEM, blaSHV and blaCTX-M genes in clinical isolates of *Escherichia coli* and *Klebsiella pneumoniae* from Northeast India. *Indian J Pathol Microbiol* 57:249–254
25. George EA, Sankar S, Jesudasan MV et al (2015) Molecular characterization of CTX-M type extended spectrum beta-lactamase producing *E coli* isolated from humans and the environment. *Indian J Med Microbiol* 33(Suppl S1):73–79
26. O'Neill J (2016) Review on antimicrobial resistance. Tackling a crisis for the health and wealth of nations London Review on antimicrobial resistance 2016. <https://amr-review.org/sites/default/files/>
27. Chakraborty AK (2016) Multi-drug resistant genes in bacteria and 21st century problems associated with antibiotic therapy. *Biotechnol Ind J* 12(12):114
28. Blair JMA, Webber MA, Baylay AJ et al (2015) Molecular mechanisms of antibiotic resistance. *Nat Rev Microbiol* 13:42–51. <https://doi.org/10.1038/nrmicro3380>

29. World Health Organization (2014) Antimicrobial resistance: global report on surveillance. World Health Organization, Geneva, Switzerland. http://apps.who.int/iris/bitstream/10665/112642/1/9789241564748_eng.pdf
30. Laxinarayan R, Chaudhury RR (2016) Antibiotic resistance in India. Drivers and opportunities for action. *PLoS Med* 13:e1001974
31. Chakraborty AK (2017) Multi-drug resistant bacteria from Kolkata Ganga River with heterogeneous MDR genes have four hallmarks of cancer cells but could be controlled by organic phyto-extracts. *Biochem Biotechnol Res* 5(1):11–23
32. Chakraborty AK (2017) MDR genes are created and transmitted in plasmids and chromosomes to keep normal intestinal microbiota alive against high dose antibiotics- a hypothesis. *J Mol Med Clin Appl* 2(1):109. <https://doi.org/10.16966/2575-0305.109>
33. Chakraborty AK (2019) Current status and unusual mechanism of multi-resistance in *Mycobacterium tuberculosis*. *J Health Med Informatics* 10(1):328. <https://doi.org/10.4172/2157-420.1000328>
34. Chakraborty AK, Pradhan S, Das S, Maity M, Sahoo S, Poria K (2019) Complexity of OXA beta-lactamases involved in multi-resistance. *British J Bio-Medical Res* 3(1):772–798. <https://doi.org/10.24942/bjbm.2019.424>
35. Chakraborty AK, Poiria K, Saha D, Halder C, Das S (2018) Multidrug- resistant bacteria with activated and diversified MDR genes in Kolkata water: ganga action plan and heterogeneous phyto-antibiotics tackling superbug spread in India. *Am J Drug Deliv Ther* 5(1):1–9
36. Chakraborty AK, Nandi SK (2019) A method of universal primer design for the detection of diverged CTX-M beta-lactamases in multi-drug resistant superbugs. *Res Rev J Biotechnol* 9(2):1–10
37. Chakraborty AK (2017) Ganga action plan, heterogeneous phyto-antibiotics and phage therapy are the best hope for India tackling superbug spread and control. *Ind J Biol Sci* 23:34–51



Lipopeptides as Therapeutics: Molecular Docking and Drug Design

7

Satya Eswari Jujjavarapu and Swasti Dhagat

Abstract

The rise of antibiotic-resistant pathogens has led to an urgent requirement of potent and safe antimicrobial compounds. Lipopeptides produced as secondary metabolites by some organisms have shown a broad range of anti-pathogenic activities, while some have anti-cancerous properties as well. Among all the lipopeptides, daptomycin has gained popularity as biopharmaceutical. In order for the lipopeptides to be used as drugs, *in silico* drug designing of these compounds should be performed which enables the identification of the presence of binding sites in lipopeptides for their corresponding ligands. In this study, molecular docking of daptomycin with its ligands was performed as a method of designing novel drug. After the identification of ligands, namely, D-alanine, decanoic acid, D-asparagine, D-serine, (2S)-2-amino-4-(2-aminophenyl)-4-oxobutanoic acid, and (2S,3R)-2-azanyl-3-methyl-pentanedioic acid, using RSCB, Schrödinger software was used to dock daptomycin with their corresponding ligands. After the identification of ligands, they were made to dock with daptomycin. The parameters for docking were docking score and glide energy. Out of the six identified ligands of daptomycin, only three were found to dock with it with docking scores of -3.229 (for D-alanine), $-$ (for D-asparagine), and -4.216 (for D-serine). Their respective glide energies were -13.678 kcal/mol (D-alanine), -22.56 kcal/mol (D-asparagine), and -12.042 kcal/mol (D-serine).

Keywords

Antimicrobial peptides · Lipopeptides · Daptomycin · Molecular docking · Drug design · *In silico*

S. E. Jujjavarapu (✉) · S. Dhagat

Department of Biotechnology, National Institute of Technology Raipur (CG), Raipur, India

e-mail: Satyaeswarj.bt@nitrr.ac.in; sdhagat.phd2016.bt@nitrr.ac.in

© Springer Nature Singapore Pte Ltd. 2020

P. C. Sadhukhan, S. Premi (eds.), *Biotechnological Applications in Human Health*, https://doi.org/10.1007/978-981-15-3453-9_7

61

7.1 Introduction

The rise in antibiotic resistance among different bacterial species has become a great threat to public throughout the world. The Infectious Diseases Society of America has classified *Enterobacter* sp., *Acinetobacter baumannii*, *Pseudomonas aeruginosa*, and *Klebsiella pneumoniae* as the antibiotic-resistant bacterial pathogens. The Centre for Disease Control and Prevention (CDC), in 2013, declared the post-antibiotic era for human race, whereas the World Health Organization (WHO), in 2014, reported that the problem of antibiotic-resistance has become calamitous [1]. The list of antibacterial pathogens includes various Gram-positive and Gram-negative bacteria, such as penicillin-resistant *Streptococcus pneumonia* (PSRP), vancomycin-resistant enterococci (VRE) and methicillin-resistant *Staphylococcus aureus* (MRSA), *Escherichia coli*, *Klebsiella pneumoniae*, *Acinetobacter*, *Pseudomonas aeruginosa*, and *Neisseria gonorrhoeae* [2].

Overuse of antibiotics and their inapt prescriptions, lack of development, and availability of new drugs and stringent regulations in the approval of new pharmaceutical products have led to antibiotic-resistant strains of bacteria [3]. Hence, it becomes a necessity to discover or develop new antibacterial agents that are active and have diverse modes of action [4]. Antimicrobial peptides (AMPs), being natural, universal, and genetically encoded, are an alternative to current antibiotics [5–7]. Low-molecular-weight antimicrobial peptides (AMPs) have multiple functions [8]. They have both hydrophobic and hydrophilic groups and thus are amphiphilic molecules. Because of this nature of AMPs, they are soluble in an aqueous environment and enter lipid-rich membranes. Hence, they increase the permeability of microbial membrane and kill the cells. These are active against a variety of bacteria, fungi, and viruses [8]. Lipopeptides, a class of AMPs, have a lipid tail connected to a linear or cyclic short oligopeptide [9, 10]. Cyclic lipopeptides, consisting of lactone or lactam ring, are synthesized by non-ribosomal pathway. Many species of microorganisms, namely, *Streptomyces*, *Bacillus*, *Pseudomonas*, and *Actinomycetes*, produce lipopeptides as secondary metabolites [10]. Lipopeptides secreted by microorganisms include daptomycin, polymyxin, surfactin, iturin, bacillomycin, and paenilarvins among several others. Daptomycin, produced by *Streptomyces roseosporus*, acts against infections by Gram-positive organisms. Insertion of daptomycin into the cell membrane leads to its aggregation in the membrane and creation of hole which results in depolarization of membrane. This, ultimately, will inhibit the synthesis of DNA, RNA, and protein causing cell death.

In silico modeling of daptomycin provides a pathway for drug design. Experimental determination of ligands is a tedious process requiring time and increases ethical concerns in case animal models are used. In silico modeling predicts pharmaceutical properties of compounds based on their structures and hence reduces animal and reagent use [11]. For this study, ligands of daptomycin were identified, and molecular docking of the lipopeptides with their ligands was performed. This can be used as a tool to identify new drugs with high efficacy and minimal animal use.

7.2 Methodology

The method for molecular docking with its lipopeptides is as mentioned by Jujjavarapu et al. [12]. The ligands of daptomycin were obtained from RCSB database. The three-dimensional structure of daptomycin was acquired from Protein Data Bank with 1T5N as PDB ID. This PDB file was uploaded on Maestro interface of Schrödinger software, and the protein preparation was performed by eliminating any molecules of water in the protein and minimizing the energy of molecule. The structure of each of the ligands was drawn in Maestro suite of Schrödinger using 2D Sketcher tool. LigPrep tool was used to prepare ligands similar to protein preparation. After the preparation of lipopeptide (receptor) and ligands, SiteMap function was used to define the docking sites in daptomycin. Glide function in Maestro interface was employed to study the affinity of daptomycin with its ligands.

7.3 Results

The various ligands of daptomycin as recognized by RCSB database are D-alanine, decanoic acid, D-asparagine, D-serine, (2S)-2-amino-4-(2-aminophenyl)-4-oxobutanoic acid, (2S, 3R)-2-azanyl-3-methyl-pentanedioic acid, and L-ornithine. Among these ligands, D-asparagine interacted with the target daptomycin via five hydrogen bonds along with some weak interactions. The interaction of D-asparagine is via the following amino acids, ASP10, LME13, GLY11, DSN12, and ORN7, as shown by the ligand interaction diagram in Fig. 7.1.

The yellow dotted lines in Fig. 7.1a show the hydrogen bonds formed between the ligands and daptomycin. The red lines symbolize oxygen atoms, whereas blue lines depict nitrogen atoms. Hydrogen atoms and carbon skeleton are depicted by white and gray lines, respectively. Figure 7.1b shows ligand interaction diagram

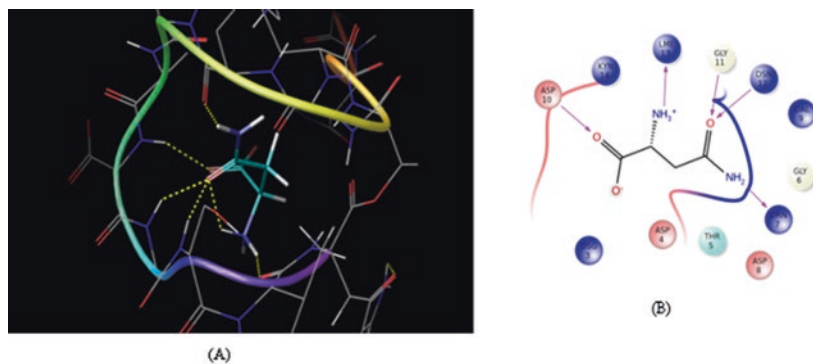


Fig. 7.1 (a) Interaction of daptomycin with D-asparagine (b) Ligand interaction diagram of daptomycin and D-asparagine

between the ligands and daptomycin. Here, hydrogen bond interaction between D-asparagine and daptomycin back bone is represented by purple solid lines. Docking score signifies the interaction of daptomycin and its ligands quantitatively. On the other hand, release of free energy due to interaction of ligand with target is measured as glide energy. The above interaction has lowest docking score of -6.068 with glide energy of -22.56 kcal/mol.

D-alanine interacted with daptomycin via four hydrogen bonds and other weak bonds. The interaction of D-alanine was with the following amino acids of daptomycin, GLY11, DSN12, LME13, and ASP10, as shown in the ligand interaction diagram in Fig. 7.2. The interaction showed the lowest docking score of -3.229 with glide energy of -13.678 kcal/mol. The interaction of D-serine with daptomycin was via four hydrogen bonds with amino acids DSG3, TRP2, and ASP4 of daptomycin as shown in the ligand interaction diagram in Fig. 7.3. This interaction yielded the

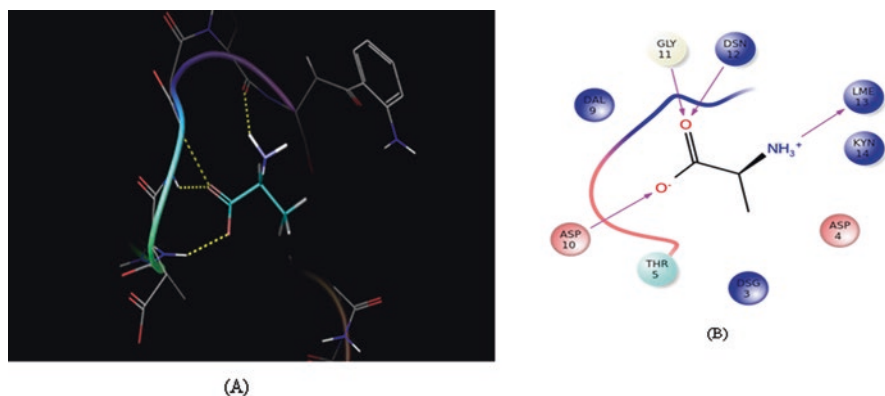


Fig. 7.2 (a) Interaction of daptomycin with D-alanine (b) Ligand interaction diagram of daptomycin and D-alanine

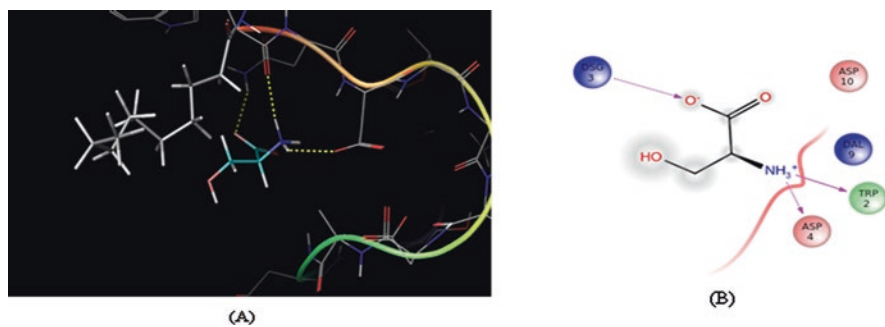


Fig. 7.3 (a) Interaction of daptomycin with D-serine (b) Ligand interaction diagram of daptomycin and D-serine

Table 7.1 Docking outcome of daptomycin with its ligands

Ligand	Docking	Docking score	Glide energy (kcal/mol)
D-alanine	Yes	-3.229	-13.678
Decanoic acid	No	-	-
D-asparagine	Yes	-6.068	-22.56
D-serine	Yes	-4.216	-12.042
(2s)-2-amino-4-(2-aminophenyl)-4-oxobutanoic acid	No	-	-
(2r,3r)-2-azanyl-3-methyl-pentanedioic acid	No	-	-

lowest docking score of -4.216 with glide energy of -12.042 kcal/mol as mentioned in Table 7.1

Three ligands, decanoic acid, (2S)-2-amino-4-(2-aminophenyl)-4-oxobutanoic acid, and (2R,3R)-2-azanyl-3-methyl-pentanedioic acid, did not show any interaction with the lipopeptide daptomycin due to the lack of any docking site for the above-mentioned ligands.

7.4 Discussion

The 3D scaffold of the protein and ligand directs the complex between protein and its ligand along with hydrogen bonds and the hydrophobic sites on the binding region of protein. The knowledge of this interaction will be helpful in synthesizing and designing drug molecules. Structure-based drug design uses structural knowledge of protein's three-dimensional structure or the sequence of amino acids of target protein to design drugs. The current study deals with the structure-based drug design of daptomycin as its structure is already reported in PDB.

Lipopeptides act as antibacterial drugs. Many studies have demonstrated the ability of structure-based drug design as potential anti-bacterial drugs. These studies have shown the increased detection of anti-bacterial drug and its applications for the generation of novel antimicrobial drugs using structure-based drug design [13]. The combinatorial synthesis for the production of novel lipopeptides with antimicrobial activity was investigated by Liu et al. [14].

Due to their potent antimicrobial activity and complex structure, rational drug design has been established on the synthesis pathways of lipopeptides. This can lead to development and optimization of novel drug molecules for pharmaceutical and medical applications [14]. The structure of plipastatin was generated by various domains of the biosynthetic complex of plipastatin. This led to the generation of novel lipopeptides with significant antimicrobial ability [15]. An *in silico* approach for the application of a lipopeptide, surfactin, as a medication of Alzheimer's disease and as an antimicrobial and anticancer agent [12, 16, 17], has been demonstrated in previous studies. Even though daptomycin is currently being used to treat Gram-positive infections under the trade name Cubicin [18], its knowledge on the aspects of structure-based drug design is not available.

In this study, structure-based drug design for daptomycin was performed using Schrödinger software. Three out of six identified ligands were found to interact with daptomycin with docking scores of -3.229 (for D-alanine), -6.068 (for D-asparagine), and -4.216 (for D-serine). Their respective glide energies were -13.678 kcal/mol (D-alanine), -22.56 kcal/mol (D-asparagine), and -12.042 kcal/mol (D-serine). Knowledge of these interactions can help us in determining the binding sites and efficacies of lipopeptides which can be used as antimicrobial drugs.

Acknowledgments We are thankful to the National Institute of Technology Raipur and Chhattisgarh Council of Science and Technology (CCOST) (Project number 2487/CCOST/ MRP/2016, Raipur dated 25.01.2016), India, for providing the necessary facilities to prepare the manuscript and permission to publish it.

Similarity Index The similarity index was checked using Turnitin software and was observed to be less than 10%.

References

1. Michael CA, Dominey-Howes D, Labbate M (2014) The antimicrobial resistance crisis: causes, consequences, and management. *Front Public Health* 2. <https://doi.org/10.3389/fpubh.2014.00145>
2. Lee SY, Fan HW, Kuti JL, Nicolau DP (2006) Update on daptomycin: the first approved lipopeptide antibiotic. *Expert Opin Pharmacother* 7(10):1381–1397
3. Ventola CL (2015) The antibiotic resistance crisis: part 1: causes and threats. *Pharm Ther* 40(4):277
4. Straus SK, Hancock RE (2006) Mode of action of the new antibiotic for Gram-positive pathogens daptomycin: comparison with cationic antimicrobial peptides and lipopeptides. *Biochim Biophys Acta (BBA)-Biomembr* 1758(9):1215–1223
5. Pálffy R, Gardlik R, Behuliak M, Kadasi L, Turna J, Celec P (2009) On the physiology and pathophysiology of antimicrobial peptides. *Mol Med* 15(1–2):51–59
6. Rotem S, Mor A (2009) Antimicrobial peptide mimics for improved therapeutic properties. *Biochim Biophys Acta (BBA)-Biomembr* 1788(8):1582–1592
7. Cotter C, Sturrock HJW, Hsiang MS, Liu J, Philips AA, Hwang J, Gueye CS, Fullman N, Gosling RD, Feachem RGA (2013) The changing epidemiology of malaria elimination: new strategies for new challenges. *Lancet* 382(9895):900–911
8. Mandal SM, Barbosa AEAD, Franco OL (2013) Lipopeptides in microbial infection control: scope and reality for industry. *Biotechnol Adv* 31(2):338–345
9. Rosenberg E, Ron E (1999) High- and low-molecular-mass microbial surfactants. *Appl Microbiol Biotechnol* 52(2):154–162
10. Schneider T, Müller A, Miess H, Gross H (2014) Cyclic lipopeptides as antibacterial agents—potent antibiotic activity mediated by intriguing mode of actions. *Int J Med Microbiol* 304(1):37–43
11. Ekins S, Mestres J, Testa B (2007) In silico pharmacology for drug discovery: applications to targets and beyond. *Br J Pharmacol* 152(1):21–37
12. Jujavarapu SE, Dhagat S (2018) In silico discovery of novel ligands for antimicrobial lipopeptides for computer-aided drug design. *Probiol Antimicrob Proteins* 10(2):129–141
13. Simmons KJ, Chopra I, Fishwick CW (2010) Structure-based discovery of antibacterial drugs. *Nat Rev Microbiol* 8(7):501–510

14. Liu H, Gao L, Han J, Ma Z, Lu Z, Dai C, Zhang C, Bie X (2016) Biocombinatorial synthesis of novel lipopeptides by COM domain-mediated reprogramming of the plipastatin NRPS complex. *Front Microbiol* 7:1801
15. Verma A, Kumar A, Debnath M (2016) Molecular docking and simulation studies to give insight of surfactin amyloid interaction for destabilizing Alzheimer's A β 42 protofibrils. *Med Chem Res* 25:1616–1622
16. Eswari JS, Dhagat S, Yadav M (2019) Antifungal lipopeptides. In: *Computer-aided design of antimicrobial lipopeptides as prospective drug candidates*. CRC Press, Boca Raton, pp 95–102
17. Jujjavarapu SE, Dhagat S, Kurrey V (2018) Identification of novel ligands for therapeutic lipopeptides: daptomycin, surfactin and polymyxin. *Curr Drug Targets* 19(13):1589–1598
18. Steenbergen JN, Alder J, Thorne GM, Francis PT (2005) Daptomycin: a lipopeptide antibiotic for the treatment of serious Gram-positive infections. *J Antimicrob Chemother* 55(3):283–288



Design and Simulation of Geometrical Shape and Size Variations of Micro-electrode for Cochlear Implant

8

Abhishek Nigam, Faiz Ahmed, and S. J. Pawar

Abstract

The microelectrode array of the cochlear implant (CI) is an important component which performs a key function in restoring the hearing process. In this study, different design possibilities for CI electrode have been explored by modelling and simulation of electrode of shapes and sizes in COMSOL Multiphysics 5.0. The effect of electric field density (EFD) distribution due to single electrode inside the fluidic environment of cochlea has been studied and evaluated. Similarly, the electric potential (EP) on the surface of electrode has also been investigated. It is found that the electric field has uniformly distributed and the value of electric field increases with increase of electrode size. There is a significant increment in the EP around the electrode and a developed potential is high enough to trigger an action potential at the nerve (hair cell) when the height of electrodes is increased.

Keywords

Cochlear implant · Electrode · Electric field density · Electric potential · Simulation

A. Nigam

Past PG Student and Current PhD Scholar, Department of Applied Mechanics, Motilal Nehru National Institute of Technology Allahabad, Prayagraj, India

F. Ahmed

Past PG Student, Department of Applied Mechanics, Motilal Nehru National Institute of Technology Allahabad, Prayagraj, India

S. J. Pawar (✉)

Professor, Department of Applied Mechanics, Motilal Nehru National Institute of Technology Allahabad, Prayagraj, India

e-mail: sjpawar@mnnit.ac.in

8.1 Introduction

Cochlear implant (CI) is the most effective transplantable prosthetic device with respect to performance and demand which can bypass the inoperative inner ear by directly invigorating the auditory nerve with electric current, thus empowering the deaf people to experience sound again. In the spiral cochlea, the low-frequency sound is towards the apical contact and high-frequency sound is towards the base. This functioning is mimicked in the CI by the spread of stimulation current to respective electrode [1]. Microelectrode array of CI performs the task of restoring the hearing process to the patients [2]. A low-cost prototype of CI has been designed and developed from commercial off-the-shelf components [3]. A number of CIs have been designed with slightly different specific characteristics, but all the devices share the common features like an ear-level microphone pick up, amplifies, and converts the speech sound into an electrical signal [4]. The flexible long straight electrode array which permit deep insertion with little or no insertion trauma is developed for speech understanding in noise and to enhance sound quality by providing a more natural impression [5]. This chapter investigates and explores the design (variation in shape and size) possibilities for improvement in the physical and electrical properties of CI electrode using COMSOL Multiphysics® 5.0.

8.2 Electrode Design and Simulation

Electrode arrangement consists of silicon substrate having Titanium Nitride (TiN) electrode. The Parylene that has been used as a protective conformal coating and fluidic cochlea environment was mimicked by Perilymph (Fig. 8.1). The material

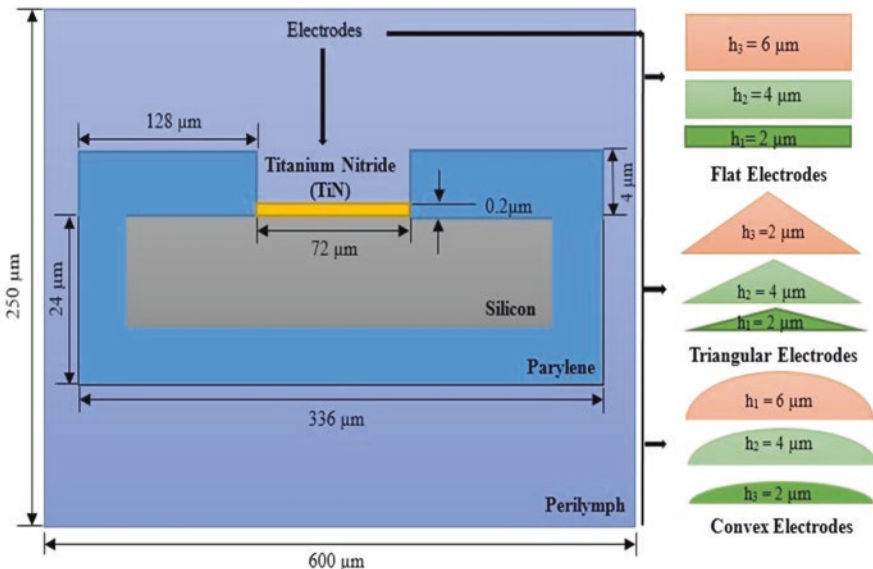


Fig. 8.1 A schematic diagram of CI with different electrodes (flat, triangular and convex shapes)

Table 8.1 Material properties considered for simulation [1]

Materials	Electrical conductivity, sigma (S/m)	Relative permittivity (ϵ_r)
Silicon	4.3 e-4	11.7
Titanium Nitride	5000	100
Perilymph (fluid in cochlea)	2	50
Parylene	5 e-20	2.2

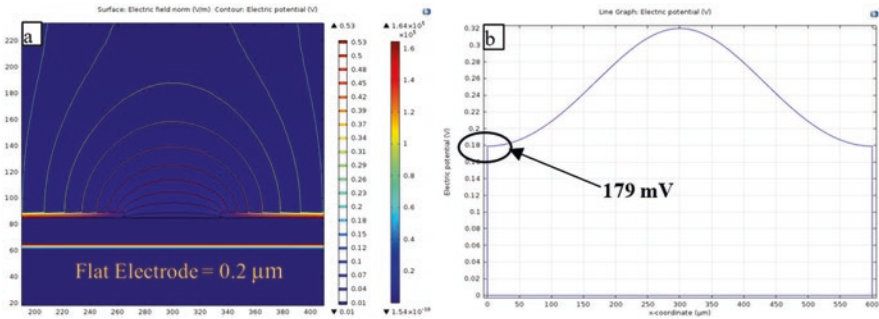


Fig. 8.2 EFD and EP for flat-shaped electrodes ($h = 0.2 \mu\text{m}$) (a) Contour plot and (b) 1-D plot

properties are listed in Table 8.1. Totally three shapes (flat, triangular and convex) of electrodes with three distinct heights ($2.2 \mu\text{m}$, $4.2 \mu\text{m}$ and $6.2 \mu\text{m}$) were studied along with $0.2 \mu\text{m}$ electrode as a reference with 2-D electrode geometry using COMSOL Multiphysics® 5.0 to observe electric field density (EFD) distribution and electric potential (EP).

In this study, the fluidic environment was created as an area of $600 \times 250 \mu\text{m}$ filled with Perilymph and encapsulating Parylene-coated silicon substrate holding TiN electrode. The AC/DC module of the COMSOL was used to simulate the model. The standard properties for this module are current conservation (all domains), electric insulation (all boundaries, except the bottom line), and initial values (all domains). The EP was given to the top boundary of electrode and the ground was given to the bottom boundary of the Perilymph. All the components were initialized as 0 V, except the top surface of an electrode which has the potential of 544 mV [1]. A free triangular mesh was used (maximum element size of $40.2 \mu\text{m}$ and minimum of $0.005 \mu\text{m}$). The growth rate, curvature resolution and the narrow region resolution was taken as 1.2, 0.3 and 1, respectively.

8.3 Result and Discussion

EFD at the surface and the contour lines of EP for the flat-shaped reference electrode ($h = 0.2 \mu\text{m}$) is shown in Fig. 8.2a. The 1-D plot of EP is shown in Fig. 8.2b. Contour lines are symmetric about the centre of the electrode. The eighth contour line is at the position nearly about $187 \mu\text{m}$. The EP distribution on the top surface of electrode is

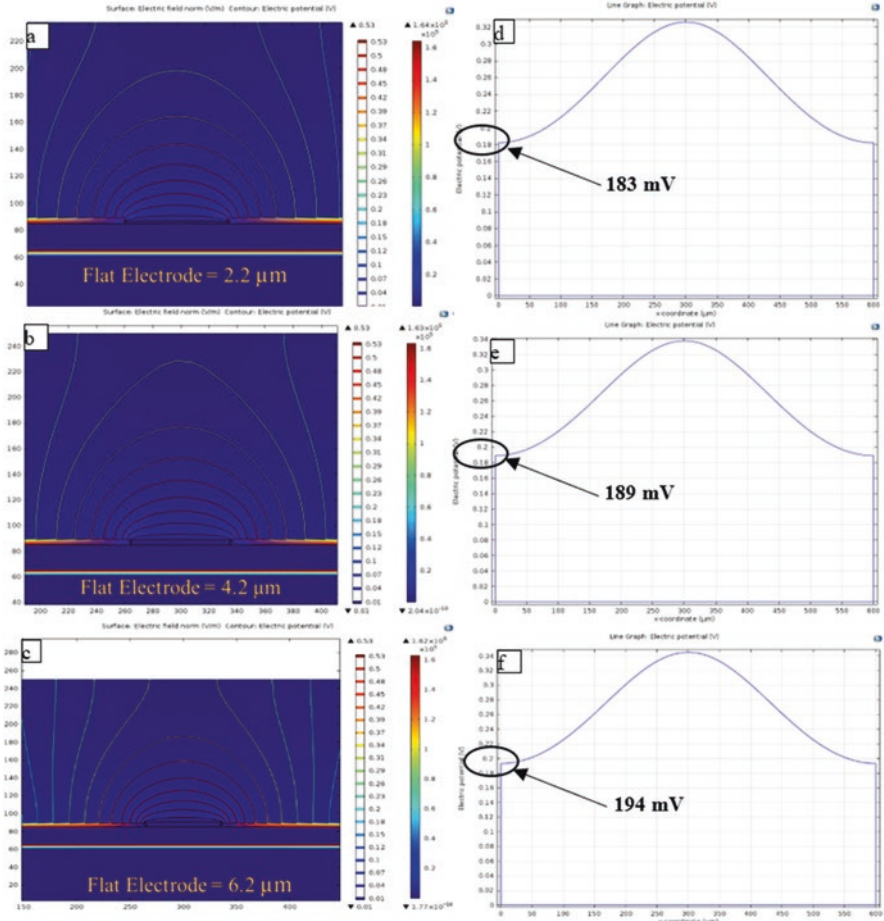


Fig. 8.3 EFD for flat-shaped electrode (a) $h = 2.2 \mu\text{m}$, (b) $h = 4.2 \mu\text{m}$, and (c) $h = 6.2 \mu\text{m}$, and EP for flat-shaped electrode contour plot (d) $h = 2.2 \mu\text{m}$, (e) $h = 4.2 \mu\text{m}$, and (f) $h = 6.2 \mu\text{m}$

bell shaped and is symmetric about the centre. The values of EP are 320 mV (maximum) at the centre and 179 mV at the extreme ends. The modification in the shape of electrode and its effect on the result is discussed below. The flat-shaped electrodes ($h = 2.2 \mu\text{m}$, $4.2 \mu\text{m}$ and $6.2 \mu\text{m}$) are shown in Fig. 8.3a–f. For $2.2 \mu\text{m}$ electrode, the eighth contour line’s peak is nearly at $200 \mu\text{m}$ (Fig. 8.3a), while for $0.2 \mu\text{m}$, the peak of eighth contour line is at $187 \mu\text{m}$. It is clearly observed that on increasing the height of electrode, the EFD peak intensity is increasing (Fig. 8.3a–c). The EP at the surface is increasing as the height of electrode increases (Fig. 8.3d–f). The EP at the ends of electrode ($0.2 \mu\text{m}$) is 180 mV, which is now increased to 183 mV, 189 mV and 194 mV for $2.2 \mu\text{m}$, $4.2 \mu\text{m}$ and $6.2 \mu\text{m}$ electrodes, respectively. The peak of EP has also increased to nearly 327 mV, 338 mV and 345 mV

for 2.2 μm , 4.2 μm and 6.2 μm electrodes, respectively as compared to 320 mV for 0.2 μm electrode.

The simulation result of triangular electrodes ($h = 2.2 \mu\text{m}$, 4.2 μm and 6.2 μm) shows that the contour lines of EFD are symmetrically distributed at both the ends of electrode and at the surface of electrode which is shown in Fig. 8.4a–c. The height of electrodes varies as peak intensity of eighth contour line increases from 190 μm to 205 μm (approximately). The peak value of EP also increases as 323 mV, 325 mV and 327 mV which is clearly shown in Fig. 8.4d–f. The EP at both ends of electrodes increases accordingly as 180 mV to 182 mV and 183 mV, respectively for electrodes ($h = 2.2 \mu\text{m}$, 4.2 μm and 6.2 μm).

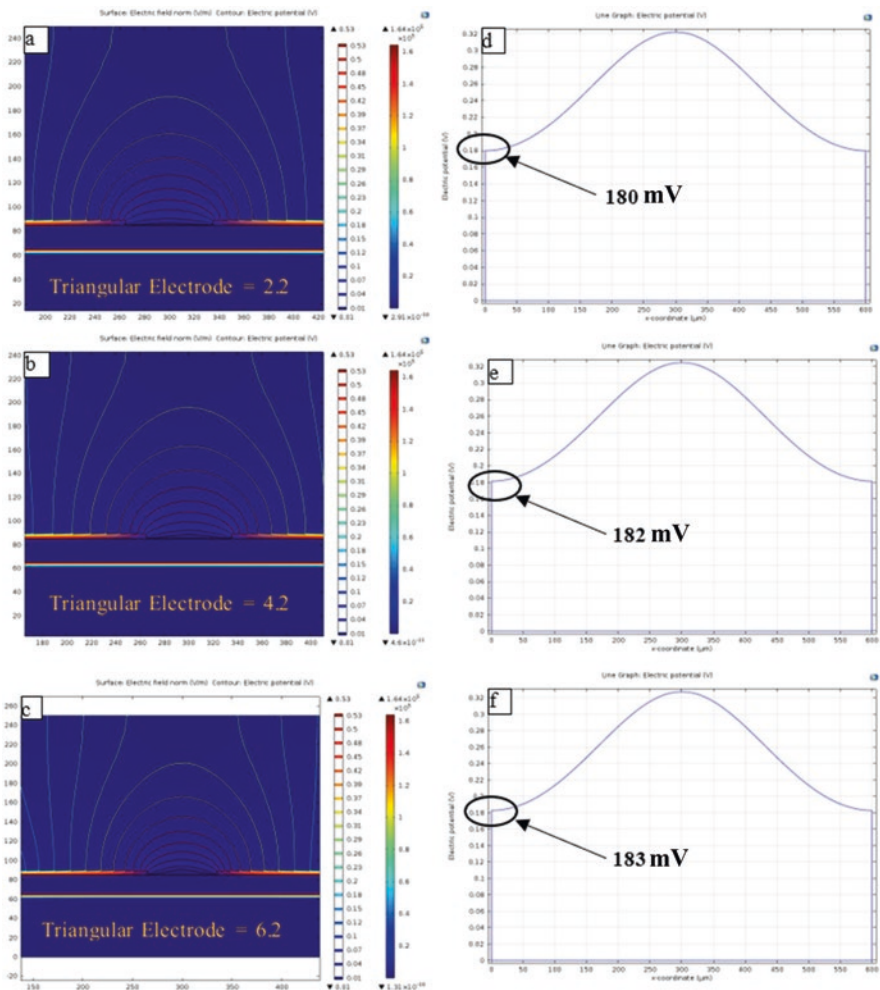


Fig. 8.4 EFD for triangular-shaped electrode (a) $h = 2.2 \mu\text{m}$, (b) $h = 4.2 \mu\text{m}$, and (c) $h = 6.2 \mu\text{m}$, and EP for triangular-shaped electrode contour plot (d) $h = 2.2 \mu\text{m}$, (e) $h = 4.2 \mu\text{m}$, and (f) $h = 6.2 \mu\text{m}$

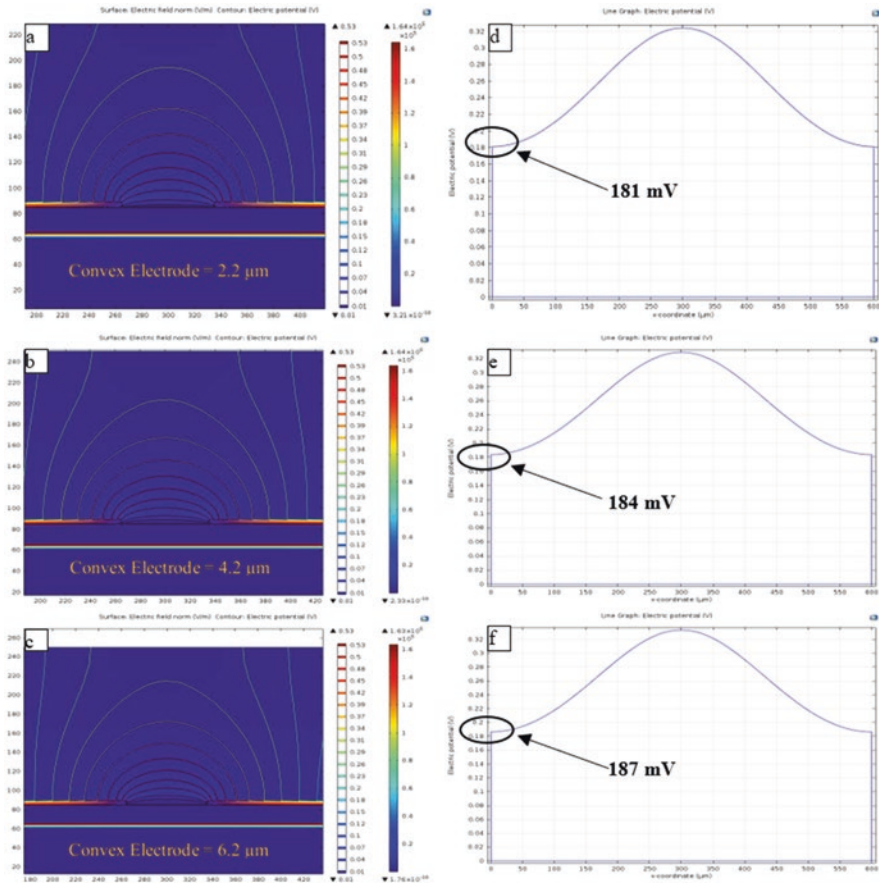


Fig. 8.5 EFD for convex-shaped electrode (a) $h = 2.2 \mu\text{m}$, (b) $h = 4.2 \mu\text{m}$, and (c) $h = 6.2 \mu\text{m}$, and EP for convex-shaped electrode contour plot (d) $h = 2.2 \mu\text{m}$, (e) $h = 4.2 \mu\text{m}$, and (f) $h = 6.2 \mu\text{m}$

The result of convex-shaped electrodes ($h = 2.2 \mu\text{m}$, $h = 4.2 \mu\text{m}$ and $h = 6.2 \mu\text{m}$) shows that the contour lines peak values are increasing from position $190 \mu\text{m}$ to $215 \mu\text{m}$ with the increase of height of electrode as shown in Fig. 8.5a–c. The EP is well distributed along the surface as a bell-shaped structure and is symmetric about the centre of electrode. The EP for these electrodes is increasing as 324 mV , 329 mV and 334 mV as shown in Fig. 8.5d–f. The EP at the ends of electrodes has been increased accordingly and is labelled in the Fig. 8.5d–f.

Among three modifications, the flat type electrodes have shown the maximum EFD and EP. The variation in the EP is minimum in case of triangular electrodes, whereas the flat type electrodes have shown maximum variation in EP with respect to variation in height of electrodes. It is also found that in all three modifications, the bell-shaped EP and the distribution of EFD have shown symmetry about the center of each electrodes.

8.4 Conclusion

The results show that the EFD and EP for the three variants are symmetrically distributed about the centre of electrodes. The EP at the surface and at ends of the electrode increases with the increase in height of electrode from 2.2 μm to 6.2 μm . Among three different shapes of the electrodes, flat-shaped electrodes give the maximum output at the surface. The electrode height above Parylene (4 μm) in the case of convex electrode has the significant increase (187 mV for 6.2 μm). The variation in EP with respect to change in height of electrode is maximum in case of flat electrodes and minimum in case of triangular electrodes. The EFD and EP are confined to the intended position of the cochlea. Finally, the approach presented in this study can be considered towards the development of micro-electrode array for more complex CI by using these modifications for research and experiments in laboratory.

References

1. Lawand NS et al (2011) Development of probes for cochlear implants. In: Proceedings of IEEE sensors, pp 1827–1830
2. Lawand NS, Van Driel J, French PJ (2012) Electric field density distribution for cochlear implant electrodes. 2012 COMSOL conference proceedings, pp 1–4
3. Ali H et al (2009) Laboratory prototype of cochlear implant: design and techniques. In 31st annual international conference of the IEEE Engineering in Medicine and Biology Society, pp 803–806
4. Tognola G et al (2005) Measurement of electrode current pulses from cochlear implants. IEEE Trans Instrum Meas 54(5):2105–2112
5. Hochmair I et al (2015) Deep electrode insertion and sound coding in cochlear implants. Hear Res 322:14–23



Molecular and Protein Interaction Studies for Inhibiting Growth of Human Leukemic Cells: An In Silico Structural Approach to Instigate Drug Discovery

Arundhati Banerjee, Rakhi Dasgupta, and Sujay Ray

Abstract

Leukemia inhibitory factor (LIF) stimulates the terminal differentiation of the cells of myelogenous leukemia by interacting with gp130 (dimeric) and LIF receptor (LIFR). Janus protein-tyrosine kinases (JAK) and STAT3 get triggered by phosphorylation. This leads to target gene expression and thus inhibition of the growth of leukemic cells occurs. Wet-laboratory experimental studies were involved so far, but the residue-based molecular-level indulgence and structural changes in the protein complexes were not explored hitherto. This study therefore involves X-ray crystal structures of the three proteins. Through molecular docking techniques, the best cluster-sized complex was selected and optimized. Electrostatic surface potential for gp130 protein, net solvent accessibility and an ascent in the ΔG value from -2101.57 kcal/mol to -2124.28 kcal/mol showed spontaneous and firmer interaction after optimization. Conformational fluctuations in gp130 had a shift for increased β -sheet conformation to stabilize the complex. All evaluations were statistically significant. Protein interaction residues and binding patterns revealed that ionic interactions were the predominant ones with Asp and Arg playing chief role. After optimization, even ionic interactions increased to 11. Other interactions including hydrogen bonding ones were also seen. Thus, it might instigate the clinical and pharmaceutical research for drug discovery and to study the mutational impacts upon interaction.

A. Banerjee · R. Dasgupta
Department of Biochemistry and Biophysics, University of Kalyani,
Kalyani, West Bengal, India

S. Ray (✉)
Amity Institute of Biotechnology, Amity University, Kolkata, West Bengal, India

Keywords

Inhibition to Leukemia · Crystallographic structures · Protein interactions · Biostatistics

9.1 Introduction

Leukemia inhibitory factor (LIF) as its name suggests is the capability to stimulate differentiation of the myeloid leukemic cells leading to their apoptosis [1]. The LIF signal transduction complex comprises two receptor molecules: gp130 (dimeric form) and LIF receptor (LIFR) [2]. After the trio-interaction, Janus protein-tyrosine kinases (JAK) are then induced by trans- and auto-phosphorylation [3]. This stimulates STAT3 tyrosine phosphorylation, fronting to the respective gene expression and thereby apoptosis of the leukemic cells [3]. So far, wet laboratory protein–protein assays and other experimental studies for the cellular transduction mechanism [2–4] were explored but the molecular and structural basis of the interaction remains unexplored, without which effective drug targeting and discovery remains a risk.

Therefore, this study aims to focus upon the detailed structural and molecular-level investigations for hindering the growth of the leukemic cells. Predominantly, gp130 plays a central role for many such interactions among which this study is one of the most focusing. The experimentally validated crystal protein structures were taken into consideration. After docking the three proteins sequentially, the best clustered-size protein complex was energy optimized to bring it near its native stable conformation. Protein–protein interaction residues and binding patterns were explored into further to compare the pre- and post-optimized protein complexes. Electrostatic surface potential, net solvent accessibility and thermodynamic stability of gp130 to interact with these proteins were studied, in details. Conformational fluctuations were further analysed to study the structural shift upon interactions. All the evaluations underwent T-test for statistical significance. Therefore, the study would instigate effectively to foresee the mutational impacts through residual disclosure. It would also serve to analyse the zones of drug discovery in the clinical and pharmaceutical research.

9.2 Materials and Methods

9.2.1 Structural Analysis of Human Gp130, LIF and LIFR

Crystal structures of human gp130, LIF and LIFR were retrieved from Protein Data Bank [5]. The complex structure of gp130 and LIF protein had PDB ID: 1PVH. In the complex structure, gp130 had chain A [6] and chain C [6]. The sequence length of A and C chain was 201 residues each. On the other hand, the LIF protein had B and D chains with 169 residues for each chain. The other 3D structure, LIFR domain was extracted from PDB having PDB ID: 3E0G, chain A [7] with 483 residues. The Discovery Studio Accelrys 4.1 was used for further processing of the structures.

9.2.2 Molecular Docking for the formation of Trio-Complex

The proteins were docked using Cluspro 2.0 web server [8]. The gp130-LIF complex was docked with the LIFR protein to form the trio protein complex. LIFR protein being longer was taken as the receptor protein and gp130-LIF complex was taken as the ligand. Among 10 docked structures, the best cluster-sized protein complex was selected for further study. Using the advanced option of structure modification from Cluspro2.0, the misappropriate residues from the respective proteins were removed. Z-DOCK [9] and GRAMM-X [10] helped to get consensus outcomes for the entire docking phenomena.

9.2.3 Protein Structure Refinement and Energy Optimization Using ModRefiner

Optimization of energy and protein structure refinement for the entire protein complex was executed through the usage of ModRefiner [11]. This leads to provide a stable and accurate protein conformation by correcting the unstable geometries through the performance of high resolution algorithm [11].

Moreover, energy optimization was finally carried out by first, steepest descent and then followed by conjugate gradient (using GROMACS [12]) until the final RMS gradient 0.0001 was attained.

9.2.4 Protein-Protein Interaction Calculations

To calculate the binding pattern and interacting residues among the trio protein complexes, Protein Interaction Calculator (P.I.C.) [13] was operated. Hydrogen bonding as well as other interaction patterns were also calculated; PyMOL [14] and interaction studies from Accelrys Discovery Studio4.1 helped to validate the outcomes.

9.2.5 Evaluation of Thermodynamic Stability, Electrostatic Potential and Net Area of Solvent Accessibility

ΔG value of human gp130 protein was evaluated and compared before and after optimization. DFire [15] energy was evaluated to examine the non-bonded atomic interaction. Upon the protein surface of gp130, electrostatic potential was calculated using PyMOL [14] through vacuum electrostatics. The net solvent accessibility area for human gp130 was calculated after LIF interaction and LIF-LIFR interaction after optimization [16].

9.2.6 Conformational Fluctuations in Human Gp130 Protein

The conformational fluctuations in gp130 before interaction and after two stages of interaction (LIF and LIFR) were calculated and compared through the operation of DSSP [17] and Discovery Studio packages from Accelrys. Previous investigation suggests that proteins having more β -sheets and pure α -helical structures along with 3_{10} helices show firmer interaction and stable conformation [17, 18].

9.2.7 Rationalization of Data from Statistical Significances

All the evaluations were corroborated through statistical calculations. P-value of less than 0.05 or 5% shows the calculated outcomes to be statistically significant from the T-test.

9.3 Results

9.3.1 Structural Demonstration of Human Gp130, LIF and LIFR

Tertiary structure of the dimeric form of human gp130 was found to be 201 residues each. The protein comprises 13 sheets and 2 helices joined by coils. It starts with Gly1 in the coil region. LIF protein comprises 5 sets of helices joined by coils. Total number of residues in LIF is 169. LIFR protein was found to be 483 residues long comprising 27 sheets and one small helical region interspersed by coils. The diagrammatic representation of the proteins has been shown in their interacted state in Fig. 9.1.

9.3.2 Protein–Protein Interaction Residues and Binding Pattern

For analysing the residual involvement of the three proteins, nine strong ionic–ionic interactions were seen to get increased to 11 ionic interactions after minimization and optimization of the complex (Table 9.1 and Fig. 9.1). Apart from ionic interaction, hydrogen bonding interactions were also involved in the interaction pattern.

9.3.3 Comparison of Thermodynamic Stability, Electrostatic Potential and Net Solvent Accessibility

The ΔG value was found to get increased from -2101.57 kcal/mol to -2124.28 kcal/mol (Table 9.2). Therefore, it implies a spontaneous and firmer interaction to be formed between the trio protein complex. Moreover, the change in the vacuum electrostatic potential was observed to have a change from ± 57.115 to ± 58.229 (Fig. 9.2).

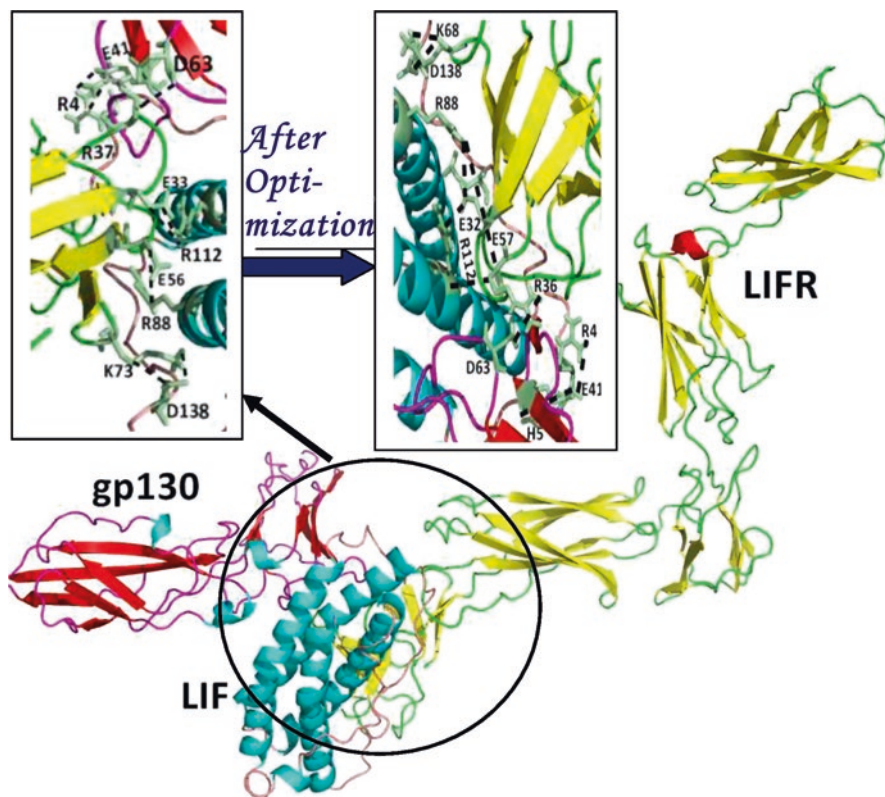


Fig. 9.1 Structural demonstration and few interacting residues in the trio-complex. The residues and bonds are represented in black sticks and black dashes, respectively

From Fig. 9.2, the shift in the electrostatic potential values upon gp130 in the interacted state pre- and post-optimization gets illustrated.

Additionally, the decrease in the net surface area for solvent accessibility for the trio complex also depicts the stronger and firmer interaction after optimization (Table 9.2).

9.3.4 Conformational Fluctuations

The conformational fluctuation in gp130 protein was observed before and after optimization in the interactive stage (trio complex). The gp130 protein was observed to have an ascent in the percentage of β -sheets accompanied by zilch decrease in the percentage of coils keeping the percentage of pure helices and 3_{10} helices same (Fig. 9.3). The overall provides a stable and firmer conformation for the protein to interact well and thereby inhibit the leukemic cells efficiently.

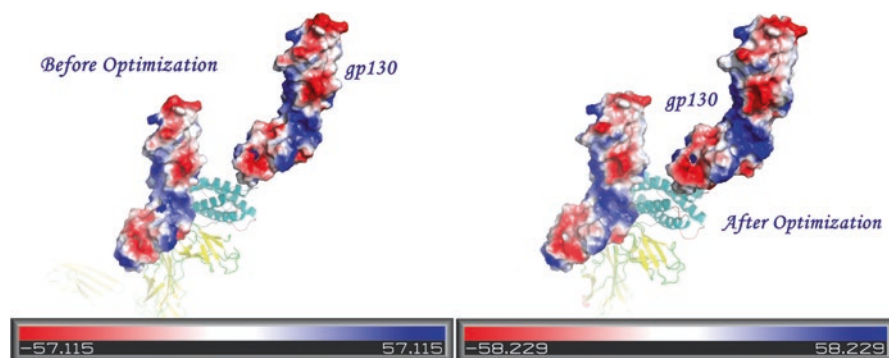
Table 9.1 Ionic interactions before optimization (left) and after optimization (right)

Position	Residue	Protein	Position	Residue	Protein	Position	Residue	Protein	Position	Residue	Protein
41	GLU	C	4	ARG	L	41	GLU	C	4	ARG	L
63	ASP	C	37	ARG	R	41	GLU	C	5	HIS	L
73	GLU	C	5	HIS	L	63	ASP	C	36	ARG	R
88	ARG	L	58	GLU	R	73	GLU	C	5	HIS	L
89	ASP	L	73	LYS	R	88	ARG	L	32	GLU	R
109	ASP	L	35	ARG	R	88	ARG	L	57	GLU	R
112	ARG	L	33	GLU	R	89	ASP	L	68	LYS	R
112	ARG	L	58	GLU	R	109	ASP	L	34	ARG	R
138	ASP	L	73	LYS	R	112	ARG	L	32	GLU	R
						112	ARG	L	57	GLU	R
						138	ASP	L	68	LYS	R

Chain C represents gp130 while L and R represent LIF and LIFR proteins, respectively

Table 9.2 Stability parameters for the entire trio complex before and after optimization

Stability parameters	Pre-optimization	Post-optimization
Dfire energy (kcal/Mol)	-2101.57	-2124.28
Net ASA (sq. Å)	48148.72	47165.17

**Fig. 9.2** The electrostatic surface potential upon gp130 in its interacted state

9.3.5 Statistical Significant Outcomes

The evaluated values from the stability parameters and the conformational fluctuations were observed to be statistically significant with a P-value of 0.020101 and 0.032183, respectively. Thus, this corroborates the outcomes.

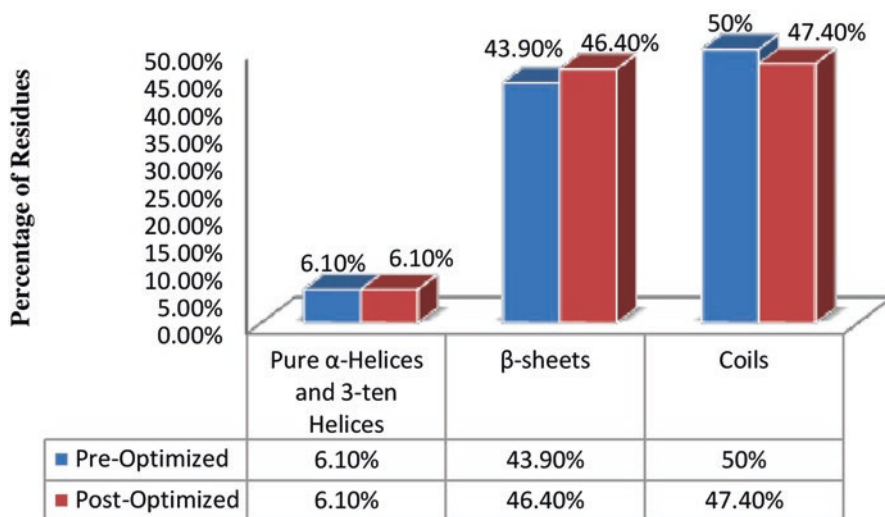


Fig. 9.3 Conformational fluctuations in gp130

9.4 Discussion and Future Scope

Leukemia is one of the most lethal and widespread diseases in today's world. In humans, LIF after interacting with gp130 and LIFR participates in a predominant role to cause apoptosis to the leukemic cells. Therefore, a trio complex is formed which leads to the apoptosis of the leukemic cells. Previously, though several wet laboratory experiments were performed to document their interaction but without molecular-level residual investigation, the effective drug discovery and novel therapeutics cannot be further developed. Additionally, earlier investigations also dealt with the interactions of proteins for breast cancers [19] and many more [20] but leukemia and its inhibition was unexplored with molecular-level studies with a prime focus to the participation of gp130 (as it is known to play a pivotal and central role in many such interactions). So, the present study primarily focuses on the residual participation, 3D crystallographic structural analysis, the detailed conformational fluctuations and thermodynamic stabilities in the proteins to explore the interaction in vivid ways.

After exploring the 3D crystallographic structures of the proteins from *Homo sapiens*, the structures were docked, and the finest structure conformation was opted for further investigations. The complex was well optimized to achieve a steady-firm conformation. The residual disclosures affirm the increased participation of residues from the optimized complex. The predominant ionic interactions were exhibited by mainly Asp and Arg residues from LIF protein with mainly Glu and Lys from LIFR. The C chain of gp130 participated in an active role in the interaction forming three interactions with LIF and one with LIFR. Arg88 and Arg112 from LIF alone formed two ionic interactions with their partner proteins. On the other

hand, Glu41 from gp130 formed two interactions with LIF. Altogether, a pocket-like structure was formed for the charged ionic interactions leading to the accommodation and interaction of the respective proteins, competently. These sites can be further studied as drug targets. Furthermore, the decrease in the ΔG value supports the spontaneous and firmer interaction in the optimized trio complex. Additionally, electrostatic surface potential upon gp130 and net solvent accessibility also depicts a firmer interaction for the aforementioned complex. Conformational fluctuations showed a drastic increase in the β -sheets keeping the percentage of pure helices and 3_{10} helices same, thereby providing a stronger conformational stability after interaction and optimization. These on the whole would lead to proficient interaction, followed by efficient cellular signalling mechanism to cause the activation of JAK-STAT and thus finally apoptosis of the leukemic cells. The outcomes were rationalized through statistical significances too. Therefore, this study poses a lime-light for the advancement in the clinical and pharmaceutical research as well as to instigate explorations with mutational impacts.

Acknowledgement High gratefulness is rendered to the Department of Biochemistry and Biophysics, University of Kalyani, for the support. Authors are also grateful to the Amity Institute of Biotechnology, Amity University, Kolkata, for the cooperation and support as well.

References

1. Blanchard F et al (2000) Stimulation of leukemia inhibitory factor receptor degradation by extracellular signal-regulated kinase. *J Biol Chem* 275:28793–28801
2. Mathieu ME et al (2012) LIF-dependent signaling: new pieces in the lego. *Stem Cell Rev Rep* 8(1):1–15
3. Sun X, Bartos A, Whitsett JA, Dey SK (2013) Uterine deletion of Gp130 or Stat3 shows implantation failure with increased estrogenic responses. *Mol Endocrinol* 27(9):1492–1501
4. Metz S et al (2008) Novel inhibitors for murine and human leukemia inhibitory factor based on fused soluble receptors. *J Biol Chem* 283:5985–5995
5. Berman MH et al (2000) The protein data bank. *Nucleic Acids Res* 28:235–242
6. Boulanger MJ, Bankovich AJ, Kortemme T, Baker D, Garcia KC (2003) Convergent mechanisms for recognition of divergent cytokines by the shared signaling receptor gp130. *Mol Cell* 12:577–589
7. Skiniotis G, Lupardus PJ, Martick M, Walz T, Garcia KC (2008) Structural organization of a full-length gp130/LIF-R cytokine receptor transmembrane complex. *Mol Cell* 31:737–748
8. Comeau SR et al (2004) ClusPro: an automated docking and discrimination method for the prediction of protein complexes. *Bioinformatics* 20:45–50
9. Pierce BG et al (2014) ZDOCK server: interactive docking prediction of protein-protein complexes and symmetric multimers. *Bioinformatics* 30(12):1771–1773
10. Tovchigrechko A, Vakser IA (2006) GRAMM-X public web server for protein-protein docking. *Nucleic Acids Res* 34:W310–W314
11. Xu D, Zhang Y (2011) Improving the physical realism and structural accuracy of protein models by a two-step atomic level energy minimization. *Biophys J* 101:2525–2534
12. Abraham MJ et al (2015) GROMACS: high performance molecular simulations through multi-level parallelism from laptops to supercomputers. *SoftwareX* 1–2:19–25
13. Tina KG, Bhadra R, Srinivasan N (2007) PIC: protein interactions calculator. *Nucleic Acids Res* 35:W473–W476

14. DeLano WL (2002) The PyMOL molecular graphics system. DeLano Scientific, San Carlos
15. Yuedong Y, Yaoqi Z (2008) Specific interactions for ab initio folding of protein terminal regions with secondary structures. *Proteins* 72:793–803
16. Gerstein M (1992) A resolution sensitive procedure for comparing protein surfaces and its application to the comparison of antigen-combining sites. *Acta Crystallogr A* 48:271–276
17. Paul DT, Ken DA (1993) Local and nonlocal interactions in globular proteins and mechanisms of alcohol denaturation. *Protein Sci* 2:2050–2065
18. Toniolo C, Benedetti E (1991) The polypeptide 310-helix. *Trends Biochem Sci* 16:350–353
19. Banerjee A, Ray S (2015) Molecular computing and structural biology for interactions in ER α and bZIP proteins from homo sapiens: an insight into the signal transduction in breast cancer metastasis. *Adv Intell Syst Comput* 404:43–55. https://doi.org/10.1007/978-81-322-2695-6_5
20. Banerjee A, Ray S (2016) Molecular modeling, mutational analysis and conformational switching in IL27: an in silico structural insight towards AIDS research. *Gene* 576(1):72–78



Laccase-Mediated Synthesis of Bio-material Using Agro-residues

10

Komal Agrawal and Pradeep Verma

Abstract

Laccase has the ability to act on a broad range of substrates, as a result of which multiple compounds have been used for laccase assay and numerous applications have been discovered over time. Thus, considering the above points, in the present study, white and blue laccase from *Myrothecium verrucaria* ITCC-8447 and *Pleurotus ostreatus* were used for laccase assay using various substrates which includes 2,2'-azinobis-3-ethylbenzothiazoline-6-sulfonic acid (ABTS), 2,6-dimethoxyphenol (2, 6 DMP), guaiacol (GCL), and syringaldazine (SYZ). The most effective substrate of the four substrates was ABTS for white and blue laccase. The white and blue laccase were further used for the synthesis of bio-material via fungal-assisted treatment of wheat bran (WB) and sugarcane bagasse (SB) followed by micro-wave pre-treatment and the addition of starch and glycerol to the treated agro-residue in the ratio of 5:1:1. The thickness swelling and water absorption percentage was minimum for wheat bran synthesized bio-material using white laccase in comparison to the other synthesized bio-material.

Keyword

ABTS · 2 · 6 DMP · GCL · SYZ · Agro-residue · Bio-material

K. Agrawal · P. Verma (✉)

Department of Microbiology, Central University of Rajasthan, Bandarsindari, Ajmer, Rajasthan, India

e-mail: pradeepverma@curaj.ac.in

© Springer Nature Singapore Pte Ltd. 2020

P. C. Sadhukhan, S. Premi (eds.), *Biotechnological Applications in Human Health*, https://doi.org/10.1007/978-981-15-3453-9_10

87

10.1 Introduction

Laccase is widely distributed in nature and is found in plants, fungi, insects [1], and bacteria [2]. Laccase, due to its substrate specificity, can act on a broad range of substrates, as a result of which various substrates have been used for laccase assay, and the most widely used substrates include ABTS, 2,6 DMP, GCL, and SYZ. The other aspect of the enzyme involves the reuse of agro-residues which are generated in huge amounts throughout the globe. Only a small fraction of these residues is used, and the rest are either dumped in wasteland or are burned, thereby contributing to environmental pollution. They have immense applications, but the lignin content in these agro-residues acts as a barrier for its effective utilization [3]. However, laccase has been used for the delignification of agro-residues [4] which can further help in the utilization of these agro-residues in lignocellulosic biorefinery and synthesis of bio-material. Thus, laccase substrate affinity and its application in various sectors have attracted considerable attention from environmental, industrial, and biotechnological prospect [5].

In the present study, the focus was on two aspects: first is on laccase assay using various substrates, which include 2,2' azinobis-3-ethylbenzothiazoline-6-sulfonic acid (ABTS), 2,6-dimethoxyphenol (2,6 DMP), guaiacol (GCL), and syringaldazine (SYZ) from newly isolated white laccase-producing strain *Myrothecium verrucaria* ITCC-8447 and blue laccase-producing strain *Pleurotus ostreatus* as the reference strain. This was followed by fungal-assisted synthesis of bio-material using wheat bran (WB) and sugarcane bagasse (SB) with white and blue laccase-producing strain *Myrothecium verrucaria* ITCC-8447 and *Pleurotus ostreatus*. The fungal pre-treated substrate was subjected to optimized microwave treatment in our laboratory. The bio-material was synthesized using starch and glycerol. The volume, thickness swelling, and water absorption percentage of the synthesized bio-material were determined. These synthesized bio-materials can help in effectively reutilizing agro-residue which would otherwise be rendered useless, thereby contributing toward management and recycling of agricultural waste.

10.2 Materials and Methods

10.2.1 Materials

The chemicals used were of analytical grades and purchased from Sigma, Hi-Media, and Merck, India.

10.2.2 Culture Condition and Inoculum Preparation

The fungal strain *Myrothecium verrucaria* ITCC-8447 and *Pleurotus ostreatus* were used in this study. The newly isolated strain *Myrothecium verrucaria* ITCC-8447 was isolated from Rajasthan, India, and maintained on malt extract agar plates,

whereas *Pleurotus ostreatus* was a gift culture from the Institute of Forstbotanik, Göttingen, Germany, used as the reference culture and maintained on potato dextrose agar plates. The medium composition used for laccase assay was as follows for *Myrothecium verrucaria* ITCC-8447 (g/L): glucose 5, peptone 5, yeast extract 2, KH_2PO_4 1, MgSO_4 0.5, ZnSO_4 0.01, MnSO_4 0.001, CaCl_2 0.01, FeSO_4 0.01, and pH 7.0 ± 0.5 [6] with slight modifications, and for *Pleurotus ostreatus*, Bushnell Haas Media (BHM) supplemented with (g/L) $\text{C}_6\text{H}_{12}\text{O}_6$ pH 5 ± 0.5 [7] was used for laccase assay. For the inoculum preparation, 7-day-old culture was used, and two 6 mm cubes were inoculated in 50 mL of media using 250 mL Erlenmeyer flask and incubated at 28 ± 2 °C under static condition. The crude enzyme was withdrawn every 48 h for laccase assay, and the experiment was carried out for a period of 12 days. The crude extract from the 10th day was centrifuged at 10,000 rpm for 5 min used for further study.

10.2.3 Enzyme Assay and Protein Concentration Determination

Laccase activity was determined quantitatively by measuring the absorption change of various substrates, which included ABTS at 420 nm, $\epsilon_{420} = 36,000 \text{ M}^{-1} \text{ cm}^{-1}$ [8]; 2,6DMP at 469 nm, $\epsilon_{469} = 14,800 \text{ M}^{-1} \text{ cm}^{-1}$ [9]; GCL at 465 nm, $\epsilon_{465} = 12,100 \text{ M}^{-1} \text{ cm}^{-1}$ [10]; and SYZ at 525 nm, $\epsilon_{525} = 65,000 \text{ M}^{-1} \text{ cm}^{-1}$ [11] for 5 min at 30 °C in UV-visible spectrophotometer (Make: Dynamica; Model: Halo DB-30). The concentration of the substrate was varied and was in the following range: ABTS – 0.5–1.5 mM; 2, 6 DMP, 1–5 mM; GCL, 20–30 mM; and SYZ, 10–30 mM, followed by the determination of the optimal concentration of substrates for laccase assay. The laccase activity was calculated as per Holme and Peck, 1996 [12]. One activity unit (U) was defined as the amount of enzyme required to oxidize 1 mmole ABTS per minute at 420 m, 2,6 DMP at 469 nm, GCL at 465 nm, and SYZ 525 nm. The protein estimation was done by Lowry's method, 1951 [13], with BSA as the standard.

10.2.4 Synthesis of Bio-material Using White and Blue Laccase

The fungal-assisted synthesis of bio-material was done by inoculating the agro-residue WB and SB with *Myrothecium verrucaria* ITCC-8447 and *Pleurotus ostreatus* under SSF for 15 days at 28 ± 2 °C. The agro-residue was then soaked in 5 mM ammonium molybdate, followed by microwave-assisted pre-treatment using microwave reaction system SOLV, Multiwave Pro (Make: Anton Parr, Austria), at 150 °C, 6 lb. pressure for 45 min, as per Verma et al. [14], with slight modifications which were established in our laboratory. It was followed by the addition of starch and glycerol to the treated agro-residue in the ratio of 5:1:1. The bio-material was then synthesized at 140 °C for 30 min. The thickness swelling (%) and water absorption (%) were measured as per Jeefferie et al. [15]:

$$\text{Water absorption} = \left[\frac{W_f - W_i}{W_i} \right] * 100$$

where W_i is the initial weight of bio-material before water absorption and W_f is the final weight of bio-material after water absorption.

$$\text{Thickness swelling} = \left[\frac{T_f - T_i}{T_i} \right] * 100$$

where T_i is the initial thickness of bio-material before water absorption and T_f is the final thickness of bio-material after water absorption.

10.3 Results and Discussions

10.3.1 Laccase Activity Using Various Substrates

Laccase activity was evaluated with different substrates for a period of 12 days using *Myrothecium verrucaria* ITCC-8447 and *Pleurotus ostreatus* (Fig. 10.1a, b). The white laccase activity for *Myrothecium verrucaria* ITCC-8447 was detected 153.3 UL⁻¹ by ABTS, whereas no activity was observed for 2,6 DMP and GCL on the fourth day. However, on the tenth day, white laccase activity using 2,6 DMP and GCL was 2.4 UL⁻¹ and 4.3 UL⁻¹ which was negligible as compared to ABTS 95.8 UL⁻¹. In the reference strain *Pleurotus ostreatus*; significant blue laccase activity was detected on the fourth day with 2,6 DMP and ABTS of 34.9 UL⁻¹ and 16.7 UL⁻¹, respectively, and it was 11.4 UL⁻¹ for GCL, whereas on the tenth day, the laccase activity was 155.7 UL⁻¹, 223.1 UL⁻¹, and 87.4 UL⁻¹ for 2,6 DMP, ABTS, and GCL. The observed difference in laccase activity may be due to the specificity of the crude extract to different substrates.

10.3.2 Laccase Assay Using Various Substrates

The most effective substrate of the four substrates was ABTS for both white and blue laccase from *Myrothecium verrucaria* ITCC-8447 and *Pleurotus ostreatus* (Table 10.1). Multiple substrates were used for laccase assay in the work done by Eichlerová (2012) [7], and laccase activity using SYZ was only obtained with purified enzyme; similarly in the present study, both white and blue laccase did not exhibit oxidation with SYZ. The optimal concentration of various substrate was determined, and it was observed that, for white laccase from *Myrothecium verrucaria* ITCC-8447, it was ABTS (0.5 mM), 2,6 DMP (2 mM), and GCL (30 mM), and for blue laccase from *Pleurotus ostreatus*, it was ABTS (1.5 mM), 2,6 DMP (2 mM), and GCL (30 mM). Similarly, the protein concentration for white and blue laccase was 1.82 mg/mL and 0.29 mg/mL, respectively (Table 10.1).

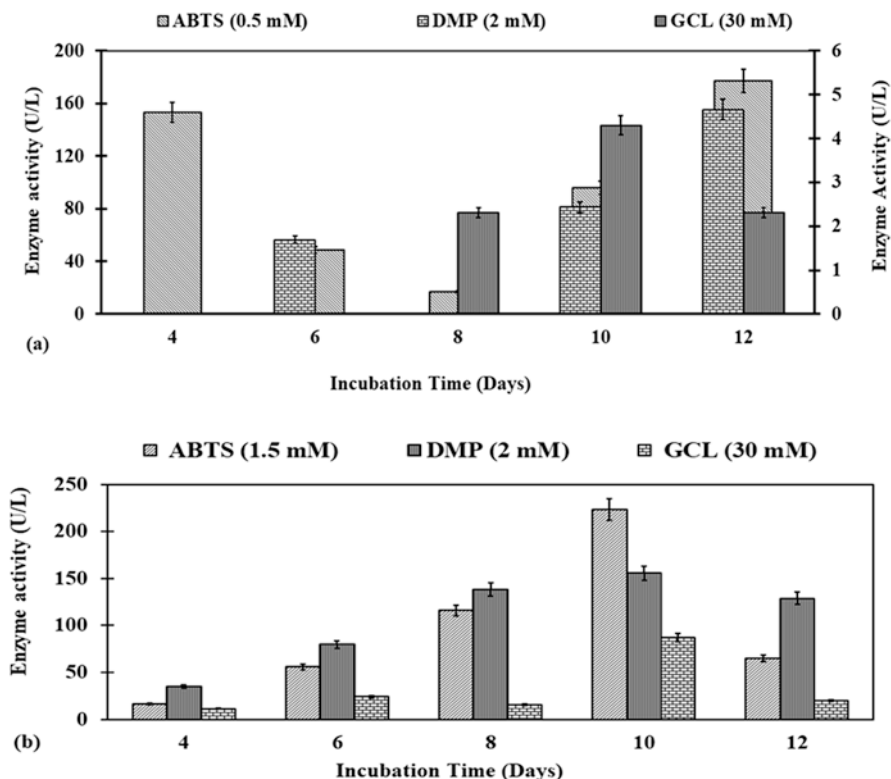


Fig. 10.1 (a) *Myrothecium verrucaria* ITCC-8447: detection of white laccase activity by ABTS, 2,6 DMP, and GCL for 12 days. (b) *Pleurotus ostreatus*: detection of blue laccase activity by ABTS, 2,6 DMP, and GCL for 12 days

Table 10.1 White and blue laccase activity from *Myrothecium verrucaria* ITCC-8447 and *Pleurotus ostreatus* with different substrates (ABTS, DMP, and GCL), protein concentration, and enzyme activity on the tenth day

Substrate concentration (mM)	Protein concentration (mg/mL)	Enzyme activity (UL ⁻¹)
<i>Myrothecium verrucaria</i> ITCC-8447		
ABTS (0.5)	1.82	95.8
DMP (2.0)	1.82	2.4
GCL (30.0)	1.82	4.3
<i>Pleurotus ostreatus</i>		
ABTS (1.5)	0.29	223.1
DMP (2.0)	0.29	155.7
GCL (30.0)	0.29	87.4

10.3.3 Synthesis of Bio-material Using White and Blue Laccase

The bio-material synthesized from WB and SB using white and blue laccase from *Myrothecium verrucaria* ITCC-8447 and *Pleurotus ostreatus* had a volume of 15.3 mm³ and 10.5 mm³ (Fig. 10.2a, b) and 25.7 mm³ and 54.9 mm³ (Fig. 10.2c, d),

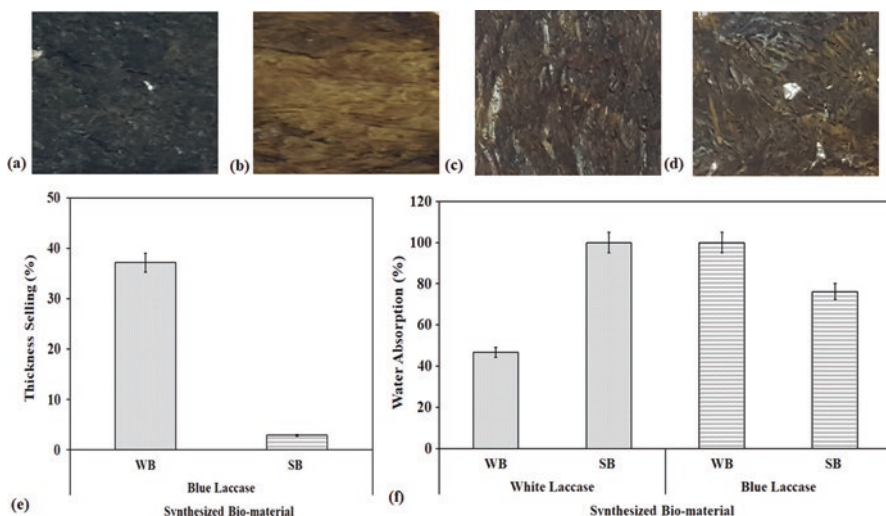


Fig. 10.2 Synthesis of bio-material via fungal-assisted treatment of wheat bran (WB) and sugarcane bagasse (SB) using white laccase (a–b) and blue laccase (c–d) followed by microwave pre-treatment and addition of starch and glycerol. (e) Thickness swelling (%) of blue laccase-synthesized bio-material (f) water absorption (%) of the white and blue laccase-synthesized bio-material

respectively. The percentage of thickness swelling observed in case of both WB and SB was negligible when synthesized using white laccase; however, in blue laccase-synthesized bio-material, it was 37.2 and 3.0 (Fig. 10.2e). These results are in accordance with Jeefferie et al. [15] which states that the thickness swelling is directly proportional to the size of fiber, i.e., smaller the size of the fiber less is the thickness swelling and vice versa [15]. The percentage of water absorption for white laccase-synthesized bio-material was 46.7 and 100 for WB and SB, respectively, whereas for blue laccase-synthesized bio-material, the percentage of water absorption was 100 and 76 (Fig. 10.2f). The water absorption of the bio-material significantly affects the structural integrity of bio-materials and results due to the saturation of the fibers in the presence of water; it also gives an insight into the water diffusivity of the bio-material [15].

10.4 Conclusion

The present study states that the most effective substrate was ABTS for white and blue laccase-producing strain *Myrothecium verrucaria* ITCC-8447 and *Pleurotus ostreatus*. The fungal-assisted treatment using white and blue laccase followed by pre-treatment was employed for the synthesis of bio-material. The WB-synthesized bio-material via white laccase exhibited minimum water absorption percentage in comparison to the other synthesized bio-material. Thus, the delignification capability of the agro-residues and its role in bio-material synthesis using pre-treatment

and binding agents can be effectively utilized for the reutilization of waste agro-residues in synthesis of bio-material, thereby fitting in the recent concept of “waste recycling.”

References

1. Hattori M, Konishi H, Tamura Y et al (2005) Laccase-type phenoloxidase in salivary glands and watery saliva of the green rice leafhopper, *Nephotettix cincticeps*. *J Insect Physiol* 51(12):1359–1365
2. Surwase SV, Patil SA, Srinivas S et al (2016) Interaction of small molecules with fungal laccase: a surface plasmon resonance based study. *Enzym Microb Technol* 82:110–114
3. Martinez AT, Ruiz-Duenas FJ, Martinez MJ, del Rio JC, Gutierrez A (2009) Enzymatic delignification of plant cell wall: from nature to mill. *Curr Opin Biotechnol* 20:348–357
4. Karp SG, Faraco V, Amore A, Letti LAJ, Thomaz Soccol V, Soccol CR (2015) Statistical optimization of laccase production and delignification of sugarcane bagasse by *Pleurotus ostreatus* in solid-state fermentation. *Biomed Res Int* 2015:1–8
5. Afreen S, Anwer R, Singh RK et al (2016) Extracellular laccase production and its optimization from *Arthrospira maxima* catalyzed decolorization of synthetic dyes. *Saudi J Biol Sci* 25:1446–1453
6. Olga VKS, Elena VS, Valeria PG, Olga VM, Natalia VL, Aida ND, Alexander IJ, Alexander M (1998) Purification and characterization of the constitutive form of laccase from basidiomycete *Coriolus hirsutus* and effect of inducers on laccase synthesis. *Biotechnol Appl Biochem* 28:47–54
7. Eichlerová I, Šnajdr J, Baldrian P (2012) Laccase activity in soils: considerations for the measurement of enzyme activity. *Chemosphere* 88(10):1154–1160
8. Bourbonnais R, Paice M, Reid I et al (1995) Lignin oxidation by laccase isozymes from *Trametes versicolor* and role of the mediator 2, 2'-azinobis (3-ethylbenzthiazoline-6-sulfonate) in Kraft lignin depolymerization. *Appl Environ Microbiol* 61(5):1876–1880
9. Wu J, Kim KS, Lee JH et al (2010) Cloning, expression in *Escherichia coli*, and enzymatic properties of laccase from *Aeromonas hydrophila* WL-11. *J Environ Sci* 22(4):635–640
10. Jolival C, Madzak C, Brault A et al (2005) Expression of laccase IIIb from the white-rot fungus *Trametes versicolor* in the yeast *Yarrowia lipolytica* for environmental applications. *Appl Microbiol Biotechnol* 66(4):450–456
11. Rajagopal D, Show PL, Tan YS et al (2016) Recovery of laccase from processed *Hericium erinaceus* (Bull.: Fr) Pers. fruiting bodies in aqueous two-phase system. *J Biosci Bioeng* 122(3):301–306
12. Holme DJ, Peck H (1996) *Resolución de Problemas de Bioquímica Analítica*, first ed. Acribia, Zaragoza 160:114–126
13. Lowry OH, Rosebrough NJ, Farr AL et al (1951) Protein measurement with the Folin phenol reagent. *J Biol Chem* 193(1):265–275
14. Verma P, Watanabe T, Honda Y, Watanabe T (2011) Microwave-assisted pretreatment of woody biomass with ammonium molybdate activated by H₂O₂. *Bioresour Technol* 102(4):3941–3945
15. Jeefferie AR, Fariha ON, Warikh AR, Yuhazri MY, Sihombing H, Junid R (2011) Preliminary study of the physical and the mechanical properties of tapioca starch/sugarcane fiber cellulose composite. *J Eng Appl Sci* 6(4):7–15



Extraction of Fungal Xylanase Using ATPS-PEG/Sulphate and Its Application in Hydrolysis of Agricultural Residues

11

Nisha Bhardwaj and Pradeep Verma

Abstract

Xylanase is a well-known enzyme for the conversion of agricultural biomass into xylose using enzymatic hydrolysis process. Agricultural residues are the rich source of lignocellulosic biomass. Recently there has been increasing interest in the use of agricultural residues for the production of industrially important enzymes along with other value-added by-products. Large-scale purification of the desired enzyme from fermentation broth and purification of enzymes via economically feasible methods are the main obstacle in biotechnological industries. In the present study, aqueous two-phase system (ATPS) was utilized for the purification of extracellular crude xylanase obtained from the submerged culture of *Aspergillus oryzae* LC1 (ITCC-8571/NAIMCC-F-03390). Various sulphate salts were tested for xylanase purification, among them $MgSO_4$ showed best results with PEG and was selected for further studies. Response surface methodology based on Box-Behnken design was used for optimizing the ATPS parameters, such as the molecular weight of PEG, $MgSO_4$ and PEG concentration. The purification factor of xylanase was found maximum in the presence of high-molecular-weight PEG (8000), PEG intermediate concentration (11.3% w/w) and high $MgSO_4$ salt concentration (22.5% w/w). A 13-fold increase in purification factor was obtained under optimized conditions, with partition coefficient 8.8% and enzyme yield 86.8% at the top phase. The partially purified xylanase obtained using ATPS was further used for the enzymatic hydrolysis of different agricultural residues, followed by the analysis of the hydrolysis products by TLC.

N. Bhardwaj · P. Verma (✉)

Department of Microbiology, Central University of Rajasthan, Bandarsindari, Kishangarh, Ajmer, Rajasthan, India
e-mail: pradeepverma@curaj.ac.in

© Springer Nature Singapore Pte Ltd. 2020

P. C. Sadhukhan, S. Premi (eds.), *Biotechnological Applications in Human Health*, https://doi.org/10.1007/978-981-15-3453-9_11

95

KeywordsXylanase · ATPS · RSM · PEG · Enzymatic hydrolysis · Agroresidues

11.1 Introduction

Xylanase (EC 3.2.1.8) or endo-1,4- β -D-xylanase is an enzyme which catalyses the hydrolysis of glycosidic linkage (β -1.4) of xylan by forming xylose, xylobiose and other sugars as end products. Microbial xylanases have been used widely in many industries, such as pulp bleaching [1] and lignocellulose to biofuel bioconversion [2]. Therefore, it is essential to have rapid and low-cost purification techniques to exploit xylanase for various industrial applications.

Aqueous two-phase system (ATPS) is formed by two immiscible phases of polymer-polymer or polymer-salt when two mutually incompatible hydrophilic solutes are dissolved above an essential concentration. This system selectively distributes desirable and contaminant protein in separate phases according to the properties of partitioned biomolecules. ATPS has several advantages over other traditional purification methods, as it is a single-step process, uses economical equipment and reagents, high concentration capability, reusable in a cyclic process, high yield and velocity, low energy consumption and also is feasible for large-scale purification [3]. As well as due to its high water content (80–90%) and low interfacial tension, it can protect proteins from denaturation [4, 5].

The agricultural sector worldwide generates a huge quantity of lignocellulosic biomass every year, the most part which is considered as residues. These agricultural residues are generated at the time of harvest and also during the agricultural product processing such as oil extraction and milling. These processes create by-products which are normally left unutilized and become wastes [6]. The discarding system of these wastes, e.g. leaving on the ground to biodegrade or burning on the field itself, can create various environmental-related problems, such as bioleaching and greenhouse gas emission [7, 8]. Thus, the production and recovery of microbial enzymes using inexpensive agricultural end-products may improve the economic viability of bioprocess technology.

Thus, in the present study, RSM based on Box-Behnken design has been performed to study the effect of PEG molecular weight, PEG concentration and salt concentration in the purification of xylanase. ATPS using polyethylene glycol (PEG)/MgSO₄ was successfully employed for purification of fungal xylanase produced by *Aspergillus oryzae* LC1 from culture medium containing rice straw as the main carbon source in submerged fermentation. Partially purified xylanase was used for the hydrolysis of agricultural residues to produce industrially important by-products.

11.2 Materials and Methods

11.2.1 Fungal Strain: Isolation and Maintenance

The fungal strain *Aspergillus oryzae* LC1 (ITCC-8571/NAIMCC-F-03390) which was able to produce extracellular xylanase was isolated from leaf sample of plant *Lantana camera* obtained from Cachar district, Assam. The obtained pure culture was grown and maintained on potato dextrose agar.

11.2.2 Preparation of Crude Enzyme Extract

Crude enzyme extract was prepared in an Erlenmeyer flask (500 mL) containing 200 mL of modified MSBS (Mendel's and Sternberg Media) consisting (g/L) 3.5 (NH₄)₂SO₄; 2.0 KH₂PO₄; 0.3 Urea; 1.0 CaCl₂; 0.3 MgSO₄·7H₂O; 1 peptone; trace elements (mg/L) 5.0 FeSO₄; 1.6 MnSO₄·H₂O; 1.4 ZnSO₄·7H₂O; 2.0 CoCl₂; 0.1% Tween 80; 1% rice straw used as carbon source; and pH 5 [9]. After autoclaving, the flasks were inoculated with 4.35×10^7 spore/mL and incubated at 28 °C on orbital shaker at 100 rpm. On the 4th day, mycelia were separated from culture broth by filtration through Whatman No. 1 filter paper. The culture filtrate was used for further studies.

11.2.3 Xylanase Assay and Determination of Protein Concentration

Quantitative assay of xylanase activity was performed in cell-free crude enzyme extract according to the method of Ghose and Bisaria [10]. Determination of amount of reducing sugar was done by measuring absorbance at 540 nm [11]. Protein estimation was done by Lowry method (1951) [12] with BSA as standard.

11.2.4 Preparation of Aqueous Two-Phase System

Various concentrations of PEG and salts were used in equal volume and mixed with 2 mL of crude enzyme extract; final weight of the system was 10 g. Sample was mixed by vortex for 2 min at room temperature. The system was allowed to settle for 1 h. Two clear phases obtained after settling the system were separated carefully. Enzyme activity and protein concentration of both the phases were calculated.

11.2.5 Partition Parameters of Aqueous Two-Phase System

11.2.5.1 Partition Coefficient (K)

Partition coefficient was determined by using the formula $K = C_t/C_b$, where C_t is the total enzyme activity at the top phase and C_b is the total enzyme activity at the bottom phase [4].

11.2.5.2 Phase Volume Ratio (R)

The phase volume ratio is defined as $R = V_t/V_b$, where V_t is the volume of top phase and V_b is the volume of bottom phase [4].

11.2.5.3 Yield (Y %) of Enzyme at Top Phase

Yield (Y %) of xylanase at top phase was calculated as:

$$\begin{aligned} Y_{\text{Top}}(\%) &= \frac{\text{Enzyme in top phase}}{\text{Total amount of enzyme}} * 100 \\ &= \frac{C_t V_t}{C_t V_t + C_b V_b} * 100 \\ &= \frac{100KR}{1 + KR} \end{aligned}$$

11.2.5.4 Purification Factor (PF) of Xylanase in the Top Phase

Purification factor (PF) of xylanase in the top phase was calculated as:

$$PF_{\text{Top}} = \frac{\text{Specific activity of xylanase at top phase}}{\text{Specific activity of crude xylanase}}$$

where specific activity signifies the ratio between the total enzyme activity and the total protein concentration in the sample [4].

11.2.6 Optimization of ATPS by Using RSM: Box-Behnken Design

Stock solution of different molecular weight of PEG was prepared as 20% and 30% (w/v), whereas 40%, 50% and 60% (w/v) salt stock solution was prepared. Final concentration of PEG in ATPS was calculated as 7.5% and 11.3% (w/w) and salt concentration was 15%, 18.7% and 22.5% (w/w). A statistical tool known as response surface methodology (RSM) based on Box-Behnken design was used for optimizing the three important parameters, (A) PEG molecular weight, (B) PEG concentration and (C) salt concentration (w/w %), to enhance the purification factor of xylanase. The experimental design consisted of 12 experiments with three important variables in three different levels (+1, 0, -1) consisting five replicates at the centre point. The second-order polynomial equation which was selected to study the effect of each variable is as follows:

$$Y = \beta_0 + \beta_1 A + \beta_2 B + \beta_3 C + -\beta_1 \beta_2 AB + \beta_1 \beta_3 AC + \beta_2 \beta_3 BC$$

where Y = response variable; β_0 = intercept; $\beta_1, \beta_2, \beta_3$ = linear coefficients; $\beta_{1,2}, \beta_{1,3}, \beta_{2,3}$ = interaction coefficients; and A, B, C, AB, AC, BC = level of independent variables. Statistical significance of model was determined by Fisher's test value. The proportion of variance explained by the model was given by the multiple coefficient of determination and R squared (R^2) value. Design Expert (Version. 9.0) by STATEASE Inc., Minneapolis, USA, was used in this study.

11.2.7 Enzymatic Hydrolysis of Agroresidues

Enzymatic hydrolysis of rice straw (RS), rice husk (RH), wheat bran (WB), wheat straw (WS), sugarcane bagasse (SB), nut shell (NS), pearl millet husk (PMH) and barley husk (BH) was done by incubating 1% of substrate with partially purified xylanase at 50 °C for 6 h. The end product analysis of hydrolysis of agricultural residues using partially purified xylanase was done by determining the R_F (retention factor) and R_S (resolution) values of the TLC.

11.3 Results and Discussions

11.3.1 Crude Xylanase Extract

The crude extract obtained from *Aspergillus oryzae* showed maximum xylanase activity of 1245 ± 2.4 IU/mL with specific activity 150 ± 4 IU/mL, at 28 °C and pH 5 on the 4th day. The cell-free crude extract was used for purification study.

11.3.2 Selection of Phase-Forming Salt

In order to achieve the high enzyme yield and purity, various alkali and transition metal sulphate salts, such as Na_2SO_4 , K_2SO_4 , CaSO_4 , MgSO_4 , $(\text{NH}_4)_2\text{SO}_4$, ZnSO_4 , MnSO_4 , FeSO and CuSO_4 , were tested. Among them, MgSO_4 showed best results and is selected for further studies. In ATPS system, the partition coefficient greater than one was preferred, in which top phase having maximum enzyme activity as compared to the bottom phase with negligible enzyme activity. Garai and Kumar [4] have reported partitioning of xylanase obtained from *Aspergillus candidus* through ATPS by using PEG 4000 with phase volume ratio (R) of 0.83 and partition coefficient (K) of 5.16 while using phosphate salt and 0.69 (R) and 2.82 (K) while using sulphate salt. In the present study, phosphate salt showed negligible partitioning with PEG 4000, 6000 and 8000 (data not shown); thus phosphate salt was not selected for further study. On the other hand, with sulphate salt and PEG 4000, no partition was obtained, whereas very low phase separation was observed using PEG 6000. However, in the case of PEG 8000 and MgSO_4 maximum of 8.8 (K) with 1.7 (R) was obtained and used for further study.

11.3.3 Optimization of Purification Factor by Using Box-Behnken Design

PEG molecular weight, PEG concentration and salt concentration are the important parameters for the formation of suitable ATPS. The matrix of RSM based on Box-Behnken design was utilized the optimization of these parameters. All the coded units considering actual and predicted responses were shown in terms of xylanase activity. The selected fraction with highest xylanase activity in the top phase was further shown in terms of purification fold and yield in Table 11.2. The Model F -value of 19.38 implies the model is significant. There is only a 0.26% chance that an F -value this large could occur due to noise. Values of “Prob > F ” less than 0.0500 indicate model terms are significant. In this case B and C are significant model terms. Values greater than 0.1000 indicate the model terms are not significant.

The xylanase activity (Y) with highest purification factor was expressed in terms of the following second-order polynomial equation obtained after the ANOVA (analysis of variance), which represents (A) PEG molecular weight, (B) PEG concentration and (C) salt concentration (Table 11.1).

$$\begin{aligned} \text{Xylanase activity (IU/mL) (Y)} = & (239.34) + (29.69 \times A) \\ & + (68.77 \times B) + (80.59 \times C) + (-8.27 \times AB) \\ & + (6.82 \times AC) + (18.35 \times BC) \end{aligned}$$

where, Y = xylanase activity, A = PEG MW, B = PEG concentration, and C = salt concentration.

Many criteria could be used to evaluate the fit of model. Coefficient determination (R^2), adjusted R^2 , predicted R^2 , adequate precision and ‘Lack of Fit’ were used in the present study. The R^2 value was calculated as 0.9588 for xylanase purification,

Table 11.1 Analysis of variance (ANOVA) fits the model regression in terms of xylanase activity resulting in maximum purification fold

ANOVA for response surface 2FI model						
Analysis of variance table [partial sum of squares – Type III]						
Source	Sum of squares	Df	Mean square	F value	p-value prob > F	
Model	2.577E+005	6	42951.25	19.38	0.0026	Significant
A-PEG MW	7694.57	1	7694.57	3.47	0.1215	
B-PEG Concentration	41274.50	1	41274.50	18.62	0.0076	
C-SALT concentration	2.078E+005	1	2.078E+005	93.77	0.0002	
AB	821.05	1	821.05	0.37	0.5694	
AC	1488.94	1	1488.94	0.67	0.4497	
BC	10773.65	1	10773.65	4.86	0.0786	
Residual	11082.79	5	2216.56			
Core total	2.688E+005	11				

R^2 : 0.9588, Adj R^2 : 0.9093, Pre R^2 : 0.7720, C.V: 29.66, Adequate precision: 13.042

Table 11.2 Purification table of xylanase from *A. oryzae* using PEG 8000/MgSO₄ system

Technique	Purification step	Volume	Enzyme activity	Protein mg/mL	Total activity	Total protein	Specific activity	Yield (%)	PF
ATPS	Crude	2	1247.4	8.1	2494.9	16.2	154	100	1
PEG 8000/ MgSO ₄	22.5% SALT 11.3% PEG	5	432.9	0.2	2164.6	1.08	2004.3	86.8	13.01

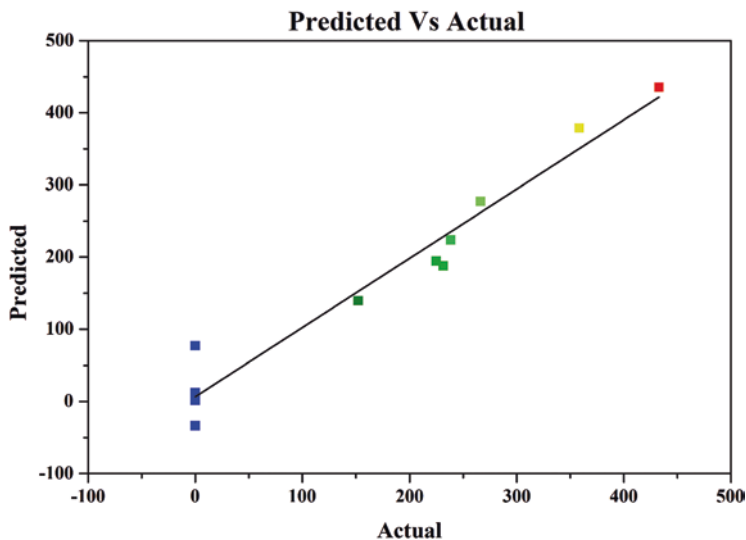


Fig. 11.1 Parity plot of actual and model predicted values for xylanase activity

which indicates that the model could explain 95.88% of the response variability. The 'Predicted R-Squared' of 0.7720 is in reasonable agreement with the 'Adjusted R-Squared' of 0.9093, i.e. the difference is less than 0.2. Preferably adjusted R^2 must be in close to R^2 value. Large difference between R^2 and adjusted R^2 indicates that the model is containing too many insignificant terms [13]. 'Adequate Precision' measures the signal to noise ratio and is defined as the ratio of response to deviation. A ratio greater than 4 is desirable. Ratio of 13.042 indicates an adequate signal. This model can be used to navigate the design space. Predicted and observed value of xylanase activity shown in Fig. 11.1 stated that the correlation between experimental and predicted value is satisfactory in which the centralized data points were adjacent to the diagonal line of the graph.

The significant interaction was found between A and B and A and C, as well as between B and C. 3D graphs represent response surface of two different parameters while keeping the third one at its constant zero level. Figure 11.2a states that the higher molecular weight of PEG in its maximum concentration favoured the higher fold of purification. Similarly, higher salt concentration has also increased the purification fold of xylanase.

11.3.4 Experimental Validation of Model Predicted Value

Using the desirability function criteria of design expert software, the optimum concentration of the selected parameters was predicted and conformation set of experiments was performed in triplicates. On the basis of study, maximum purification fold of xylanase was achieved while using PEG MW 8000, PEG concentration

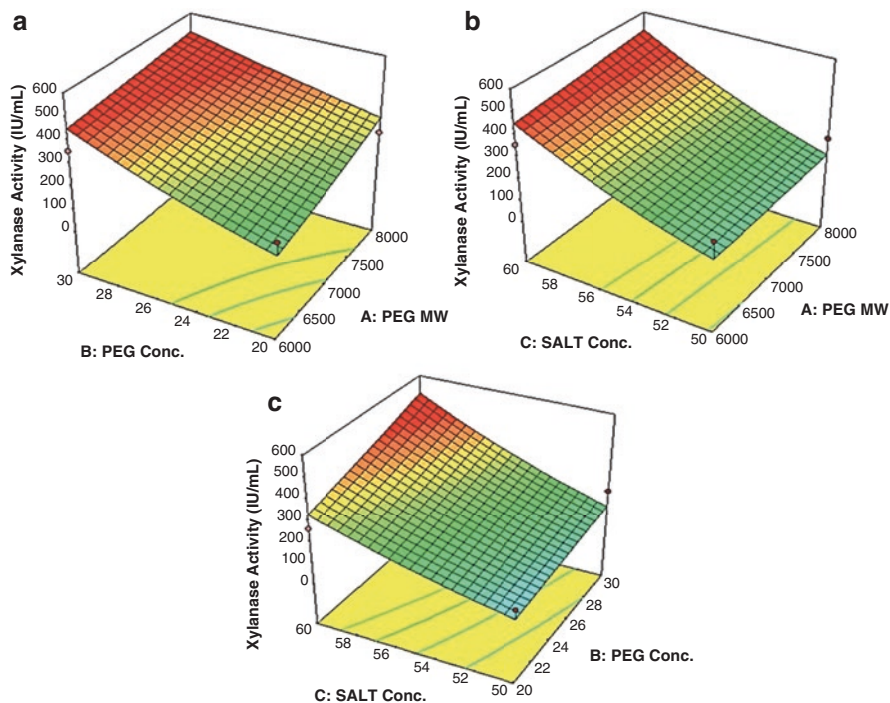


Fig. 11.2 Response surface plot displaying relative effect of two variables. (a) PEG concentration and PEG molecular weight, (b) PEG molecular weight and salt concentration and (c) PEG concentration and salt concentration

11.3% (w/w) and salt concentration 22.5% (w/w). The activity of the purified xylanase obtained from the optimized conditions was very close to the predicted value (Fig. 11.1). Hence, the high-molecular-weight polymer and high concentration of salt and polymer were found capable of increasing purification factor (Table 11.2).

Salting out effect and volume exclusion effect of polymer are the two main factors governing partitioning and purification factor [14]. With the increase in the concentration of salt (salting out effect), molecules move towards the top phase. In our study, purification fold was increased with increasing the sulphate salt concentration from 40% to 60%. The salt changes the surface properties of the enzyme and makes it hydrophobic in nature which tends to do more partition [15]. In previous studies of xylanase purification using ATPS, researchers have reported fungal xylanase produced from *Polyporus squamosus* showed 4.8-fold purification with 97.4% yield with PEG/sulphate system [16]. Xylanase produced by *Paecilomyces thermophila* was purified by using PEG/sulphate system and showed 5.5-fold purification with 98.7% yield [7]. In our present study, under optimized condition, 13-fold purification with 86.8% yield was obtained using PEG 8000/MgSO₄.

Table 11.3 R_F (retention factor) and R_S (resolution) obtained from TLC of the hydrolysates of agroresidues treated by partially purified xylanase from ATPS

Agroresidues	R_F					R_S
	S1	S2	S3	S4	S5	
RS			0.5		3.6	1.93
RH		5.9	4.9			1.02
WS	6.5	0.6	5.2			1.97
WB	0.6	0.5	0.4			1.42
SB	0.6	0.5	0.4			1.36
PMH	0.7	0.6	0.5			1.14
NS		0.6	0.5	0.4		1.08
BH		0.6	0.5	0.4		1.15

Note: *SB* sugarcane bagasse, *RS* rice straw, *WB* wheat bran, *RH* rice husk, *WS* wheat straw, *NS* peanut shell, *PMH* pearl millet husk, *BH* barley husk

11.3.5 Determination of Hydrolysis Products of Agroresidues

The determination of end products of hydrolysis of all the agroresidues by partially purified xylanase using ATPS was done by using TLC. Different spots were detected on the TLC sheet, of which S1 was considered to be xylose when compared to commercial D-xylose as standard and spots S2–S5 may indicate the presence of different sugar molecules. Further study is under progress to confirm these molecules by HPLC. The observed R_F values indicate the presence of different sugar molecules in the hydrolysates of all the tested agroresidues. R_S values of all the agroresidues are greater than 1.0, which suggests that the sugar molecules are considered to be resolved (Table 11.3).

11.4 Conclusion

RSM based on Box-Behnken design was successfully employed for ATPS- PEG/ $MgSO_4$ system which gave optimal concentration of 11.3% (w/w) PEG 8000 and 22.5% $MgSO_4$ (w/w) for xylanase purification. ATPS-PEG/ $MgSO_4$ is an efficient extraction process to achieve maximum of 13-fold purification and 86.8% yield of xylanase from cell-free crude extract of *Aspergillus oryzae* LC1 (ITCC-8571/ NAIMCC-F-03390). The conventional purification processes are time-consuming, multistep processes such as precipitation, dialysis and washing, and use of costly chemicals in chromatographic techniques causes product loss with each step. ATPS is a single-step process, and use of low-cost chemical components increases its economic feasibility during the scale-up process. The partially purified xylanase obtained using ATPS was used for the enzymatic hydrolysis of agricultural residues. Based on the observed R_F and R_S values of the treated agroresidues by partially purified xylanase, xyloses along with different sugar molecules were detected as the end product. These end products can be further utilized for various industrial applications such as xylooligosaccharide and bioethanol (biofuel) generation.

Acknowledgement The authors are thankful to DBT for providing the financial support (Grant No. BT/304/NE/TBP/2012).

References

1. Taneja K, Gupta S, Kuhad RC (2002) Properties and application of a partially purified alkaline xylanase from an alkalophilic fungus *Aspergillus nidulans* KK-99. *Bioresour Technol* 85(1):39–42
2. Tabka M, Herpoel-Gimbert I, Monod F, Asther M, Sigoillot JC (2006) Enzymatic saccharification of wheat straw for bioethanol production by a combined cellulase xylanase and feruloyl esterase treatment. *Enzym Microb Technol* 39(4):897–902
3. Patil G, Raghavarao K (2007) Aqueous two phase extraction for purification of C-phycoyanin. *Biochem Eng J* 34(2):156–164
4. Garai D, Kumar V (2013) Aqueous two phase extraction of alkaline fungal xylanase in PEG/phosphate system: optimization by Box-Behnken design approach. *Biocatal Agric Biotechnol* 2(2):125–131
5. Naganagouda K, Mulimani V (2008) Aqueous two-phase extraction (ATPE): an attractive and economically viable technology for downstream processing of *Aspergillus oryzae* α -galactosidase. *Process Biochem* 43(11):1293–1299
6. Cardoen D, Joshi P, Diels L, Sarma PM, Pant D (2015) Agriculture biomass in India: part 1. Estimation and characterization. *Resour Conserv Recycl* 102:39–48
7. ElMekawy A, Diels L, De Wever H, Pant D (2013) Valorization of cereal based biorefinery byproducts: reality and expectations. *Environ Sci Technol* 47(16):9014–9027
8. ElMekawy A, Diels L, Bertin L, De Wever H, Pant D (2014) Potential biovalorization techniques for olive mill biorefinery wastewater. *Biofuels Bioprod Biorefin* 8(2):283–293
9. Bhardwaj N, Chanda K, Kumar B, Prasad HK, Sharma GD, Verma P (2017) Statistical optimization of nutritional and physical parameters for Xylanase production from newly isolated *Aspergillus oryzae* LC1 and its application in the hydrolysis of lignocellulosic agro-residues. *Bioresources* 12(4):8519–8538
10. Ghose T, Bisaria VS (1987) Measurement of hemicellulase activities: part I xylanases. *Pure Appl Chem* 59(12):1739–1751
11. Miller GL (1959) Use of dinitrosalicylic acid reagent for determination of reducing sugar. *Anal Chem* 31(3):426–428
12. Lowry CC, Kraeft NH, Hughes FA Jr (1951) Blastomycosis of the lung. *Am J Surg* 81(6):676–679
13. Haaland PD (1989) *Experimental design in biotechnology*, vol 105. CRC Press, Boca Raton
14. Babu BR, Rastogi N, Raghavarao K (2008) Liquid–liquid extraction of bromelain and polyphenol oxidase using aqueous two-phase system. *Chem Eng Process Process Intensif* 47(1):83–89
15. Vaidya BK, Suthar HK, Kasture S, Nene S (2006) Purification of potato polyphenol oxidase (PPO) by partitioning in aqueous two-phase system. *Biochem Eng J* 28(2):161–166
16. Antov MG, Pericin DM, Dasic MG (2006) Aqueous two-phase partitioning of xylanase produced by solid-state cultivation of *Polyporus squamosus*. *Process Biochem* 41(1):232–235



Thyme (*Thymus vulgaris*) Essential Oil-Based Antimicrobial Nanoemulsion Formulation for Fruit Juice Preservation

12

Aakash Patel and Vijayalakshmi Ghosh

Abstract

More effective preservation strategies need to be found to fight increasing emergence of food-borne diseases. Preservation is a process of prevention of decay and spoilage of food. One of the potent sources of antimicrobial compounds is plant essential oils which can be used for food preservation. The antimicrobial effect of essential oils is reduced in food system due to its hydrophobic nature. Nanoemulsion is a fine dispersion of two immiscible liquids which are thermodynamically more stable and optically isotropic. Therefore, nanoemulsion can be used as potent antimicrobial delivery system for preservation. The purpose of this study was to develop different thyme oil in water nanoemulsion formulations by optimizing different parameters such as oil concentration, surfactant concentration and co-surfactant concentration. Nanoemulsion formulations were characterized by dynamic light scattering, stability test and turbidity. Nanoemulsion formulation with oil-surfactant (Thyme oil-Tween80) concentration ratio of 1:5 v/v was found to be stable (more than 3 months) and translucent having droplet diameter of 83 nm. The selected thyme oil nanoemulsion formulation was found to be exhibiting its antibacterial activity against *S. aureus*. The in situ taxation of the nanoemulsion in fruit juice demonstrated significant decline in inherent microbial population.

Keywords

Thyme oil · Nanoemulsion · Antimicrobial · Food preservation

A. Patel · V. Ghosh (✉)

P. C. Bhakta Institute of Biotechnology, Uka Tarsadia University,
Tarsadi, Surat, Gujarat, India

12.1 Introduction

Bioprocessing and food industries are facing challenges in maintaining good quality of food. Food spoilage by microbial contamination is one of the major problems of food industries. The research for new safe food preservation strategies is being performed worldwide [1]. Development of synthetic food preservatives requires great money and time for their formation and approval process [2]. One of the potent alternatives to synthetic food additives is bioactive compounds arising from plants which have antimicrobial and antioxidant properties [3]. One of the effective sources of antimicrobial compounds is plant essential oils which can be used for food preservation. Essential oils derived from plants have been reported to exhibit noteworthy antimicrobial power in contradiction of spoilage and pathogenic microorganisms [4]. Various bio-active compounds of essential oils are benzaldehyde, carvacrol, carvone, cineole, cinnamaldehyde, citral, cymene, estragole, eugenol, geraniol, limonene, methanol, pinene, terpinene, terpineol, thymol and vanillin [5–7]. To improve the dispersion of the essential oil in water and also to protect it from degradation, nanoemulsions have emerged as a great alternative [8]. Nanoemulsion can serve as a potent delivery system for essential oils [9]. Nanoemulsion is a fine dispersion of two immiscible liquids (oil and water) with each oil droplet circumvented by a thin interfacial layer consisting of surfactant molecules [10–12]. Different methods are there for the formulation of nanoemulsion. These methods are mainly divided into two categories: high-energy methods and low-energy methods [10, 12, 13]. High-energy methods mostly require sophisticated instruments and high energy for the formulation of nanoemulsion, e.g. high-pressure homogenizer, microfluidizer and ultrasonication [13–16]. Emulsions formulated with low-energy method are generally called as coarse emulsions which can be further treated with high-energy method to reduce the droplet size [17]. Spontaneous emulsion method, phase inversion composition, phase inversion temperature and emulsion inversion point are examples of low-energy methods. Ultrasound cavitation can be used for reduction of droplet size with the help of high-frequency sound waves (20 kHz). It can yield emulsion having smaller droplet size, greater stability and lesser polydispersity.

12.2 Materials and Methods

12.2.1 Chemical Reagents

Thyme essential oil (extracted from *Thymus vulgaris*), refined and food grade, was obtained from local market. Tween 80 (polyoxyethylene (20) sorbitan monooleate), a non-ionic surfactant, was obtained (SDFCL, Mumbai) and utilized. Distilled water was used for all experiments throughout the study.

12.2.2 Nanoemulsion Formulation

Nanoemulsion was formulated using thyme oil, non-ionic surfactant Tween 80 and water. Thyme oil (4%) used was refined and food grade. Non-ionic surfactant Tween 80 was used due to its high hydrophilic-lipophilic balance (HLB) value of 15 which is suitable for formation of oil in water emulsion. The effectiveness of Tween 80 in minimizing droplet diameter of nanoemulsion is due to their rapid adsorption on droplet surface. Initially coarse emulsion was prepared by mixing organic phase (oil and surfactant) and water. Organic phase was added drop-wise to water under continuous stirring using a magnetic stirrer. The coarse emulsion was then subjected to ultrasonic emulsification using probe sonicator (PCI Analytics KS-250F) with power of 250 W. Energy is supplied through probe horn. The probe generates high-frequency sound waves which forms emulsion droplet by process of cavitation. Different formulations were prepared by optimizing process parameter (surfactant concentration), keeping oil concentration constant (4%), which were mixed in various ratios (1:1, 1:2, 1:3, 1:4, 1:5) and labelled as T1, T2, T3, T4 and T5. The characterization of all the formulated emulsions was done and their stability was determined.

12.3 Characterization of Nanoemulsion

12.3.1 Droplet Size Measurement

The measurement of droplet size of the formulated emulsion was performed by particle size analyser (Zetasizer Nano ZS90) using technique of dynamic light scattering (DLS). The polydispersity index and droplet size of formulated emulsions were measured.

12.3.2 Physicochemical Characterization

The pH value of the formulated emulsions was measured by pH meter (Arvind Industries SV4, India) at room temperature. The absorbance of the undiluted emulsion samples was measured at 600 nm using spectrophotometer (SHIMADZU UV-1800) to determine the turbidity of the formulated emulsion.

12.3.3 Stability

To determine the stability, formulated emulsions were subjected to centrifugation at 10000 rpm for half an hour, and phase separation was checked (if any).

All the formulated emulsions were stored at room temperature for prolonged storage time to determine the intrinsic stability. Phase separation or creaming (if any) was then observed. All the experiments were performed in duplicates.

12.4 Antibacterial Activity

12.4.1 Inactivation Kinetics of Bacterial Population

For assessment of antibacterial activity, thyme oil nanoemulsion T5 was chosen due to its low droplet size and high stability than other formulations. Killing of *S. aureus* population upon treatment with thyme oil nanoemulsion was determined depending on two parameters, i.e. time and nanoemulsion concentration. Overnight culture of *S. aureus* was centrifuged at 6000 rpm for 10 min and washed twice in phosphate buffer saline (pH 7.4). Test culture with known inoculum size was then prepared (10^7 CFU/ml). The test culture was then treated with undiluted and diluted (10-fold, 100-fold, 1000-fold) T5 thyme oil nanoemulsion for different time intervals. For viable count enumeration, 100 μ l of the interacted sample was spread onto nutrient agar plates and incubated for 24 h at 37 °C. After incubation, colonies were counted. All experiments were performed in duplicates.

12.4.2 Preservation of Juice

The antimicrobial activity of Thyme oil nanoemulsion against microbial spoilage for preservation of fruit juice was examined, over a time period of 24 h. In laboratory, fresh sweet lime juice was prepared under sterile condition. Its microbial count was evaluated by spreading 10 μ l of juice onto nutrient agar plates and incubated overnight at 37 °C, and numbers of colonies were enumerated. Juice was then treated with 10% nanoemulsion and sodium benzoate. Bactericidal effect of nanoemulsion and sodium benzoate in fruit juice was examined by determining the effect of two distinct process variables, i.e. time and temperature.

12.5 Results and Discussion

12.5.1 Selection of Nanoemulsion Formulation

Thyme oil, Tween 80 and water were used to prepare different nanoemulsion formulations by mixing oil and surfactant in different ratios. Nanoemulsion formulation T5 with oil-surfactant ratio of 1:5 showed highest stability as compared to other formulations. Centrifugation of formulations resulted into phase separation of T1, T2 and T3. Intrinsic stability was not observed in formulation T4 upon storage, but nanoemulsion T5 was found to be stable. In addition, nanoemulsion T5 was translucent as compared to other formulations which were turbid indicating low droplet size of nanoemulsion T5.

12.5.2 Droplet Size

Nanoemulsion formulations were obtained as a result of ultrasonic emulsification of coarse emulsion for 20 min using sonicator. Tween 80 being a small molecule

surfactant gets rapidly adsorbed onto droplet surface, and hence they are more efficient in minimizing droplet diameter than other polymers. The mean droplet diameter of the formulation T5 was found to be 83 nm. The homogeneity of the nanoemulsion droplets was indicated by polydispersity index (PDI) of 0.24.

12.5.3 Physicochemical Characterization

Thyme oil nanoemulsion T5 was optically translucent while other formulations were turbid. Initially coarse emulsion prepared was turbid. However, after ultrasonic emulsification, the emulsion became optically translucent. The absorbance at 600 nm was 0.6 abs. The pH of nanoemulsion at room temperature was 6.8.

12.5.4 Stability

Stability was assessed by centrifuging nanoemulsion formulations for half an hour at 10000 rpm. Nanoemulsion formulation T5 was found to be stable as phase separation was not observed. In addition, formulation T5 was more stable than other formulations when stored at room temperature for prolonged period of time.

12.5.5 Antibacterial Activity

12.5.5.1 Inactivation Kinetics of Bacterial Population

Thyme oil nanoemulsion T5 was used due to its low droplet size and higher stability. Loss in viability of *S. aureus* was observed over a short period of time upon treatment with thyme oil nanoemulsion depending on time and concentration in experiment of inactivation of kinetics. The reduction of *S. aureus* upon treatment with different dilutions (10-fold, 100-fold, 1000-fold) of thyme oil nanoemulsion is shown in Fig. 12.1.

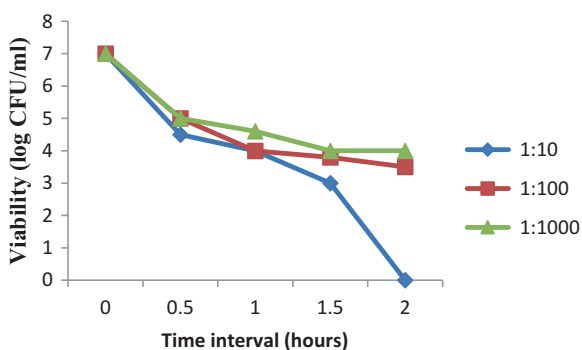


Fig. 12.1 Time- and concentration-dependent killing of bacterial population upon treatment with thyme oil nanoemulsion

Inactivation with tenfold diluted nanoemulsion demonstrated approximately 3 log reduction in cell viability within half an hour of exposure; complete loss of viability was observed in 2 h. Treatment with 100-fold diluted nanoemulsion showed 40% loss in viability in 60 min, 3 log reduction in population within 120 min. In case of 1000-fold diluted nanoemulsion, 2 log reduction in *S. aureus* population was observed within 60 min and 3 log reduction within 120 min. In this study, effective bactericidal activity was observed even after dilution (10-fold, 100-fold, 1000-fold) of nanoemulsion with sterile water. However, microemulsion loses their bactericidal activity when diluted with water (Fig. 12.2).

12.5.5.2 Preservation of Fruit Juice

Thyme oil nanoemulsion T5 demonstrated antibacterial activity on inherent bacterial population in sweet lime juice. A reduction in bacterial population was observed up to 4 h by both 10% nanoemulsion and sodium benzoate upon storage at 4 °C and room temperature. Approximately 40% loss of viability was observed at 2 h and 4 h upon treatment with 10% nanoemulsion in case of both 4 °C and room temperature. Further gradual increase in bacterial population was observed at 24 h for storage temperature of 4 °C and room temperature. Nanoemulsion exhibited enhanced antibacterial activity as compared to sodium benzoate at both 4 °C and room temperature (Fig. 12.3).

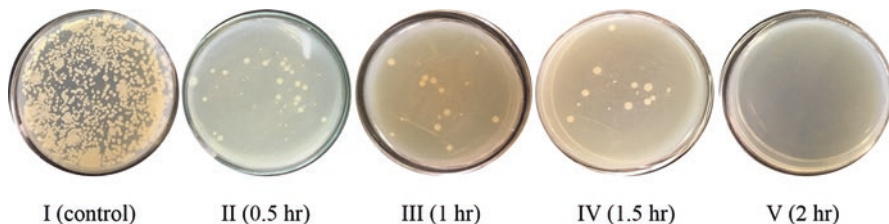


Fig. 12.2 Loss of viability in *S. aureus* population upon treatment with thyme oil nanoemulsion (10-fold diluted) at different time interval

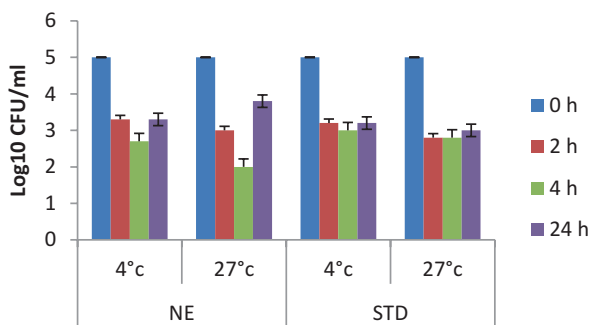


Fig. 12.3 Time- and temperature-dependent antibacterial activity of 10% nanoemulsion and sodium benzoate

12.6 Conclusion

Different thyme oil nanoemulsion formulations were prepared by optimizing process parameters such as oil and surfactant concentration. Thyme oil nanoemulsion T5 was found to be most stable and had lower droplet size as compared to other formulations. Therefore, formulation T5 was selected for antibacterial assay. Nanoemulsion T5 exhibited bactericidal activity against *S. aureus* even after dilution. Further, thyme oil nanoemulsion T5 was also effective in reducing bacterial population in sweet lime juice and hence can be utilized for prevention of microbial spoilage for preservation of juice.

References

1. Magnuson B, Munro I, Abbot P, Baldwin N, Lopez-Garcia R, Ly K, McGirr L, Roberts A, Socolovsky S (2013) Review of the regulation and safety assessment of food substances in various countries and jurisdictions. *Food Addit Contam Part A* 30(7):1147–1220
2. Tajkarimi MM, Ibrahim SA, Cliver DO (2010) Antimicrobial herb and spice compounds in food. *Food Control* 21:1199–1218
3. Ortega-Ramirez LA, Rodriguez-Garcia I, Leyva JM, Cruz-Valenzuela MR, Silva-Espinoza BA, Gonzalez-Aguilar GA, Siddiqui Wasim MD, Ayala-Zavala JF (2014) Potential of medicinal plants as antimicrobial and antioxidant agents in food industry: a hypothesis. *J Food Sci* 79(2):R129–R137
4. Jayasena DD, Jo C (2013) Essential oils as potential antimicrobial agents in meat and meat products: a review. *Trends Food Sci Technol* 34(2):96–108
5. Burt S (2004) Essential oils: their antibacterial properties and potential applications in foods – a review. *Int J Food Microbiol* 94(3):223–253
6. Singh G, Maurya S, deLampasona MP, Catalan CAN (2007) A comparison of chemical, anti-oxidant and antimicrobial studies of cinnamon leaf and bark volatile oils, oleoresins and their constituents. *Food Chem Toxicol* 45(9):1650–1661
7. Wang R, Yang B (2009) Extraction of essential oils from five cinnamon leaves and identification of their volatile compound compositions. *Innovative Food Sci Emerg Technol* 10(2):289–292
8. Acevedo-Fani A, Salvia-Trujillo L, Rojas-Graü MA, Martín-Belloso O (2015) Edible films from essential-oil-loaded nanoemulsions: physicochemical characterization and antimicrobial properties. *Food Hydrocoll* 47:168–177
9. Donsì F, Cuomo A, Marchese E, Ferrari G (2014) Infusion of essential oils for food stabilization: unraveling the role of nanoemulsion-based delivery systems on mass transfer and antimicrobial activity. *Innovative Food Sci Emerg Technol* 22:212–220
10. Tadros T, Izquierdo P, Esquena J, Solans C (2004) Formation and stability of nano-emulsions. *Adv Colloid Interf Sci* 108–109:303–318
11. McClements DJ, Decker EA, Weiss J (2007) Emulsion-based delivery systems for lipophilic bioactive components. *J Food Sci* 72(8):R109–R124
12. Acosta E (2009) Bioavailability of nanoparticles in nutrient and nutraceutical delivery. *Curr Opin Colloid Interface Sci* 14(1):3–15
13. Leong TSH, Wooster TJ, Kentish SE, Ashokkumar M (2009) Minimising oil droplet size using ultrasonic emulsification. *Ultrason Sonochem* 16(6):721–727
14. Gutiérrez JM, González C, Maestro A, Solè I, Pey CM, Nolla J (2008) Nano-emulsions: new applications and optimization of their preparation. *Curr Opin Colloid Interface Sci* 13(4):245–251
15. Velikov KP, Pelan E (2008) Colloidal delivery systems for micronutrients and nutraceuticals. *Soft Matter* 4(10):1964–1980

-
16. Wooster TJ, Golding M, Sanguansri P (2008) Impact of oil type on nanoemulsion formation and Ostwald ripening stability. *Langmuir* 24(22):1275–1276
 17. Ghosh V, Mukherjee A, Chandrasekaran N (2013) Ultrasonic emulsification of food-grade nanoemulsion formulation and evaluation of its bactericidal activity. *Ultrason Sonochem* 20(1):338–344